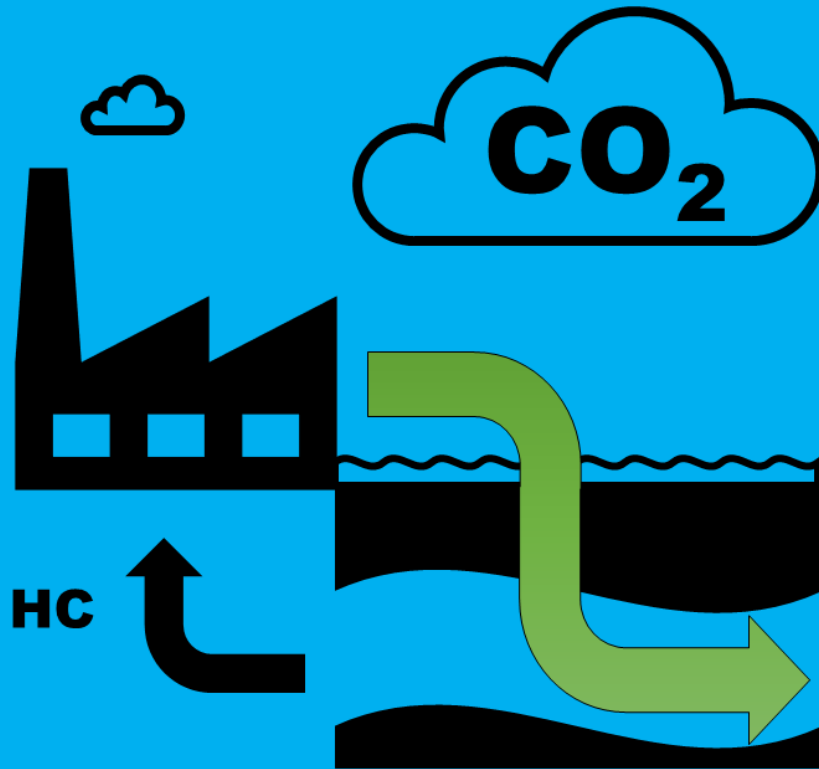


# MSc Thesis

Near wellbore effects induced by CO<sub>2</sub> injection and the influence on injectivity in depleted gas reservoirs

M.C.M. Creusen





# Near wellbore effects induced by CO<sub>2</sub> injection and the influence on injectivity in depleted gas reservoirs

by

M.C.M. Creusen

in partial fulfillment of the requirements for the degree of

**Master of Science**  
in Applied Earth Sciences

at the Delft University of Technology,  
to be defended publicly on Wednesday May 30, 2018 at 02:00 PM.

Student number:	4250737	
Supervisors:	Dr. H. Hajibeygi	TU Delft
	Ir. T. Huijskes	EBN B.V.
	Dr. Ir. R. Godderij	EBN B.V.
Thesis committee:	Prof. Dr. P. Zitha	TU Delft
	Dr. Ir. A-C. Dieudonné	TU Delft

An electronic version of this thesis is available at <http://repository.tudelft.nl/>.



# Abstract

Sequestration of carbon dioxide (CO<sub>2</sub>) in depleted gas reservoirs is an attractive choice, especially in The Netherlands, to reduce CO<sub>2</sub> emissions into the atmosphere. Injection of CO<sub>2</sub> in the subsurface geological formations can distort local thermal, chemical and geomechanical equilibria. As such, it results in highly coupled (thermo)physical effects in the near wellbore region, referred to as “near wellbore effects”. In this work, qualitative and quantitative descriptions of the near wellbore effects in depleted gas fields on macroscopic scale are provided. The primary focus is on the thermal effects (i.e., Joule-Thomson effect, water vaporization and CO<sub>2</sub> dissolution) and specific chemical effects (i.e., salt precipitation and hydrate formation). Occurrence and the corresponding magnitude of certain near wellbore effects influence the injectivity of CO<sub>2</sub> both positively and negatively. In several occasions these effects can lead to severe reduction of the injectivity. To accurately model these effects, thermal multi-component multi-phase simulations are conducted using both TOUGH2-ECO2MG and CMG-GEM commercial-grade simulators. Important is that these simulations include precipitation of salt and phase changes of CO<sub>2</sub> during repressurization of the reservoir. Extensive sensitivity study on numerous 1D, 2D and 3D reservoirs with various injection parameters and degrees of heterogeneity is carried out. A comprehensive 3D geological model of the nearly depleted P18-4 gas field (located in the Dutch North sea) is also investigated, in order to examine the near wellbore effects in a real-field application. Moreover, the potential control of the near wellbore thermal effects by interplay of controllable operational parameters (e.g. rate, temperature or composition) and the local reservoir pressure and temperature conditions is presented. Results reveal that the high injection rates targeted for real CO<sub>2</sub> injection (i.e., 1.1 Mt/yr) in combination with low initial reservoir pressures (> 40 bar) and a large reservoir volume provide favorable conditions for development of predominantly excessive cooling effects (15°C) near the wellbore. Injection of CO<sub>2</sub> in gaseous conditions at low temperatures can cause such strong cooling that hydrate can form, which can potentially jeopardize the injection process due to clogging of the reservoir. However, as for its specific geometry and well location, the thermal effects are significantly less pronounced in the P18-4 field model. Besides, heterogeneity of the formations plays a key role in the distribution of the appearing effects along the wellbore. Overall, for the considered cases, the injectivity is found to be enhanced rather than decreased by the studied near wellbore effects, with the proviso that the conditions in the near wellbore region remain outside the hydrate formation window.



# Preface

This MSc thesis marks the end of an exceptional educational period at the TU Delft and a fascinating internship at EBN.

First of all, I would like to thank Dr. Hadi Hajibeygi for being an outstanding supervisor. His critical feedback and detailed questions stimulated me to overthink my work and place it in a broader perspective. Since my BSc thesis, that was in fact also conducted under supervision of Hadi, a fruitful relation has been established over the recent years which provided to my experience an exceptional synergy. I strongly admire his ambition for reservoir simulation and academic research; it was a privilege to be supervised by him.

A special thanks to my daily supervisor Ir. Thijs Huijkes. Using his pragmatic approach, Thijs provided valuable input for this research and helped me to define the crux of CCS. His thorough understanding of the incorporated physics provided a lot of help to understand the thermodynamic aspects of compositional simulations.

I would also like to express my gratitude to Dr. Ir. Raymond Godderij. Based on his extensive experience on simulation and reservoir engineering in general, Raymond provided very helpful guidance. The weekly progress meetings with Thijs and Raymond were highly beneficial for the progress of this thesis.

Furthermore, I would like to thank various EBN employees, fellow interns and the DARSim group members for providing feedback on my project.

Finally, my gratitude also goes to Dr. Cor Hofstee and Ir. Daniël Loeve from TNO for providing part of the essential simulation software, TAQA for sharing the P18 reservoir model and the CMG support, especially Marco Misenta, for the assistance on the development of the depleted gas reservoirs systems in GEM. A significant part of this research could not have been performed without these contributions.

*M.C.M. Creusen  
Delft, May 2018*



# Contents

<b>List of Figures</b>	<b>x</b>
<b>1 Introduction</b>	<b>1</b>
1.1 Subsurface CO <sub>2</sub> storage . . . . .	2
1.1.1 Aquifer versus hydrocarbon reservoir storage . . . . .	3
1.1.2 Hydrocarbon reservoir types and storage options . . . . .	3
1.2 CO <sub>2</sub> storage potential in Dutch North Sea depleted gas fields . . . . .	4
1.3 Prior research on the modeling of geological CO <sub>2</sub> storage. . . . .	5
1.4 Research objectives . . . . .	6
<b>2 Fluid-rock characteristics and governing equations</b>	<b>7</b>
2.1 Characteristic properties of CO <sub>2</sub> , CH <sub>4</sub> , brine and their mixtures . . . . .	7
2.1.1 Phases and components . . . . .	7
2.1.2 CO <sub>2</sub> -CH <sub>4</sub> phase behavior . . . . .	7
2.1.3 Thermodynamic properties CO <sub>2</sub> and CH <sub>4</sub> . . . . .	8
2.1.4 Properties of brine . . . . .	9
2.1.5 Mutual solubility. . . . .	9
2.2 Thermal processes and parameters . . . . .	10
2.2.1 CO <sub>2</sub> and CH <sub>4</sub> dissolution . . . . .	10
2.2.2 Water vaporization. . . . .	10
2.2.3 Phase enthalpy changes by vaporization and dissolution . . . . .	10
2.2.4 Joule-Thomson effect . . . . .	11
2.2.5 Effective heat capacity and thermal conductivity . . . . .	11
2.3 Non-isothermal compositional multi-phase flow . . . . .	12
2.3.1 Mass conservation equation . . . . .	12
2.3.2 Energy conservation equation . . . . .	13
2.3.3 Thermodynamic equilibrium and component phase partitioning . . . . .	15
2.3.4 Injectivity . . . . .	17
2.3.5 Relative permeability curves . . . . .	18
2.3.6 Capillary pressure . . . . .	18
2.3.7 Additional constrains . . . . .	19
<b>3 Near wellbore effects</b>	<b>20</b>
3.1 Thermal effects . . . . .	21
3.1.1 Joule-Thomson effect . . . . .	21
3.2 Geochemical effects. . . . .	23
3.2.1 Hydrate formation . . . . .	23
3.2.2 Acid reactions . . . . .	24
3.2.3 Salt precipitation reactions. . . . .	25
3.3 Geomechanical . . . . .	26
3.3.1 Hydraulic and thermal fracturing . . . . .	26
<b>4 Numerical simulators and simulation overview</b>	<b>27</b>
4.1 Numerical simulators . . . . .	27
4.1.1 TOUGH2 ECO2MG . . . . .	27
4.1.2 CMG GEM . . . . .	28

4.2	Phase combinations and simulation variables . . . . .	29
4.3	Simulation overview and work flow . . . . .	29
4.4	Simulation models . . . . .	30
4.4.1	1D and 2D sensitivity study and near wellbore cooling management . . . . .	30
4.4.2	P18-4 test case . . . . .	31
4.4.3	Case overview and incorporated physics. . . . .	31
<b>5</b>	<b>Simulation results and discussion</b>	<b>32</b>
5.1	1D sensitivity study . . . . .	32
5.1.1	Base case - Reservoir dynamics: thermal effects, flow behavior and phase change. . . . .	32
5.1.2	Injection rate. . . . .	35
5.1.3	Injection temperature . . . . .	35
5.1.4	Permeability . . . . .	35
5.1.5	Porosity . . . . .	36
5.1.6	Initial reservoir pressure and temperature . . . . .	37
5.1.7	Reservoir size . . . . .	38
5.1.8	Brine saturation . . . . .	39
5.1.9	Salt precipitation. . . . .	40
5.1.10	Relative permeability . . . . .	41
5.1.11	Rock thermal properties . . . . .	41
5.1.12	Capillary pressure . . . . .	41
5.1.13	1D Sensitivity study results analysis . . . . .	43
5.2	2D sensitivity study . . . . .	44
5.2.1	Homogeneous model . . . . .	44
5.2.2	3-layer model . . . . .	46
5.2.3	Heterogeneous model . . . . .	47
5.3	Influence of dry-out and salt precipitation on effective permeability . . . . .	49
5.4	Simulator comparison . . . . .	50
5.4.1	Comparison of JTC between analytical solution and numerical models . . . . .	50
5.4.2	Comparison of ECO2MG and GEM simulation results . . . . .	51
<b>6</b>	<b>Near wellbore cooling management</b>	<b>53</b>
6.1	Injection scenarios . . . . .	54
6.1.1	Variable injection rate with fixed injection temperature . . . . .	54
6.1.2	Variable injection temperature with fixed flow rate . . . . .	55
6.2	Impurities in CO <sub>2</sub> injection stream . . . . .	55
<b>7</b>	<b>P18-4 test case</b>	<b>60</b>
7.1	Model initialization . . . . .	61
7.1.1	Local grid refinement . . . . .	61
7.1.2	Permeability matching. . . . .	61
7.1.3	Initial pressure, temperature and water saturation. . . . .	62
7.1.4	Relative permeability and capillary pressure curves . . . . .	62
7.2	Simulation results. . . . .	63
7.2.1	CO <sub>2</sub> flow, near wellbore cooling and pressure behavior . . . . .	63
7.2.2	Well location . . . . .	65
<b>8</b>	<b>Discussion</b>	<b>66</b>
<b>9</b>	<b>Conclusions</b>	<b>68</b>
<b>10</b>	<b>Recommendations and future work</b>	<b>70</b>
	<b>Bibliography</b>	<b>71</b>
<b>A</b>	<b>Appendix</b>	<b>78</b>
A.1	Mutual solubility CO <sub>2</sub> -brine . . . . .	78
A.2	Mutual solubility CH <sub>4</sub> -brine . . . . .	79
A.3	Peng-Robinson EOS for non-aqueous phase fugacity coefficient determination . . . . .	79

---

<b>B Appendix</b>	<b>81</b>
B.1 Derivation of analytical solution for Joule-Thomson cooling . . . . .	81
<b>C Appendix</b>	<b>83</b>
C.1 Modified phase envelopes in ECO2MG . . . . .	83
<b>D Appendix</b>	<b>84</b>
D.1 Comparison between CO <sub>2</sub> -brine and CO <sub>2</sub> -CH <sub>4</sub> -brine systems . . . . .	84
D.2 Permeability reduction parameters and temperature profiles . . . . .	85
D.3 Relative permeability curves and temperature profiles . . . . .	85
D.4 Rock thermal parameters and temperature profiles . . . . .	87
<b>E Appendix</b>	<b>88</b>
E.1 Realistic CO <sub>2</sub> bottom hole injection temperature . . . . .	88
E.2 Impure CO <sub>2</sub> injection temperature profiles . . . . .	88
E.2.1 90 mole% CO <sub>2</sub> and 10 mole% impurity at 35 kg/s . . . . .	88
E.2.2 95 mole% CO <sub>2</sub> and 5 mole% impurity at 10 kg/s . . . . .	89
<b>F Appendix</b>	<b>90</b>
F1 Effect of grid refinement . . . . .	90
F2 Effect of well location and reservoir geometry. . . . .	90

# List of Figures

1.1	Carbon dioxide concentration in the atmosphere over the last decades. . . . .	1
1.2	Overview of subsurface storage options. . . . .	2
1.3	Trapping mechanisms of CO <sub>2</sub> in geological formations. . . . .	2
1.4	Gas field pressure responses during production for various degrees of aquifer support. . . . .	3
1.5	Map of platforms in the Dutch North Sea connected to depleted gas fields characterized as potential location for CO <sub>2</sub> sequestration. . . . .	5
2.1	(left) Phase envelopes of CO <sub>2</sub> -CH <sub>4</sub> mixtures for different mixture compositions, obtained from WinProp 2017 and (right) phase diagram for pure CO <sub>2</sub> . . . . .	8
2.2	Density (left top), viscosity (right top) and specific enthalpy (bottom) for different mixture compositions in mole fraction ranging from pure CO <sub>2</sub> to pure CH <sub>4</sub> at different temperatures in °C. . . . .	8
2.3	(left) Density of brine with 15 wt% NaCl plotted over pressure for different temperatures and (right) viscosity and specific enthalpy of brine plotted over temperature. . . . .	9
2.4	(left) Heat of dissolution ( $\Delta H_{sol}$ ) obtained from experimental data as a function of temperature for various brine salinities and pressures; (right) Heat of water vaporization ( $\Delta H_{vap}$ ) for pure water according to IAPWS-95. . . . .	10
2.5	(a) Conceptual model of pore-body and pore-throat in rocks and the 'tubes-in-series' configuration in the Verma-Pruess model; (b) Permeability reduction as function of the solid saturation; (c) Schematic representation of a pore-body to pore-throat combination with uniformly distributed salt precipitation. . . . .	13
3.1	Concatenation of processes and parameters affected by the perturbation of the temperature and pressure in the system caused by CO <sub>2</sub> injection. . . . .	20
3.2	Overview of potential effects arising in the near wellbore region as a consequence of CO <sub>2</sub> injection. . . . .	21
3.3	Joule-Thomson coefficients of pure CO <sub>2</sub> based on experimental data. . . . .	22
3.4	(a) Schematic phase diagram of a binary pure CO <sub>2</sub> -brine and CH <sub>4</sub> -brine system for different salinity values; (b) Hydrate stability curves for pure CO <sub>2</sub> and mixtures with real natural hydrocarbon gas from a North Sea field. . . . .	24
4.1	Schematic representations of CO <sub>2</sub> injection in a saline aquifer (a) and depleted gas reservoir with initial CH <sub>4</sub> (b), including the component exchange between phases due to vaporization, dissolution and chemical reactions. . . . .	28
4.2	Overview of the phase combinations and transitions captured by ECO2MG and GEM (excluding the solid salt phase). . . . .	29
4.3	Overview of the sequence of performed simulation studies in this research, in which the simulator utilized for each study is indicated. . . . .	30
4.4	Radial model including the logarithmic grid distribution implemented in the 1D sensitivity study, injection rate scenarios and impurity simulations. . . . .	30
5.1	(top) Components and saturation distribution after 1 year of injection for a simulation in which all thermal effects are enabled and (bottom) temperature and pressure profiles in the reservoir after 1 year of injection for 3 simulations with different thermal effects included. . . . .	33
5.2	(left) Temperature profiles at different times during the injection process for a reservoir with a radius of 1000 m and (right) corresponding pressure profiles in which the red line indicates the critical pressure of CO <sub>2</sub> . . . . .	35
5.3	(a) Temperature, pressure and salt distribution for different CO <sub>2</sub> injection rates; (b) Temperature, pressure and salt distribution for different formation permeabilities. . . . .	36

5.4	(a) Temperature, pressure and mole fraction of water in the non-aqueous phase and (b) saturation distributions for different CO <sub>2</sub> injection temperatures after 1 year of injection. . . . .	37
5.5	(left) Temperature profile for different rock porosity values and (right) corresponding pressure and solid salt profiles. . . . .	37
5.6	(a) Temperature and pressure profiles for different initial reservoir pressures; (b) Temperature and pressure profiles for different initial reservoir temperatures. . . . .	38
5.7	(a) Temperature and pressure profiles for different reservoir sizes ; (b) Temperature, pressure and saturation distribution for different initial brine saturations. . . . .	39
5.8	(a) Temperature and pressure profiles for different brine salinities; (b) Salt precipitation and corresponding permeability reduction profiles; (c) Saturation distribution over time at a radial distance of 10 m with respect to the well. . . . .	40
5.9	(a) Temperature and pressure distribution for different capillary pressures and (b) implemented capillary pressure curves. . . . .	42
5.10	(left) Saturation distribution of the non-aqueous phase, aqueous phase, solid saturation and dissolved salt concentration for the simulation case with mobile brine and capillary pressure (CP1) after 1 year of injection; (right) Fluxes of the injected CO <sub>2</sub> , aqueous phase and dissolved salt plotted on a logarithmic scale after 1 year of injection. . . . .	43
5.11	(left) Precipitated salt and corresponding permeability reduction in the near wellbore region for different capillary pressure curves after 1 year of injection; (right) Displacement ratio and salt precipitated in the dry-out zone for an immobile and mobile case with capillary pressure (CP2) plotted as function of the flow rate. . . . .	43
5.12	Permeability models for the homogeneous (left), 3-layer (middle) and heterogeneous (right) simulation cases. In the 3-layer model the non permeable layers are indicated with black and the permeability distribution from top to bottom is 1 mD, 10 mD and 100 mD respectively. . . . .	44
5.13	(a) 2D temperature profiles for a homogeneous reservoir after 1, 5 and 10 years of injection and (b) pressure, density, water saturation and solid saturation profiles after 5 years of injection. . . . .	45
5.14	Temperature profiles for different $K_v/K_h$ ratios after 5 years of injection at initial reservoir pressures of 40 and 70 bar. . . . .	45
5.15	Temperature profiles for simulations with (left) and without (right) heat exchange with the confining over- and underburden formations after 5 years of injection. . . . .	46
5.16	(a) Permeability field for the 3-layered system with a permeability distribution from top to bottom of 1 mD, 10 mD and 100 mD respectively and (b) corresponding temperature profile after 5 years of injection. . . . .	46
5.17	Pressure, density of the NA phase, CO <sub>2</sub> mole fraction in the NA phase and solid saturation profile for the 3-layer model after 5 years of injection. . . . .	47
5.18	(a) Heterogeneous permeability field and (b) temperature profile including CO <sub>2</sub> mass flux vectors and streamlines after 5 year of injection. . . . .	48
5.19	Pressure, CO <sub>2</sub> mole fraction in the non-aqueous phase, aqueous phase saturation and solid saturation profiles for the heterogeneous model after 5 years of injection. . . . .	48
5.20	(a) Permeability reduction due to salt precipitation as a function of initial water saturation at different salinities; (b) The absolute increase in relative permeability caused by water vaporization with respect to the initial relative permeability in presence of a brine phase; (c) Fractional change in effective permeability as a consequence of relative permeability increase and absolute permeability decrease; (d) Effective permeability change between the initial situation (without dry-out and salt precipitation) and after dry-out and salt precipitation for different water saturations and salinities. . . . .	49
5.21	Comparison of the analytical solution (solid), ECO2MG (dashed) and GEM (dotted). . . . .	51
5.22	(a) Temperature profiles and (b) pressure and non-aqueous phase composition profiles obtained from ECO2MG and GEM with and without permeability reduction after 1 year of injection, with equivalent model geometries and simulation parameters. . . . .	51
5.23	(a) Permeability reduction and (b) aqueous phase saturation simulated obtained from ECO2MG and GEM after 1 year of injection, with equivalent model geometries and simulation parameters. . . . .	52

6.1	(a) Injection rate plotted over time for the variable injection rate scenario (solid lines) and base case scenario with fixed injection rate (dashed lines) and (b) Injection temperature for the variable injection temperature scenario (solid lines) and base case with fixed injection temperature (dashed lines). . . . .	54
6.2	Minimum reservoir temperature and corresponding pressure for the 3 injection scenarios considered, in which the dots represent the pressure and temperature condition at consecutive time steps of one month and the solid lines mark the outer boundaries of the hydrate formation region. . . . .	55
6.3	Joule-Thomson coefficient (solid) and specific heat capacity (dotted) of different pure components at a fixed temperature of 318K. . . . .	56
6.4	Density and enthalpy values of the CO <sub>2</sub> /impurity mixtures for various mixture compositions at 318K and 50 bar. . . . .	56
6.5	(a& b) Temperature and pressure profiles for the various impurities with injection composition of (95 mole% CO <sub>2</sub> + 5 mole% impurities) and for pure CO <sub>2</sub> after 1 year of injection at 35 kg/s; (c) Dissolution profile of the impurities in the aqueous phase and (d) profile of H <sub>2</sub> O components in the non-aqueous phase. . . . .	58
6.6	Temperature, pressure and compressibility profiles for a realistic CO <sub>2</sub> mixture with impurities injected in a pure methane reservoir (mixture), pure CO <sub>2</sub> injected in reservoir with a realistic natural gas composition (real gas) and pure CO <sub>2</sub> injected in a pure methane reservoir (original). . . . .	59
7.1	(left) Areal view of the complete P18 field in which the P18-4 compartment is indicated by the red box and (right) 3D view of the P18-4 compartment including the well location with an arbitrary color scheme. . . . .	60
7.2	P18-4 cross section in NW-SE direction intersecting the well. . . . .	61
7.3	Capillary pressure and relative permeability curves for each of the porosity classes, implemented in the P18-4 simulation model. . . . .	62
7.4	CO <sub>2</sub> distribution in the reservoir over time. . . . .	63
7.5	Temperature distribution plotted over time in a zoomed cross section (NW-SE direction) parallel to the reservoir boundary intersecting the well, wherein the perforated cells are indicated by the black dots. . . . .	63
7.6	Pressure distribution in the reservoir over time in areal perspective, where the well location is indicated by the green dot. . . . .	64
7.7	Comparison of field model (left top), radial model with parameters matching to the field model (right top) and radial model equivalent to the sensitivity study (bottom). . . . .	64
7.8	(left) Temperature and pressure profile for the original and modified well location after 1 year of injection and (right) position of the original (red) and modified well (yellow) in the P18-4 field. . . . .	65
A.1	Mutual solubility of CO <sub>2</sub> in the aqueous brine phase in molal (left) and H <sub>2</sub> O in the non-aqueous CO <sub>2</sub> -rich phase (right) for various pressures, temperatures and brine salinities. . . . .	78
A.2	Mutual solubility of CH <sub>4</sub> in the aqueous brine phase in molal and H <sub>2</sub> O in the CH <sub>4</sub> -rich phase (bottom-right) for various pressures, temperatures and brine salinities. . . . .	79
C.1	Modified CO <sub>2</sub> -CH <sub>4</sub> phase envelopes in ECO2MG. . . . .	83
D.1	Temperature and pressure profiles for a CO <sub>2</sub> -brine system (dashed lines) and original CO <sub>2</sub> -CH <sub>4</sub> -brine (solid lines) for an initial pressure of 40 bar (i.e. subcritical conditions) and 100 bar (i.e. supercritical conditions). . . . .	84
D.2	(a) Temperature and pressure profiles for the tested permeability reduction function parameters and (b) zoomed section of the temperature curve and the calculated permeability reduction due to salt precipitation. . . . .	85
D.3	Relative permeability curves utilized to study the sensitivity with respect to the relative permeability. . . . .	86
D.4	Temperature and pressure profile for different relative permeability curves. . . . .	86
D.5	Temperature profiles for (a) different densities, (b) specific heat capacities and (c) thermal conductivities of the formation after 1 year of injection. . . . .	87

---

E.1	Bottom hole temperature for a CO <sub>2</sub> injection well of approximately 3200 m depth versus flow rate at different initial reservoir temperatures with an initial surface CO <sub>2</sub> injection temperature of 4°C. . . . .	88
E.2	Temperature and pressure profile for an injected CO <sub>2</sub> stream with a composition of 90 mole% CO <sub>2</sub> and 10 mole% impurity after 1 year of injection at 35 kg/s. . . . .	88
E.3	Temperature and pressure profile for an injected CO <sub>2</sub> stream with a composition of 95 mole% CO <sub>2</sub> and 5 mole% impurity after 1 year of injection at 10 kg/s. . . . .	89
F.1	Pressure and temperature profiles for a grid with different refinement levels of the cell perforated by the well. . . . .	90
F.2	Geometries of the different reservoirs tested ranging from a symmetric to an highly elongated reservoir with approximately the same volumes. . . . .	91
F.3	Pressure profiles for the various reservoir geometries illustrated in figure F.2 after 1 year of injection. . . . .	91



# Introduction

In the last decades the concentration of carbon dioxide ( $\text{CO}_2$ ) in the atmosphere significantly increased (see figure 1.1), as a result of anthropocentric emission by combustion of excessive amounts of fossil fuels [1].  $\text{CO}_2$  is recognized as a greenhouse gas (GHG) responsible for absorption and emission of thermal radiation. Hence, the concentration of  $\text{CO}_2$  has a significant impact on the atmosphere's energy balance and intensifies the greenhouse effect leading to global warming [2]. Global warming is one of the most complex issues of today's society. Based on the continuously increasing global energy demand, which can at the current stage of development only be partly covered by sustainable energy sources, the  $\text{CO}_2$  emission is forecasted to rise in the upcoming decades at vexatious rates [3].

Mitigation of supplementary accumulation of  $\text{CO}_2$  in the atmosphere is necessary to prevent the occurrence of irreversible climate issues. A feasible solution is storage of  $\text{CO}_2$  in geological formations, eliminating emission into the atmosphere. Depleted gas fields proved to have suitable characteristics for safe and permanent storage of  $\text{CO}_2$  [4]. To ensure long term integrity of the storage, it is necessary that the combination of reservoir and fluid behavior during and after the injection phase is properly understood, modeled and monitored.

Geological storage forms the final stage in the Carbon dioxide Capture and Storage (CCS) chain. CCS comprises the entire process from the  $\text{CO}_2$  source to geological storage. In Europe, application of geological storage of  $\text{CO}_2$  would obviate roughly 47% of the yearly emissions into the atmosphere [5].

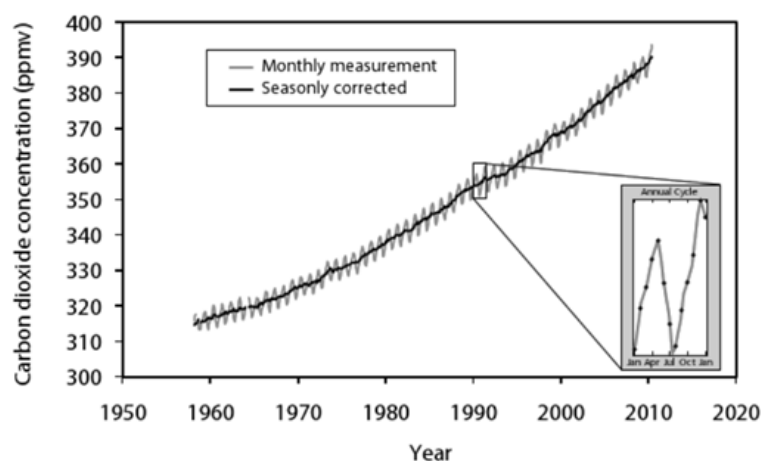


Figure 1.1: Carbon dioxide concentration in the atmosphere over the last decades [6].

## 1.1. Subsurface CO<sub>2</sub> storage

The subsurface has significant potential to permanently store substantial volumes of captured CO<sub>2</sub> in a safe manner. Geological formations considered as targets for CO<sub>2</sub> sequestration are characterized by large storage capacities, reasonable formation properties and excellent trapping features, minimizing the chances of leakage to the surface [7]. Different geological settings eligible for CO<sub>2</sub> storage are (see figure 1.2) [4]:

- Saline aquifers
- Oil and gas reservoirs
- Coal beds (ECBM)
- Salt structures

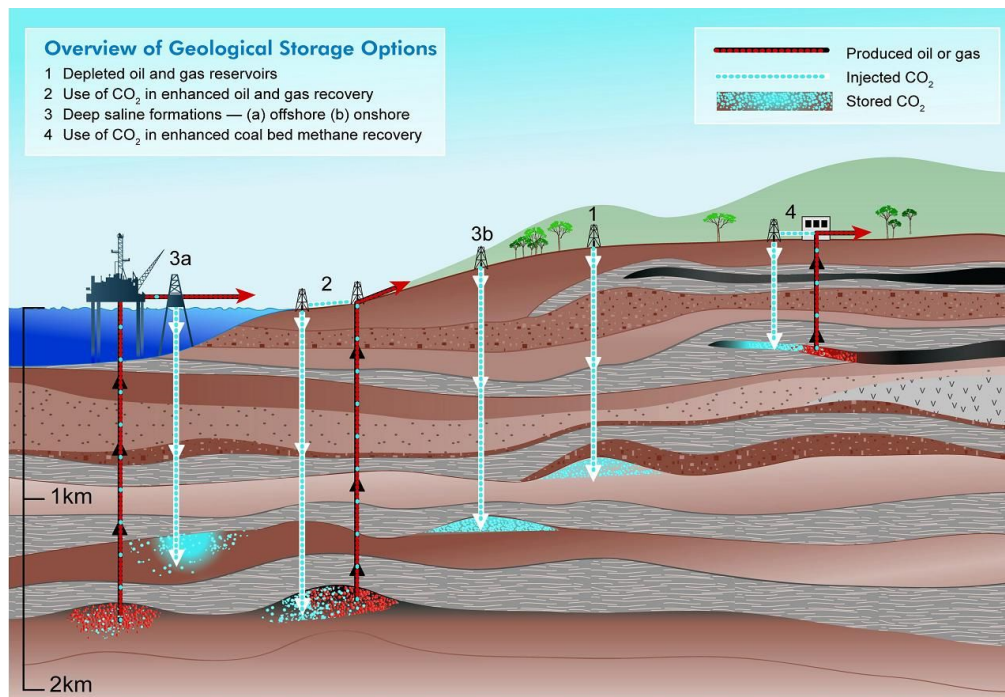


Figure 1.2: Overview of subsurface storage options [4].

Various storage mechanisms have been identified for CO<sub>2</sub> sequestration in geological formations [4]. These are: (1) *Structural and stratigraphic trapping*, where CO<sub>2</sub> migration is obstructed by structural and stratigraphic features as faults, folds or pinched-out formations; (2) *Capillary trapping*, where CO<sub>2</sub> is immobilized at residual saturation by capillary forces; (3) *Solubility trapping*, where the CO<sub>2</sub> gets trapped by dissolving into the formation brine; (4) *Mineral trapping*, where the dissolved CO<sub>2</sub> is fixated in minerals after reacting with rock minerals and formation fluids. Figure 1.3 provides an overview of the trapping mechanisms including their corresponding time scales and storage securities.

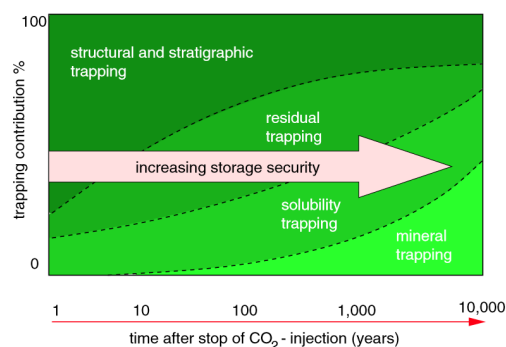


Figure 1.3: Trapping mechanisms of CO<sub>2</sub> in geological formations [8].

### 1.1.1. Aquifer versus hydrocarbon reservoir storage

The primary locations for geological CO<sub>2</sub> storage are saline aquifers and depleted hydrocarbon reservoirs. Saline aquifers typically offer higher storage capacities compared to depleted hydrocarbon reservoirs because of their larger volumes. In addition, saline aquifers are more abundantly present in the subsurface [4]. However, in contrast to hydrocarbon reservoirs, for the majority of the saline aquifers sealing capacities are unsure because of the absence of validation data. Due to the lack of data and absence of onsite facilities on most saline aquifers, the short-term practical implementation of CO<sub>2</sub> sequestration in depleted hydrocarbon reservoirs tends to be more straightforward [9].

A large contrast exists in characteristic properties between saline aquifers and depleted hydrocarbon reservoirs. Generally the reservoir pressure of aquifers are at or above hydrostatic pressure. This in contrast to the typically low pressures of depleted hydrocarbon reservoirs. The reservoir pressure affects the physical phenomena during and after CO<sub>2</sub> injection and injection in highly pressurized reservoir can be precarious. Absence of residual hydrocarbons in saline aquifers significantly influence the modeling complexity by altering the occurrence physical phenomena and geochemical reactions. In saline aquifers, the flow system can be usually reduced to two phase CO<sub>2</sub>-brine problems, which is contrary to hydrocarbon reservoirs where three or more phases can coexist.

### 1.1.2. Hydrocarbon reservoir types and storage options

CO<sub>2</sub> can be injected purely for permanent storage in hydrocarbon reservoirs. However, CO<sub>2</sub> can also be utilized as driving substance in enhanced oil recovery (EOR) or enhanced gas recovery (EGR) methods, enhancing ongoing hydrocarbon recovery for fields on stream while simultaneously storing CO<sub>2</sub>. Main differences between EOR and CO<sub>2</sub> storage projects in depleted fields are the operational conditions and residual saturations of the reservoir fluids. EOR and EGR processes operate at higher reservoir pressures compared to storage processes in depleted fields.

The type of hydrocarbons in hydrocarbon reservoirs (i.e. oil or gas) significantly impacts the CO<sub>2</sub> sequestration process. It affects the dynamic storage capacity in terms of compressibility, oil is less compressible than gas, and miscibility. Modeling of CO<sub>2</sub> injection in oil reservoir is more complex than gas reservoirs. This is caused by presence of additional gas besides the residual oil under depleted conditions, primarily if the oil bubble point has been reached. Consequently, high order multi-phase systems arise due to the existence of the residual oil phase, impacting the CO<sub>2</sub> flow behavior and injectivity [10].

#### Gas reservoirs: driving mechanisms

Different driving mechanisms can be distinguished for natural gas reservoirs based on the amount of aquifer support provided to the reservoir, ranging from depletion driven (no aquifer support) to entirely water driven (strong aquifer support). Other uncommon mechanisms as slow gas and tight gas are disregarded here. The drive mechanism determines the reservoir pressure response during production, well shut-in and subsequently at the onset of CO<sub>2</sub> injection (see figure 1.4) [9]. This remaining reservoir pressure at the onset of CO<sub>2</sub> injection plays an important role in the magnitude and type of thermophysical phenomena occurring in the near wellbore region and further in the reservoir during the injection process.

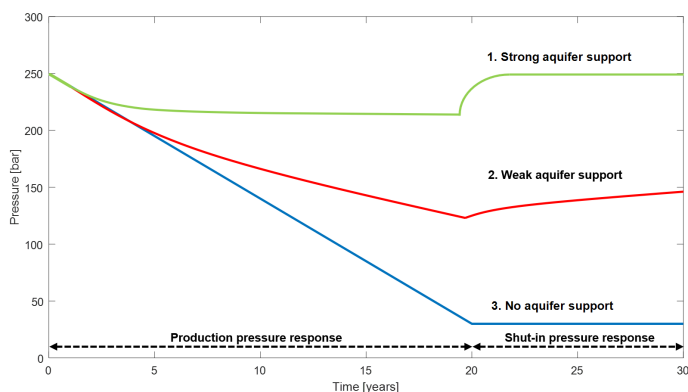


Figure 1.4: Gas field pressure responses during production for various degrees of aquifer support, modified after [9].

### Water drive

In water driven gas reservoirs, the reservoir pressure remains fairly constant and close to hydro-static conditions throughout the production processes due to the continuous water influx from a connected aquifer. Recovery factors for water driven gas reservoirs are therefore typically low, approximately 60%. Strong water influx reduces production from gas well as a result of water coning around and into the well. Hence, watering-out the gas well and preventing production of the remaining gas in place. Nevertheless, the water-drive reservoirs, having a substantial residual gas saturation, tend to be suitable candidates for CSEGR (i.e. CO<sub>2</sub> injection combined with gas production) [9, 11].

### Depletion drive

During gas production from depletion driven gas fields, the reservoir pressure declines due to the absence of water influx and low pressures can be reached. Accordingly, watering-out problems of the gas production well will not be encountered and a reasonable gas recovery of roughly 90% can be achieved [11].

## 1.2. CO<sub>2</sub> storage potential in Dutch North Sea depleted gas fields

The Netherlands contains a large number of exploited gas fields (> 190) and is mainly due to the Groningen gas field one of the largest producers of natural gas in Europe. The majority of these gas fields are close to the end of their production life cycle or already fully depleted and could be utilized for storage of CO<sub>2</sub> [12]. Within The Netherlands more than 150 fields are characterized as potential subsurface storage location having a total storage capacity of 2.7 Gt (excluding the Groningen gas field and natural gas storage location), of which 1.7 Gt is available in offshore fields (see table 1.1). In theory the number of fields and total storage capacity is significantly higher. However, tight reservoirs with a permeability less than 100 mDm are excluded based on practical considerations. CCS in The Netherlands mainly focuses on the storage of CO<sub>2</sub> in offshore depleted gas fields. Aquifers identified as suitable for CO<sub>2</sub> storage in The Netherlands are scarce, but this may change in the future. Nearly all of the offshore gas field considered for storage are depletion driven reservoirs, thus having exceptionally low reservoir pressures after depletion at onset of the CO<sub>2</sub> injection phase. In figure 1.5, an overview is provided of the locations of platforms connected to offshore fields characterized as potential storage locations. For national implementation of CCS the large offshore fields with high capacities (> 100 Mt) and favorable reservoir properties (mainly located in the K and L blocks), and fields close to shore (P and Q blocks) are the main targets [13].

Presently, CO<sub>2</sub> is only being injected in the K12-B field. However, due to the limited (re-)injection rate of the locally produced CO<sub>2</sub>, as byproduct of natural production, this pilot project is not comparable to the injection rates targeted. Detailed feasibility studies have been conducted on the offshore P18-4 field in the vicinity of the Port of Rotterdam as part of the ROAD project and a storage license was provided for injection of 5 Mt CO<sub>2</sub> over a time-span of 5 years. But, due to limited funding the project is currently canceled [12].

In the recently published 2017 coalition agreement, the Dutch government decided to set a new environmental goal stating that in 2030 at least 20 Mt should be stored yearly in Dutch offshore fields. Consequently, supplementary subsidies and investments will be provided in the upcoming years, stimulating research and pilot projects concerning CCS.

Table 1.1: Dutch CO<sub>2</sub> storage capacity onshore and offshore (excluding the Groningen gas field and natural gas storage locations) [13].

Location	Offshore		Onshore	
	Capacity (Gt)	No. of fields	Capacity (Gt)	No. of fields
Theoretical storage capacity	2.2	222	1.4	172
Practical storage capacity	1.7	104	1.1	54

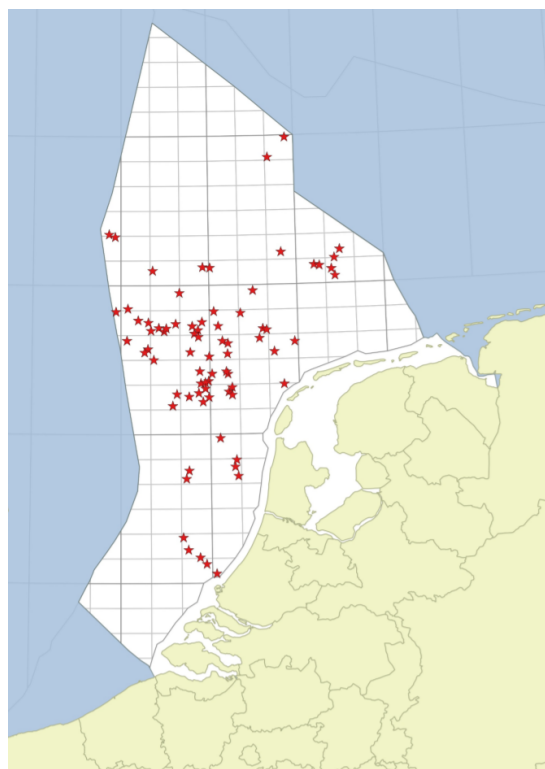


Figure 1.5: Map of platforms in the Dutch North Sea connected to depleted gas fields characterized as potential location for CO<sub>2</sub> sequestration [13].

### 1.3. Prior research on the modeling of geological CO<sub>2</sub> storage

Research on geological CO<sub>2</sub> sequestration accelerated over the last 25 years. Geological CO<sub>2</sub> storage is a broad and complex issue comprising various facets ranging from thermophysical transport phenomena to geochemical and geomechanical processes. Significant effort has been made on numerical modeling of CO<sub>2</sub> flow and transport in geological formations [6]. Numerous numerical models have been extensively examined and benchmarked [8]. However, the majority of the available simulators incorporate thermodynamic models explicitly for CO<sub>2</sub>-brine systems only applicable to aquifer storage. In addition, many models incorporate only part of the relevant (thermo)physical processes involved and explicitly focus on one particular effect. Hence, the effects are primarily studied individually despite their strongly coupled nature. Injection of CO<sub>2</sub> disturbs local equilibria and induces thermophysical effects influencing the injectivity. Numerical models and laboratory experiments were developed and conducted to investigate induced effects as salt precipitation [14–16], hydrate formation [17–19] and thermal or hydraulic fracturing [20–22]. Due to the significant dependency of the thermophysical properties of CO<sub>2</sub> on pressure and temperature, a comprehensive understanding of non-isothermal processes along all the elements within the CCS chain and especially within the near wellbore region is necessary [23, 24]. Recently, much attention is paid to CO<sub>2</sub> sequestration in depleted gas fields and CO<sub>2</sub> in EGR applications which require a different modeling approach due to the presence of methane in the thermodynamic model and the generally low pressure of depleted fields [9, 25, 26]. The CMG GEM simulator claims to be capable of coupling most of the mentioned effects in presence of methane, while entirely accounting for thermal effects as dissolution, vaporization and the Joule-Thomson (JT) effect [27]. Moreover, the TOUGH simulator, extensively utilized to simulate aquifer storage [28] has been extended to include a thermodynamic model with methane, also enabling analysis of (thermal) effects (e.g. the JT effect) in presence of methane [29–32]. The occurrence of the previously mentioned JT effect and its magnitude during CO<sub>2</sub> injection at depleted conditions was tested in an experimental core scale study [33]. Likewise, an analytical solution was developed for rapid determination of the JT effect at depleted conditions [34].

## 1.4. Research objectives

Prior to large-scale storage of CO<sub>2</sub> in depleted gas fields in the Dutch North Sea, proper research is required to define the physical impact of the highly coupled potential near wellbore effects as a consequence of CO<sub>2</sub> injection. This study focuses particularly on depletion driven methane reservoirs at low depleted reservoir pressures (<50 bar; below the critical point of CO<sub>2</sub>), abundantly present in the Dutch North Sea. In this research, a time scale is considered corresponding to the injection period, i.e. 0 to approximately 20 years. Certain near wellbore effects arising during this injection period can potentially impair the formation in the vicinity of the injector, having a detrimental impact on the injectivity of CO<sub>2</sub>, while other effects can enhance the injectivity. Knowledge acquired via this research on the physical impact of CO<sub>2</sub> injection at the depleted conditions considered can be utilized to take precautionary measures to mitigate or prevent several of the detrimental near wellbore effects (e.g. by changes of operating conditions). Eventually this would shorten the CO<sub>2</sub> injection time-span and enhance processes safety, hereby forming an essential element in the national deployment of CCS. Hence, the following research objectives are formulated:

- Determine and quantify the potential near wellbore effects provoked by injection of CO<sub>2</sub> in depleted gas reservoirs;
- Perform a sensitivity study on the parameters affecting potential near wellbore effects to determine dominant factors;
- Study the thermophysical influence of the presence of methane and other components in the reservoir or CO<sub>2</sub> stream on the magnitude of the near wellbore effects with respect to CO<sub>2</sub>-brine systems;
- Define the consequences of the near wellbore effects on the injectivity of CO<sub>2</sub>;
- Characterize optimal injection conditions to mitigate potential detrimental effects.

This research starts with a theoretical explanation of potential near wellbore effects induced by CO<sub>2</sub> injection including the underlying thermophysical phenomena and governing equations (chapter 2 and 3). Thereafter, the utilized numerical simulators and obtained results of a sensitivity study on CO<sub>2</sub> injection in a depleted reservoir are discussed (chapter 4 and 5). Then, a section is devoted to potential factors and conditions that can be altered to control near wellbore effects (chapter 6) and afterwards an injection test case is performed on the P18-4 field (chapter 7). The simulations are subsequently briefly discussed (chapter 8). Finally, a conclusion is drawn on the probability of the occurrence and related magnitude of the near wellbore effects considered and the corresponding influence of these effects on the injectivity (chapter 9) and recommendations are provided (chapter 10).

Several software programs are utilized to conduct this study. Modeling of CO<sub>2</sub> injection in the subsurface is performed with the aid of an academic and a commercial reservoir simulator, i.e. TOUGH2-ECO2MG and CMG GEM respectively. For visualization and analysis of the simulation results MATLAB is used. This thesis forms the first step for EBN to integrated CCS modeling, from capture to storage.

# 2

## Fluid-rock characteristics and governing equations

Precise modeling of non-isothermal processes during CO<sub>2</sub> injection in depleted gas reservoirs is essential due to the strong dependency of the fluid properties (e.g. density, viscosity and solubility) on the local temperature and pressure conditions. These fluid properties control the transport and thermophysical processes in the reservoir.

### 2.1. Characteristic properties of CO<sub>2</sub>, CH<sub>4</sub>, brine and their mixtures

#### 2.1.1. Phases and components

Injection of CO<sub>2</sub> in a depleted gas reservoir system resembles a multi-component multi-phase system. Several phases can be distinguished in the reservoir during a CO<sub>2</sub> injection process depending on the local conditions, i.e. a liquid aqueous phase (Aq), a non-aqueous liquid phase (NA<sub>L</sub>), a non-aqueous vapor phase (NA<sub>V</sub>) and a separate solid salt phase (s). The aqueous phase is formed mainly by water (H<sub>2</sub>O), wherein dissolved salt components and traces of non-aqueous components (i.e. CO<sub>2</sub> and CH<sub>4</sub>) can be present. On the other hand, the non-aqueous phases consists of a mixture of the non-aqueous components (CO<sub>2</sub>-CH<sub>4</sub>), of which the composition can vary from pure CO<sub>2</sub> to pure CH<sub>4</sub>. The non-aqueous phase can contain some additional dissolved or vaporized H<sub>2</sub>O components. Besides, the solid phase comprises only precipitated salt. The mentioned phases can coexist inside the reservoir in numerous configurations, varying from a single phase system (i.e. only the aqueous phase) to a four phase system where the liquid aqueous phase, non-aqueous phases in both liquid and vapor conditions and solid phase are present. In a real gas reservoir, more components are present in the system than described above. However, for convenience and brevity, the components treated are restricted to solely the essential components necessary to adequately describe the system.

#### 2.1.2. CO<sub>2</sub>-CH<sub>4</sub> phase behavior

Introduction of CO<sub>2</sub> in an initially filled CH<sub>4</sub> reservoir induces formation of a multi-component mixture consisting of CO<sub>2</sub>-CH<sub>4</sub> and traces H<sub>2</sub>O vaporized from the aqueous phase. For pure components, the vapor-liquid equilibrium (VLE) can be simply described by a vapor pressure curve separating the vapor and liquid phase in a pressure temperature diagram (see figure 2.1 (right)). However, for mixtures phase envelopes are defined (see figure 2.1 (left)). VLE characteristics of a CO<sub>2</sub>-CH<sub>4</sub> mixture deviate from the characteristics of its pure components. The phase envelopes, which consists of a dew-point and bubble point line originating from the critical point, enclose the two phase liquid-vapor region. At the critical point the phases are in equilibrium and have an identical composition. A cricondentherm and cricondenbar can be specified on the outline of the phase envelope. The former indicates the maximum temperature for which liquid can coexist with vapor while the latter indicates the maximum pressure for which vapor can coexist with liquid. Above the critical pressure and temperature the substance in supercritical phase. The critical pressure and temperature of pure CO<sub>2</sub> are 73.9 bar and 31.1°C respectively. Within the range of temperature and pressure conditions encountered in depleted gas reservoirs, multiple phases can coexistence. Changes of these conditions caused by the CO<sub>2</sub> injection can induce phase transitions to occur in the reservoir.

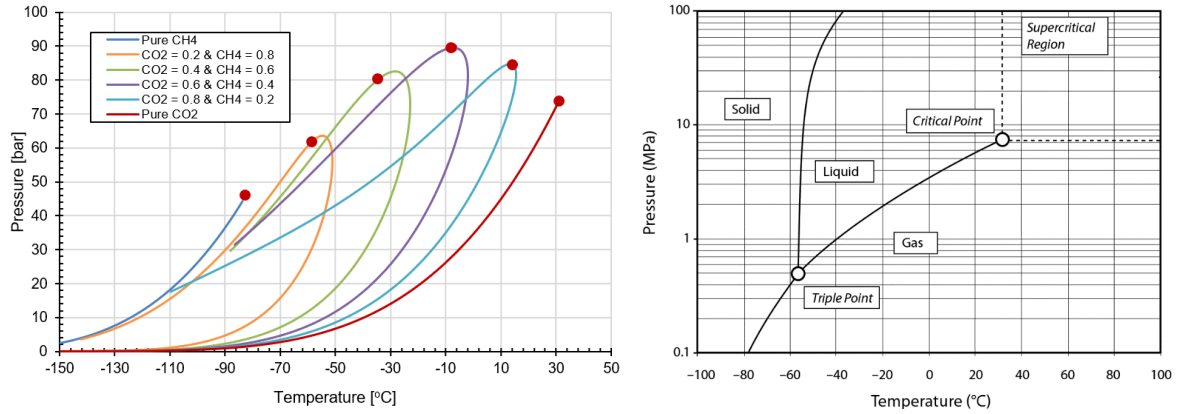


Figure 2.1: (left) Phase envelopes of CO<sub>2</sub>-CH<sub>4</sub> mixtures for different mixture compositions, obtained from WinProp 2017 [27] and (right) phase diagram for pure CO<sub>2</sub> [6].

### 2.1.3. Thermodynamic properties CO<sub>2</sub> and CH<sub>4</sub>

The thermodynamic properties of a mixture highly depend on the pressure and temperature condition and are closely correlated to its composition. Essential thermodynamic properties (i.e. density, viscosity and specific enthalpy) of the pure components and mixture with a 0.66 mole fraction of CO<sub>2</sub> are shown in figure 5.22 at different temperatures.

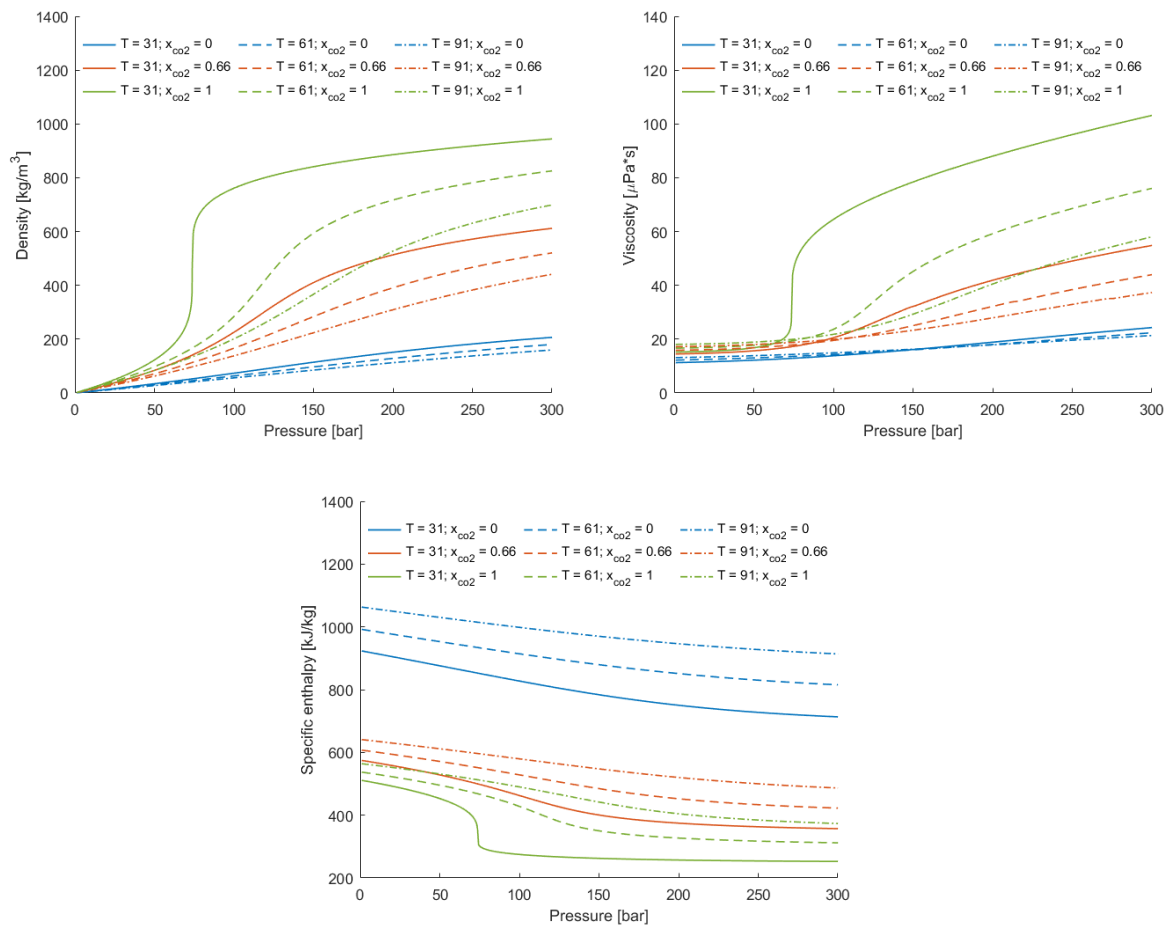


Figure 2.2: Density (left top), viscosity (right top) and specific enthalpy (bottom) for different mixture compositions in mole fraction ranging from pure CO<sub>2</sub> to pure CH<sub>4</sub> at different temperatures (°C), obtained from [35].

In the given pressure and temperature range (i.e. 31 to 91°C and 0 to 300 bar), both the density and viscosity of CO<sub>2</sub> are higher compared to CH<sub>4</sub>, while the enthalpy of CO<sub>2</sub> is lower. As the CO<sub>2</sub> reaches critical pressure the density, viscosity and enthalpy abruptly change, in particular at lower temperatures, which is attributed to the phase transition of CO<sub>2</sub>. The properties of the CO<sub>2</sub>-CH<sub>4</sub> mixture scale between the values of pure CO<sub>2</sub> and CH<sub>4</sub>.

### 2.1.4. Properties of brine

The thermodynamic properties of brine slightly deviate from pure water due to presence of dissolved salts. In figure 2.3, the properties of brine with a salinity of 15 wt% NaCl are plotted. Brine density and viscosity are obtained from the correlations provided by Batzle and Wang [36]. For the determination of the enthalpy the correlation from Michaelidis [37] has been adopted. The enthalpy of brine is a combination of the enthalpy of pure water, enthalpy of dissolved salts and its mixing enthalpy. Viscosity and specific enthalpy of brine barely change over pressure.

Despite the numerous salt components that can be present in brine in the subsurface, in this research only presence of NaCl is considered. Dissolved salt components starts to precipitate from the aqueous brine phase into solids, if the dissolved salt concentration ( $x_{NaCl,Aq}$ ) exceeds the solubility limit ( $x_{NaCl,Aq,max}$ ). This solubility limit is mainly affected by the temperature of brine and is calculated using [38]

$$x_{NaCl,Aq,max} = 0.26218 + 7.2 \times 10^{-5} T + 1.06 \times 10^{-6} T^2, \quad (2.1)$$

where  $T$  is the temperature in °C. The solubility limit increases with increasing temperature.

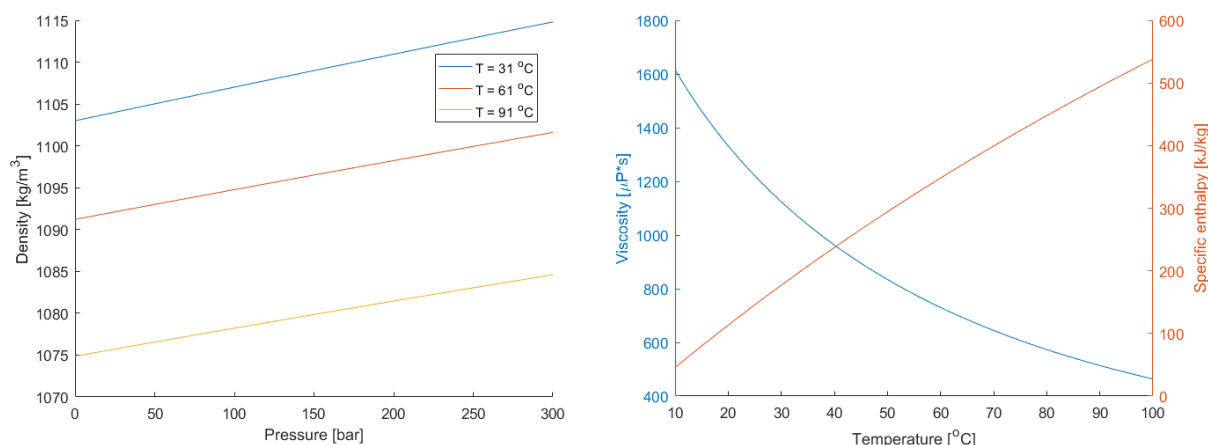


Figure 2.3: (left) Density of brine with 15 wt% NaCl plotted over pressure for different temperatures and (right) viscosity and specific enthalpy of brine plotted over temperature.

### 2.1.5. Mutual solubility

The CO<sub>2</sub> and CH<sub>4</sub> components in the non-aqueous phase can dissolve in the brine phase while simultaneously H<sub>2</sub>O components of the brine phase can dissolve or evaporate into the non-aqueous phase, causing mutual exchange of components. This mutual exchange of components is associated with thermal effects, which is further addressed in paragraph 2.2. Whether water evaporates or dissolves from the aqueous into the non-aqueous phase depends on the phase condition of the latter. However, for convenience, dissolution of water in the non-aqueous phase will also be referred to as vaporization throughout this research, regardless of the phase condition of the non-aqueous phase. Various solubility models have been developed to calculate the mutual exchange of components for a given temperature, pressure and salinity. Comprehensive models, applicable in the considered pressure and temperature range, for the mutual solubility of CO<sub>2</sub>-brine systems and CH<sub>4</sub>-brine systems have been developed by Spycher and Pruess [39] and Duan and Mao [40] respectively. The mutual exchange of components are shown in Appendix A figure A.1 and A.2.

Overall, the solubility of the  $\text{CO}_2$  and  $\text{CH}_4$  increases with increasing pressure and decreasing salinity of the aqueous phase. Dissolution of  $\text{CH}_4$  in brine is approximately one order of magnitude smaller than  $\text{CO}_2$ . The amount of water components that dissolves or evaporates, into the non-aqueous phase increases with increasing temperature. In addition, the dissolution curves of water in  $\text{CO}_2$  reach a minimum in the range of 50 to 110 bar depending on the temperature. The mentioned figures in the appendix illustrate the mutual solubility of pure  $\text{CO}_2$ -brine and  $\text{CH}_4$ -brine binary systems. However, presence of a secondary non-aqueous component in a full  $\text{CO}_2$ - $\text{CH}_4$ -brine mixture system, actually slightly enhances the solubility of the other component in the brine phase [25, 41].

## 2.2. Thermal processes and parameters

### 2.2.1. $\text{CO}_2$ and $\text{CH}_4$ dissolution

Dissolution of  $\text{CO}_2$  and  $\text{CH}_4$  in the aqueous phase is a non-isothermal process. Below a temperature of roughly  $160^\circ\text{C}$ , this process is exothermic. The amount of heat released during dissolution of these components ( $\Delta H_{sol}$ ) is dependent on the temperature, pressure and salinity, as shown for  $\text{CO}_2$  in figure 2.4 (left). It decreases with increasing salinity and pressure for a constant temperature. The heat of dissolution of  $\text{CH}_4$  is approximately in the same order of magnitude as for  $\text{CO}_2$  [40].

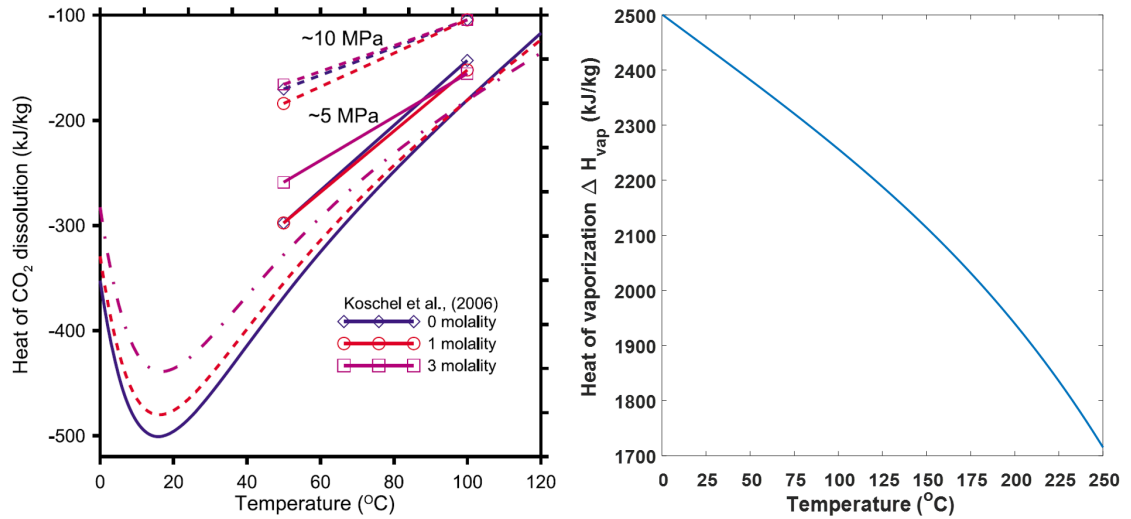


Figure 2.4: (left) Heat of dissolution ( $\Delta H_{sol}$ ) obtained from experimental data as a function of temperature for various brine salinities and pressures [23]; (right) Heat of water vaporization ( $\Delta H_{vap}$ ) for pure water according to IAPWS-95.

### 2.2.2. Water vaporization

Similar to  $\text{CO}_2$  dissolution in the aqueous phase, also the vaporization of water in the non-aqueous phase is a non-isothermal process. However, contrary to  $\text{CO}_2$  and  $\text{CH}_4$  dissolution, the vaporization of water is endothermic and absorbs heat from the system. In figure 2.4 (right), the heat of vaporization for pure water is shown. It can be observed that the heat absorbed during vaporization of water is significantly larger than the heat released during  $\text{CO}_2$  dissolution for equal mass transfers.

### 2.2.3. Phase enthalpy changes by vaporization and dissolution

The dissolution and vaporization effects, change the thermal equilibrium of the system. To find the exact contribution of each effect, the heat of dissolution should be combined with the amount of non-aqueous components dissolved in the aqueous phase and the heat of vaporization with the amount of  $\text{H}_2\text{O}$  components vaporized into the non-aqueous phase. These thermal effects are captured in the system by a change of enthalpy of the present phases, similar to the procedures used in the numerical TOUGH2 simulator, which can be written for the aqueous phase as

$$H_{Aq} = x_{\text{CO}_2, Aq}(H_{\text{CO}_2} + \Delta H_{sol, \text{CO}_2}) + x_{\text{CH}_4, Aq}(H_{\text{CH}_4} + \Delta H_{sol, \text{CH}_4}) + (1 - x_{\text{CO}_2, Aq} - x_{\text{CH}_4, Aq})H_b, \quad (2.2)$$

and for the non-aqueous phase, where no distinction is made on its phase condition as

$$H_{NA} = x_{CO_2,NA}H_{CO_2} + x_{CH_4,NA}H_{CH_4} + x_{H_2O,NA}(H_{H_2O} + \Delta H_{vap,H_2O}). \quad (2.3)$$

Here,  $H$  and  $x$  describe the enthalpy and component mass fraction in a certain phase. Besides,  $H_b$  represents the enthalpy of brine, comprising the enthalpy of  $H_2O$  and dissolved NaCl components. In the equations above, the enthalpy of mixing ( $\Delta H_{mix}$ ), a term which is introduced for non-ideal mixtures is neglected. This is a reasonable assumption due to presence of additional heat terms (i.e. vaporization and dissolution) considerably larger than the enthalpy of mixing [42].

#### 2.2.4. Joule-Thomson effect

Another important thermal process is the JT effect. The JT effect is defined as the change of the temperature of a substance during compression or expansion. Changes in the enthalpy of a substance caused by JT effect is given by [23]

$$dH = C_p dT - \mu_{jt} C_p dp, \quad (2.4)$$

where  $C_p$  is the heat capacity,  $\mu_{jt}$  is the JT coefficient and  $p$  is the pressure. The JT effect will be extensively discussed in paragraph 3.1.1.

#### 2.2.5. Effective heat capacity and thermal conductivity

The aforementioned processes, together with  $CO_2$  injection at considerably lower temperatures with respect to the initial reservoir temperature, perturb the initial equilibrium temperature of the reservoir. The absolute change in temperature of the system, in response to the induced changes in heat by these processes within the system, depends on predominantly the individual heat capacities of the formation, aqueous phase and non-aqueous phase. Heat capacity of a substance specifies the heat required to change its temperature and can be related to enthalpy change by

$$C_p = \left( \frac{\partial H}{\partial T} \right)_p. \quad (2.5)$$

For the determination of temperature changes in the entire reservoir as a result of the thermal effects, an effective value for the heat capacity can be defined [23], i.e.,

$$C_{p,eff} = \phi(C_{p,NA}S_{NA} + C_{p,Aq}(1 - S_{NA})) + (1 - \phi)C_{p,r}, \quad (2.6)$$

where  $\phi$  is the rock porosity,  $S$  denotes the saturation and the subscript  $r$  indicates the rock. The heat capacity of the non-aqueous phase is highly variable and affected by the local pressure, temperature and composition. Typical values for the heat capacity of sandstone and water, in the temperature and pressure range for depleted gas reservoirs, are 0.9 to 1 and 4.1 to 4.2 kJ/kg/ $^{\circ}C$  respectively. Due to the density differences between the fluid and formation, especially at depleted conditions, usage of an effective volumetric heat capacity is more appropriate, i.e.,

$$C_{eff} = \phi(C_{p,NA}\rho_{NA}S_{NA} + C_{p,Aq}\rho_{Aq}(1 - S_{NA})) + (1 - \phi)C_{p,r}\rho_r, \quad (2.7)$$

where  $\rho$  represents the density. Similar to the effective heat capacity also a effective thermal conductivity can be derived. This is a measure for the ease of a substance to conduct heat. It indicates the relation between the heat flux and induced temperature gradient and is used to determine the average heat transport in the subsurface [23]. The average thermal conductivity, for a formation containing a non-aqueous phase and brine phase, is written by means of a geometric mean [23] as

$$\lambda_{eff} = \lambda_{NA}^{\phi S_{NA}} \lambda_{Aq}^{\phi(1-S_{NA})} \lambda_r^{1-\phi}, \quad (2.8)$$

where  $\lambda$  denotes the thermal conductivity. The thermal conductivity of pure  $CO_2$ ,  $CH_4$ , water and rock are in the range of 0.02 to 0.10, 0.59 to 0.68, 0.03 to 0.05 and 2.2 to 3.5 W/m/ $^{\circ}C$ , respectively [35]. Since the porosity is generally far below 30%, the contribution of the rock formation plays a dominant role in the effective heat capacity and thermal conductivity of the system.

### 2.3. Non-isothermal compositional multi-phase flow

Injection of CO<sub>2</sub> into depleted gas reservoirs induces transport of mass and energy [23]. In this paragraph the non-isothermal compositional multi-phase flow equations are addressed together with a thermodynamic model to describe the component partitioning along the phases.

#### 2.3.1. Mass conservation equation

A mass conservation equation can be derived for the 4 components ( $N_c = 4$ ) (i.e. CO<sub>2</sub>, CH<sub>4</sub>, H<sub>2</sub>O, NaCl) in the considered depleted gas reservoir system, partitioned along the 3 non-solid phases ( $N_p = 3$ ) (i.e. NA<sub>L</sub>, NA<sub>V</sub> and Aq) and can be written as

$$\frac{\partial}{\partial t} \left( \sum_{\alpha=1}^{N_p} \phi \rho_{\alpha} S_{\alpha} x_{i,\alpha} \right) + \nabla \cdot \left( \sum_{\alpha=1}^{N_p} \rho_{\alpha} \vec{u}_{\alpha} x_{i,\alpha} \right) = \sum_{\alpha=1}^{N_p} q_{i,\alpha}, \quad \forall i \in \{1, \dots, N_c\}, \quad (2.9)$$

where  $\rho_{\alpha}$ ,  $S_{\alpha}$ ,  $u_{\alpha}$  are the density, saturation and velocity of phase  $\alpha$ . Besides,  $x_{i,\alpha}$  is mole fraction of component  $i$  in phase  $\alpha$  and  $q_{i,\alpha}$  is the sink or source term as mass rate. It should be noted that the NaCl components are only present in the aqueous phase in the provided conservation equation. At the time scale and injection rates considered in this research, the migration of the reservoir fluids is predominately dominated by advection as a result of the pressure gradient induced by injection and gravity effects due to significant density variations. Diffusion is therefore negligible with respect to the aforementioned forces and not included in the equation above.

The Darcy's multi-phase flow equation is adopted to describe fluid velocities and is defined as

$$\vec{u}_{\alpha} = - \frac{k_{r,\alpha} \mathbf{K}}{\mu_{\alpha}} (\nabla p_{\alpha} - \rho_{\alpha} g \nabla h), \quad \alpha \in \{Aq, NA_L, NA_V\}, \quad (2.10)$$

where  $\mathbf{K}$  is the rock permeability tensor which is assumed to be isotropic,  $g$  is the gravitational acceleration,  $h$  is the depth and  $k_{r,\alpha}$ ,  $\mu_{\alpha}$ ,  $p_{\alpha}$  are the relative permeability, viscosity and pressure of a phase  $\alpha$  respectively.

In the reservoir salt can precipitate from the aqueous phase, as the salt concentration in this phase exceeds the solubility limit. Assuming instantaneous precipitation of salt as the concentration of dissolved salt in the aqueous phase exceeds the solubility limit, the source term, i.e. the mass of the precipitating salt over time, can be written as [43]

$$q_{NaCl,Aq} = \begin{cases} r_c \phi \rho_{Aq} S_{Aq} (x_{NaCl,Aq} - x_{NaCl,Aq,max}), & \text{if } x_{NaCl,Aq} > x_{NaCl,Aq,max} \\ 0, & \text{otherwise} \end{cases} \quad (2.11)$$

where  $r_c$  is the precipitation rate constant in 1/s. Precipitation of salt from the aqueous phase adds additional mass to the solid salt phase, implying a positive source term in the equation above. On the other hand, dissolution of precipitated salt leads to a negative source term but is not considered here. Eventually, a mass conservation equation can be defined for the immobile salt in precipitated solid form in the reservoir, i.e.,

$$\frac{\partial}{\partial t} (\phi_{NaCl,s} \rho_s) + q_{NaCl,Aq} = 0. \quad (2.12)$$

Where  $\phi_{NaCl,s}$  is the solidity representing the volume of pore space occupied with precipitated salt [43] and  $\rho_s$  is the density of the solid precipitate. The provided equations should be simultaneously treated to ensure the conservation mass in both solid and non-solid phases. As a consequence of the exchange of mass between phases, mass is not conserved for each phase but for each component [44].

#### Porosity and permeability reduction due to salt precipitation

Precipitated salt reduces the pore space, because the salt crystals occupy part of the pore volume. The reduction of the formation porosity as a consequence of salt precipitation can be defined as [45]

$$\phi = \phi_0 - \phi_{NaCl,s} = \phi_0 (1 - S_s), \quad (2.13)$$

where  $\phi_0$  refers to the initial porosity without precipitated salt. Various models are used in literature to relate the change in porosity to a change in permeability. Widely adopted is the 'tubes-in-series' model by Verma and Pruess (1988), which captures the natural converging-diverging nature of natural pore channels

consisting of alternating segments of capillary tubes with larger and smaller radii [28] (see figure 2.5a). The Verma-Pruess model reads as

$$\frac{K}{K_0} = \theta^2 \frac{1 - \Gamma + \frac{\Gamma}{\omega^2}}{1 - \Gamma + \Gamma \left[ \frac{\theta}{\theta + \omega - 1} \right]^2}, \quad (2.14)$$

with

$$\theta = \frac{1 - S_s - \phi_r}{1 - \phi_r}, \quad (2.15)$$

and

$$\omega = 1 + \frac{1/\Gamma}{1/\phi_r - 1}, \quad (2.16)$$

where  $K_0$  is the original rock permeability,  $S_s$  is the solid salt saturation,  $\phi_r$  is the fraction of the original porosity (or critical porosity) for which the permeability reduces to zero and  $\Gamma$  is the fractional length of the pore bodies (see fig 2.5) [28]. The latter two parameters can be tuned according to experimental results. Moreover, another extensively used model for numerical calculation of permeability reduction due to salt precipitation is the Carman-Kozeny function [27], given by

$$\frac{K}{K_0} = \left( \frac{\phi}{\phi_0} \right)^{C_{ck}} \left( \frac{1 - \phi_0}{1 - \phi} \right)^2, \quad (2.17)$$

where  $C_{ck}$  is a fitting parameter which has a default value of 3 by definition. This equation can also be expressed in terms of the solid saturation by substitution of (2.13) in (2.18), which, for a default value of the fitting parameter [45], results in

$$\frac{K}{K_0} = \frac{(1 - S_s)^3}{\left( 1 + \frac{\phi_0}{1 - \phi_0} S_s \right)^2}. \quad (2.18)$$

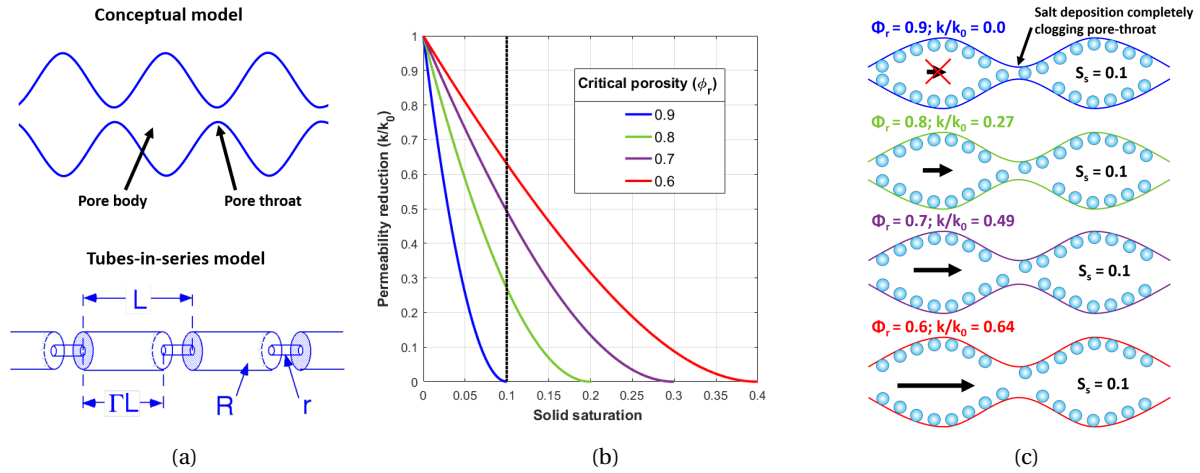


Figure 2.5: (a) the conceptual model of pore-body and pore-throat in rocks and the 'tubes-in-series' configuration indicating the fractional pore length ( $\Gamma$ ) adopted in the Verma-Pruess permeability reduction model [28]; (b) Permeability reduction as function of the solid saturation for various  $\phi_r$  values; (c) Schematic representation of a pore-body to pore-throat combination with uniformly distributed salt precipitation at a solid salt saturation of 0.1 (indicated in (b) by the dotted black line) for each  $\phi_r$  value (at a fixed  $\Gamma$  of 0.8), modified after [46].

### 2.3.2. Energy conservation equation

To model non-isothermal flow for  $\text{CO}_2$  injection in depleted gas reservoirs an energy conservation equation should be incorporated. The energy conservation equation captures influence of the thermal effects on the temperature of the system. Potential existence of a solid salt phase is not accounted for in this section. Although the formation temperature and fluid temperature can deviate, especially in reservoirs with significant fluid velocities and low thermal diffusivity of the formation [47], local thermal equilibrium is assumed in this research. Following [44], the energy conservation equation is defined as

$$\frac{\partial}{\partial t}(\rho_t U) + \nabla \cdot \vec{E} + \nabla \cdot \sum_{\alpha=1}^{N_p} (p_\alpha \vec{u}_\alpha) = \sum_{\alpha=1}^{N_p} H_\alpha q_\alpha - q_L, \quad (2.19)$$

where  $\rho_t U$  denotes the total internal energy,  $E$  denotes the energy flux, the last term on the left hand side of the equation indicates the rate of work done by the pressure field and  $q_L$  gives the heat exchange with adjacent formations. Radiation and influences of kinetic energy are neglected in the equation above. The total internal energy can be written as

$$\rho_t U = \phi \sum_{\alpha=1}^{N_p} \rho_\alpha S_\alpha U_\alpha + (1 - \phi) \rho_r C_{p,r} T. \quad (2.20)$$

Here  $C_{p,r}$  represents the specific heat capacity of the rock and  $U_\alpha$  the specific internal energy of a phase  $\alpha$ . The energy flux considered consists of convective contributions from flow and conductive heat flux (i.e. neglecting radiation and other contributions) and reads respectively

$$\vec{E} = \sum_{\alpha=1}^{N_p} \rho_\alpha \vec{u}_\alpha U_\alpha - \lambda_T \nabla T, \quad (2.21)$$

in which the phase enthalpy is defined as

$$H_\alpha = U_\alpha + \frac{p_\alpha}{\rho_\alpha}, \quad (2.22)$$

where  $\lambda_T$  represents the total thermal conductivity. Substitution of 2.20 and 2.21 into 2.19 and combination of the convective flow contribution of the energy flux and the work done against the pressure field, leads to the final energy balance, i.e.,

$$\frac{\partial}{\partial t} \left( \phi \sum_{\alpha=1}^{N_p} \rho_\alpha S_\alpha U_\alpha + (1 - \phi) \rho_s C_s T \right) + \nabla \cdot \sum_{\alpha=1}^{N_p} \rho_\alpha \vec{u}_\alpha H_\alpha - \nabla \cdot (\lambda_T \nabla T) = \sum_{\alpha=1}^{N_p} H_\alpha q_\alpha - q_L. \quad (2.23)$$

The mass and energy conservation equations (2.9, 2.12 and 2.23) are strongly coupled non-linear equations. Coupling between the mass and energy balance equation is formed through the convective heat transfer induced by migration of fluids, as a consequence of the existing pressure differential within the reservoir and the effect of local temperature changes on the properties of the reservoir fluids. PVT properties of the substances highly dependent on both the pressure and temperature. Hence, an implicit solution strategy, simultaneously solving the mass and energy equations is most applicable for these non-isothermal multi-component multi-phase simulations.

### Heat exchange with reservoir confining formations

CO<sub>2</sub> injection perturbs the temperature distribution in the reservoir and subsequently induces heat exchange between the reservoir and the adjacent formations. To calculate this particular heat exchange, the temperature profile in the confining formations is required. An efficient method to approximate this profile is the semi-analytical solution developed by Vinsome and Westerveld [48]. In this solution a temperature profile in the confining formations is defined, based on two fitting parameters  $p$  and  $q$ , which are determined from physical constraints of the continuity of heat flux across the boundary between the confining beds and reservoir and energy conservation of the layers during the flow simulation [28], and can be written as [48]

$$T(z, t) - T_i = (T_f - T_i + pz + qz^2) e^{-\frac{z}{d}}. \quad (2.24)$$

Here  $T_i$  indicates the initial temperature of the adjacent formation,  $T_f$  gives the time-dependent temperature at the boundary of the adjacent formation,  $z$  is the penetration depth and  $d$  is the diffusion length [28]. This diffusion length is defined as

$$d = \sqrt{\frac{\kappa t}{2}}. \quad (2.25)$$

In the equation above,  $\kappa$  represents the rock thermal diffusivity ( $\kappa = \lambda_r / \rho_r C_{p,r}$ ). Although significant temperature differentials can arise across the boundary between reservoir and confining formation, merely continuous temperature changes will be observed in the confining formations due to the strong heat conduction within these formations. The unaffected parts of the confining formations significantly dampen the temperature variation [28]. After the temperature profile is approximated, the heat exchange source/sink term can be derived. For the final derivation of this term refer to Vinsome and Westerveld [48].

### 2.3.3. Thermodynamic equilibrium and component phase partitioning

In systems consisting of multiple components and phases at local thermodynamic equilibrium, the chemical potentials of particular components partitioned among the phases are in equilibrium. The chemical potential of a component  $i$  in phase  $\alpha$  is defined as

$$\mu_{i,\alpha} = \mu_{i,\alpha}^o + RT \ln(f_{i,\alpha}), \quad (2.26)$$

where  $\mu_{i,\alpha}^o$  and  $f_{i,\alpha}$  are the chemical potential and fugacity at reference temperature of a component  $i$  in phase  $\alpha$  and  $R$  is the gas constant. Thermodynamic equilibrium ensures that the chemical potentials of each component in all phases is equal, i.e.,

$$\mu_{i,\alpha}(p, T) - \mu_{i,\beta}(p, T) = 0, \quad \forall \alpha \neq \beta = 1, \dots, N_p; \quad i = 1, \dots, N_c, \quad (2.27)$$

Specific thermodynamic models have been developed to explicitly model the phase partitioning of the various components in CO<sub>2</sub>-H<sub>2</sub>O-NaCl mixtures. However, these models are only valid to CO<sub>2</sub>-brine systems and cannot be used in presence of additional components as CH<sub>4</sub>. Accordingly, modeling of depleted gas field storage requires extended thermodynamic equilibrium models which allow for multi-component CO<sub>2</sub> mixtures with additional components as CH<sub>4</sub>, SO<sub>2</sub>, N<sub>2</sub> in conjunction with an aqueous phase. Ziabakhsh-Ganji [25] and Battistelli and Marcolini [29] developed these extended thermodynamic equilibrium models which account for dissolution of non-aqueous components in the aqueous phase and vaporization of aqueous component in the non-aqueous phase. Following the clearly described thermodynamic model and related derivations provided by Ziabakhsh-Ganji [25], for a component  $i$  (excluding H<sub>2</sub>O), partitioned between the non-aqueous phase i.e. the multi-component mixture in gaseous, supercritical or condensed conditions and the aqueous phase, holds that

$$\frac{\mu_{i,NA}^o - \mu_{i,Aq}^o}{RT} = \ln\left(\frac{f_{i,Aq}}{f_{i,NA}}\right), \quad (2.28)$$

which follows from combining equation 2.26 and 2.27. Determination of the phase partitioning of non-aqueous components (e.g. CO<sub>2</sub>, CH<sub>4</sub> and N<sub>2</sub>) differs from the aqueous component (i.e. H<sub>2</sub>O) due to limitations in the applicability of certain physical laws with respect to the aqueous component and are therefore discussed separately.

#### Non-aqueous components

Since the solubility of the gaseous components is relatively low, the fugacity of a non-aqueous component in the aqueous phase can be replaced by the activity  $a$ , given by

$$f_{i,Aq} = a = N_w \gamma_i x_{i,Aq}, \quad (2.29)$$

where  $N_w$  the number of moles of per kilogram water and  $\gamma_i$  denotes the activity coefficient. Influence of the salinity is accounted for in the activity coefficient; salt components (e.g. NaCl) are not explicitly modeled. The fugacity in the non-aqueous phase can be written in terms of a fugacity coefficient, i.e.,

$$f_{i,NA} = p \phi_i x_{i,NA}, \quad (2.30)$$

where  $\phi_i$  indicates the fugacity coefficient of component  $i$ . Substitution of equation 2.28 and 2.29 into equation 2.30 and rewriting leads to an expression for the equilibrium constant  $K_i^o$  which is given by

$$\frac{\mu_{i,NA}^o - \mu_{i,Aq}^o}{RT} = \ln\left(\frac{N_w \gamma_i x_{i,Aq}}{p \phi_i x_{i,NA}}\right) = \ln(K_i^o). \quad (2.31)$$

The equilibrium constant in equation 2.31 can be written in terms of Henry's coefficients  $k_{H,i}$ , i.e.,

$$K_i^o = \frac{N_w}{k_{H,i}}. \quad (2.32)$$

Solubility of the components in the aqueous phase is affected by the pressure, temperature and salinity of the aqueous phase and should be consequently accounted for in the Henry coefficient of this component. As discussed in paragraph 2.1.5, the solubility of a component in the aqueous phase increases with increasing pressures, but decreases for increasing temperatures and salinities.

Combining and rewriting equation 2.31 and 2.32 finally yields the rewritten equilibrium of a non-aqueous component (e.g. CO<sub>2</sub> and CH<sub>4</sub>) between the non-aqueous and aqueous phase, i.e.,

$$(p\phi_i x_{i,NA}) = (k_{H,i}\gamma_i x_{i,Aq}). \quad (2.33)$$

Interaction between non-aqueous components dissolved in the aqueous phase is neglected. To obtain the required fugacity coefficient in the non-aqueous phase for both the non-aqueous and aqueous components, a (cubic) equation of state (EOS) (e.g. Peng-Robinson (PR) or Soave-Redlich-Kwong (SRK)) can be utilized. Generally the PR EOS is preferred over the SRK EOS because it allows for better accuracy across the vapor-liquid boundary [25]. In the PR EOS, the fugacity coefficient is calculated based on compressibility of the non-aqueous phase, characteristic critical properties of the components and binary interaction coefficients in case of mixtures, using the following equation

$$\ln(\phi_i) = \frac{B_i}{B}(Z-1) - \ln(Z-B) + \frac{A}{2.828B} \left[ \frac{B_i}{B} - \frac{2\sum_j x_{i,NA} a_{ij}}{a} \right] \ln \left[ \frac{Z+2.414B}{Z-0.414B} \right], \quad (2.34)$$

The complete procedure for the determination of the fugacity coefficient and explanation of the corresponding parameters in the PR EOS is given in Appendix A.3. Moreover,  $\gamma$  in equation 2.33 can be calculated from an equation provided by Duan and Sun (2003), which reads

$$\ln(\gamma_i) = \sum_C 2m_C \lambda_{i-C} + \sum_A 2m_A \lambda_{i-A} + \sum_C \sum_A m_A m_C \zeta_{i-A-C}, \quad (2.35)$$

where  $m_C$  is the anions molality,  $m_A$  is the cation molality,  $\lambda_{i-A}$  is the second order interaction parameter which assumed to be equal to zero and  $\lambda_{i-C}$  is the third order interaction parameter.

### Aqueous component

For the aqueous H<sub>2</sub>O components in the system a similar procedure is used to define the partitioning between the non-aqueous and aqueous phase. In contrast to the non-aqueous components, to calculate the fugacity of the H<sub>2</sub>O component in the aqueous phase Henry's law is not applicable. Hence, alternative constitutive relations are utilized in the model developed by ZiabakhshGanji [25] which are based on the Spycher et al. (2003) equilibrium constant  $K$ , i.e.,

$$K_{H_2O} = \frac{f_{H_2O,NA}}{a_{H_2O,Aq}}. \quad (2.36)$$

Implementation of 2.29 for the fugacity of water in the non-aqueous phase in the equation above gives

$$f_{H_2O,NA} = p\phi_{H_2O} x_{H_2O,NA} = K_{H_2O} a_{H_2O,Aq}. \quad (2.37)$$

As a consequence of the low solubility of gaseous components in the aqueous phase in the temperature range considered (5 to 110°C) the activity  $a$  can be approximated by the amount of aqueous components present in the aqueous phase (i.e.  $x_{H_2O,Aq}$ ). The equilibrium constant for the water component, strongly depending on pressure and temperature, is defined as

$$K_{H_2O}(p, T) = K_{H_2O}^0(p_0, T) \exp \left[ \frac{(p-p_0)V_{H_2O}}{RT} \right], \quad (2.38)$$

where  $V_{H_2O}$  denotes the average partial molar volume of water in the aqueous phase within the pressure interval  $(p-p_0)$  and  $p_0$  denotes the reference pressure. Combining equations 2.37 and 2.38 gives

$$K_{H_2O}^0(p_0, T) \exp \left[ \frac{(p-p_0)V_{H_2O}}{RT} \right] x_{H_2O,Aq} = p\phi_{H_2O} x_{H_2O,NA}, \quad (2.39)$$

where  $K_{H_2O}^0$  can be obtained from an straightforward relation provided by Spycher et al. (2003). The described thermodynamic equilibrium model by ZiabakhshGanji [25] proved to be accurate and reliable up to a pressure of 600 bar, temperature of 110 °C and a salinity of 6 molality. These conditions are within the characteristic range of depleted gas fields considered for CO<sub>2</sub> storage.

### Non-aqueous and aqueous components phase partitioning

In mixture systems a flash calculation is required to calculate the partitioning of the components among the non-aqueous and aqueous phase. The component partitioning at a certain temperature, temperature and salinity can be obtained from the Rachford-Rice equation, i.e.,

$$\sum_{i=1}^{N_c} \frac{z_i(K_i - 1)}{1 + \beta(K_i - 1)} = 0, \quad (2.40)$$

where  $z_i$  denotes the mole fraction of the individual components in the entire system. Equation 2.40 is solved for  $\beta$  representing the total mole fraction of the non-aqueous phase. The equilibrium constant  $K_i$  for both non-aqueous and aqueous components is given by

$$K_i = \frac{x_{i,NA}}{x_{i,Aq}}. \quad (2.41)$$

Substitution of the right hand side of the equation above into 2.32 for the non-aqueous components and 2.38 for the aqueous component, provides the final  $K_i$  values. Eventually, after  $\beta$  and  $K_i$  are calculated, the mole fractions of the individual components in the non-aqueous and aqueous phase can be determined for a given  $z_i$  by

$$x_{i,Aq} = \frac{z_i}{1 + \beta(K_i - 1)}, \quad (2.42)$$

and

$$x_{i,NA} = \frac{K_i z_i}{1 + \beta(K_i - 1)}. \quad (2.43)$$

### 2.3.4. Injectivity

The near wellbore effects influence the injectivity of CO<sub>2</sub> in the reservoir. Injectivity of CO<sub>2</sub> in a depleted reservoir in a reservoir can be defined as the pressure fall off required to inject a certain amount of CO<sub>2</sub> in the reservoir and can be written as [49]

$$\Pi = \frac{q_{NA}}{p_{bhp} - p_{avg}}, \quad (2.44)$$

where  $\Pi$  denotes the injectivity index,  $q_{NA}$  is the non-aqueous phase mass injection rate at reservoir conditions which is assumed to be consisting of pure CO<sub>2</sub> components (i.e.  $q_{NA} = q_{CO_2,NA}$ ),  $p_{bhp}$  is the injection well bottom hole pressure and  $p_{avg}$  is the pattern average pressure. The injection rate  $q_{NA}$  is given by [49] as

$$q_{NA} = WI \rho_{NA} \frac{k_{r,NA}}{\mu_{NA}} (p_{bhp} - p_{we}), \quad (2.45)$$

where  $p_{we}$  is the pressure of grid block in which the well is located. The relative permeability and the viscosity of the phase are evaluated at the well block in the equation above. The well index, describing the interaction between the reservoir and wellbore [50], is defined using Peaceman's model which reads as [49]

$$WI = \frac{2\pi K_{eff} h_{gb}}{\ln(r_{eff}/r_w) + s}, \quad (2.46)$$

where  $K_{eff}$  is an effective value for the permeability (in mD) given by  $\sqrt{K_y K_x}$ , comprising the permeability in  $x$  and  $y$  direction [50] which are assumed to be equal in this research,  $h_{gb}$  grid block height,  $r_{eff}$  effective radius of the well grid block and  $s$  is the dimensionless skin factor. In this research, the detrimental effect of salt precipitation on the injectivity due to precipitation of salt is captured by a reduction of the rock permeability as discussed in paragraph 2.3.1.

### 2.3.5. Relative permeability curves

Relative permeability is defined as the ability of flow of a certain phase in presence of other phases. Generally, constitutive relations as the Corey (1954), Brooks-Corey (1964) and Van Genuchten-Mualem (1976) can be adopted to obtain the relative permeability curves fitted to experimental data for two phase problems. Three phase problems, where CO<sub>2</sub> in liquid and gaseous phase coexists along with the aqueous phase, require extended relative permeability models as provided by Stone (1970) and Parker (1987). However, in this thesis, a modified Corey formulation is utilized instead of the traditional relations for three phase relative permeability, which ensures better consistency for phase changes across and above the critical point of CO<sub>2</sub> in numerical models, i.e.,

$$k_{r,\alpha} = \left( \frac{S_\alpha - S_{\alpha,r}}{1 - S_{\alpha,r}} \right)^n, \quad (2.47)$$

where  $S_{\alpha,r}$  is the residual saturation of a phase  $\alpha$  and  $n$  is the Corey exponent. The modified formulation is characterized by dependency of the relative permeability of a particular phase on solely its own saturation and is not affected by the presence of other phases [20]. The manner in which the modified Corey formulation (2.47) is defined, also ensures flow of the CO<sub>2</sub>-rich phase if the aqueous phase saturation drops below the irreducible water saturation due to vaporization.

### 2.3.6. Capillary pressure

The pressure differential along the interface between two immiscible phases in a confined volume (e.g. rock pore) is defined as the capillary pressure. Capillary pressure is a consequence of cohesive and adhesive forces acting on the phases in the system. In a three phase water wet system, the capillary pressures is given by

$$p_{c,V-L} = p_L - p_V, \quad (2.48)$$

$$p_{c,V-Aq} = p_{Aq} - p_V, \quad (2.49)$$

$$p_{c,L-Aq} = p_{Aq} - p_V, \quad (2.50)$$

where  $p_{c,V-L}$ ,  $p_{c,V-Aq}$  and  $p_{c,L-Aq}$  are the capillary pressures between the vapor-liquid, vapor-aqueous and liquid-aqueous phases respectively. Various analytical methods have been developed to describe capillary pressure as a function the non-wetting phase. Here, the Van Genuchten (1980) model utilized, i.e.,

$$p_c = -p_0 \left( [S_{eff}]^{-1/\lambda} - 1 \right)^{1-\lambda}, \quad (2.51)$$

where  $\lambda$  and  $p_0$  are fitting parameters indicating the curvature of the capillary pressure curve and the strength coefficient respectively. The effective saturation ( $S_{eff}$ ) is given by

$$S_{eff} = \frac{S_w - S_{w,r}}{1 - S_{nw,r} - S_{w,r}}, \quad (2.52)$$

where  $S_w$  is the saturation of the wetting phase and  $S_{w,r}$  and  $S_{nw,r}$  are the residual saturation of the wetting and non-wetting phase respectively. The Van Genuchten model is only applicable to two phase problems, while in three phase problems capillary pressure arises between all phases. Thus, the assumption is made in this research that capillary pressure between the non-aqueous phase and the aqueous phase is independent of the non-aqueous phase condition. In addition, capillary pressure between different phase conditions of the non-aqueous phase (liquid-vapor) is neglected.

The shape of the capillary pressure function is directly correlated to the pore size distribution of the formation. A uniform pore size distribution leads to very steep gradients in the capillary pressure curve close to the irreducible water saturation and a low gradient at high saturation values [51]. Hence, for uniformly distributed pores only a minor pressure is required to displace water from the pores at high water saturations. On the other hand, in formations with highly uneven distributed pores, a more gradual increase in capillary pressure is observed as the water saturation decreases. Differences in capillary pressure behavior imbibition and drainage (i.e. capillary hysteresis) are not taken into account.

### 2.3.7. Additional constrains

Additional constrains are required to construct a well posed system along with the previously discussed balance equations. These are:

- Occupation of the entire pore space by the phases, i.e.,

$$S_s + S_{NA_L} + S_{NA_V} + S_{Aq} = 1 \quad (2.53)$$

- The component mass fractions in each particular phase sum up to unity, according to phase partitioning of components discussed in paragraph 2.2.3, which can be written for each phase as

Solid phase:

$$x_{NaCl,s} = 1 \quad (2.54)$$

Non-aqueous liquid phase:

$$x_{CO_2,NA_L} + x_{CH_4,NA_L} + x_{H_2O,NA_L} = 1 \quad (2.55)$$

Non-aqueous vapor phase:

$$x_{CO_2,NA_V} + x_{CH_4,NA_V} + x_{H_2O,NA_V} = 1 \quad (2.56)$$

Aqueous phase:

$$x_{CO_2,Aq} + x_{CH_4,Aq} + x_{H_2O,Aq} + x_{NaCl,Aq} = 1 \quad (2.57)$$

# 3

## Near wellbore effects

Injection of CO<sub>2</sub> in a reservoir will cause a disturbance in global and local equilibria and the associated physical state of the reservoir. Reservoir characteristics and conditions (i.e. temperature, pressure and pore fluid properties) are affected by the introduction of CO<sub>2</sub>. This results in perturbations in heat and fluid flow (i.e. hydrology), stress and strain states of the reservoir (i.e. geomechanics) and chemical equilibria and reactions (i.e. geochemistry). Changes in these strongly interconnected elements ultimately influence rock properties as permeability and porosity, which in turn again affects the heat and fluid transport in the reservoir (see figure 3.1). Hence, a sophisticated concatenation of mutually affecting processes is induced during the injection of CO<sub>2</sub>, increasing the modeling complexity of a injection process.

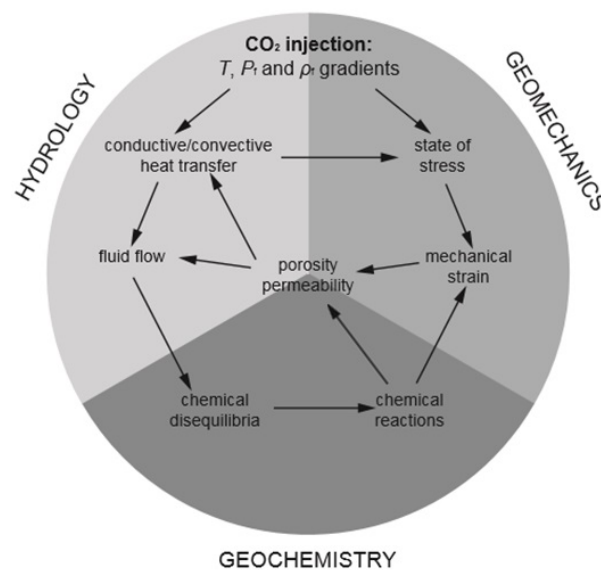


Figure 3.1: Concatenation of processes and parameters affected by the perturbation of the temperature and pressure in the system caused by CO<sub>2</sub> injection, modified after [52].

The aforementioned disturbances of the local equilibrium and state of the reservoir during the injection of CO<sub>2</sub> express themselves in the appearance of physical phenomena in the near wellbore area or so called near wellbore effects. A schematic overview of the main near wellbore effects are depicted in figure 3.2. Minor effects as exothermic CO<sub>2</sub> dissolution or endothermic water vaporization, discussed previously, are not considered in this overview. The near wellbore effects can be loosely divided into thermal, geomechanical and geochemical effects. Due to the complex nature of the near wellbore effects, some effects (e.g. hydrate formation and thermal fracturing) pertain to multiple categories but are classified to a category based on their underlying physical principle. In this research primary focus is given to the thermal near wellbore effects, salt precipitation and hydrate formation.

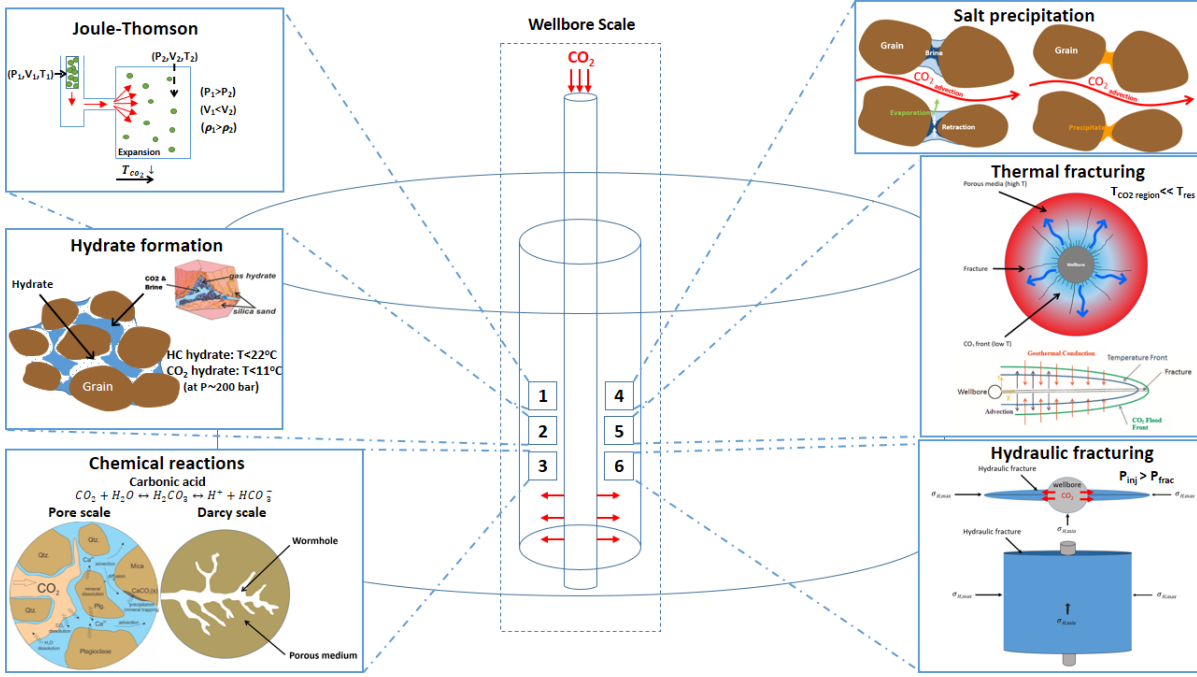


Figure 3.2: Overview of potential effects arising in the near wellbore region as a consequence of CO<sub>2</sub> injection, modified after [53–58].

### 3.1. Thermal effects

#### 3.1.1. Joule-Thomson effect

The JT effect is defined as the change in temperature of a substance caused by adiabatic expansion during a reduction of the substance its pressure [23]. According to the original Joule-Thomson experiment, one will observe a change in temperature and volume of a substance if this substance migrates through a thermally insulated medium from a region at high pressure to a region at low pressure. The amount of work ( $w$ ) provided during this transition from a begin pressure ( $p_1$ ), where substance has a volume ( $V_1$ ), to the final pressure ( $p_2$ ) and volume ( $V_2$ ), is equivalent to the change in internal energy or work done during injection [11], i.e.,

$$w = \Delta U = p_1 V_1 + p_2 V_2. \quad (3.1)$$

The change in internal energy and the change in product of the volume and pressure of the substance represent the change of enthalpy, which is written as

$$\Delta H = \Delta U + \Delta(pV). \quad (3.2)$$

Since thermal insulation is assumed, the enthalpy remains constant ( $\Delta H = H_2 - H_1 = 0$ ) despite the changes in temperature and volume of the substance. This implies that the JT expansion corresponds to an isenthalpic process [23], i.e.,

$$\Delta H = \Delta U + \Delta(pV) = p_1 V_1 + p_2 V_2 + \Delta(pV) = H_2 - H_1 = 0. \quad (3.3)$$

Based on the previous statements, it can be argued that a perturbation of the temperature drop of the substance during adiabatic expansion or compression directly relates to the pressure drop. The ratio between the temperature and pressure drop during adiabatic expansion or compression is defined as the JT coefficient, i.e. [11],

$$\mu_{jt} = \left( \frac{\partial T}{\partial p} \right)_H \approx \frac{\Delta T}{\Delta p}. \quad (3.4)$$

The JT coefficient varies strongly for different substances and highly depends on the initial temperature of the substance and pressures at which the expansion or compression occurs. In addition, the sign of this coefficient indicates if the substance cools down (i.e. positive sign) or heats up (i.e. negative sign) upon expansion. Each substance has a specific JT inversion temperature where the sign of the JT coefficient changes.

In the range of conditions corresponding to gas reservoirs, the JT coefficients of the non-aqueous substances considered (i.e. CO<sub>2</sub> and CH<sub>4</sub>) remain positive and will consequently cool down during expansion [11, 23]. Below the inversion temperature, the expansion of the substance increases the potential energy because the distance between the molecules, exerting and experiencing inter molecular attraction forces, increases. Since no heat exchange with the surrounding takes place and the total energy of the gas remains constant, the kinetic energy consequently decreases causing a temperature reduction [26].

JT coefficients for pure CO<sub>2</sub> are shown in figure 3.3 and vary between 0 to 1.5 °C/bar. At pressures below critical pressure (<73.9 bar) of CO<sub>2</sub>, the JT coefficient increases for decreasing temperatures while above 120 bar the opposite holds. Below critical conditions (i.e. <73.9 bar and <31.1°C respectively) and the vapor pressure, when the CO<sub>2</sub> is in gaseous phase, the highest JT coefficients are measured. This in contrast to the low values (0 to 0.5 °C/bar) in the region corresponding to liquid CO<sub>2</sub>. For conditions ( $p, T$ ) approaching the saturation line, the graph shows strong erratic behavior indicating sudden phase transitions between gaseous and liquid CO<sub>2</sub>. The JT coefficients of supercritical CO<sub>2</sub> are in between the values for gaseous and liquid phase but strongly decrease with increasing pressure. Therefore, the injection and reservoir conditions, defining the phase of the CO<sub>2</sub>, are extremely important for the magnitude of the induced cooling by injection of CO<sub>2</sub>. In order to prevent excessive cooling of the reservoir, CO<sub>2</sub> injection in liquid or supercritical phase is preferred. However, considering the extremely low pressures of depleted gas fields, CO<sub>2</sub> injection in gaseous phase will generally be inevitable.

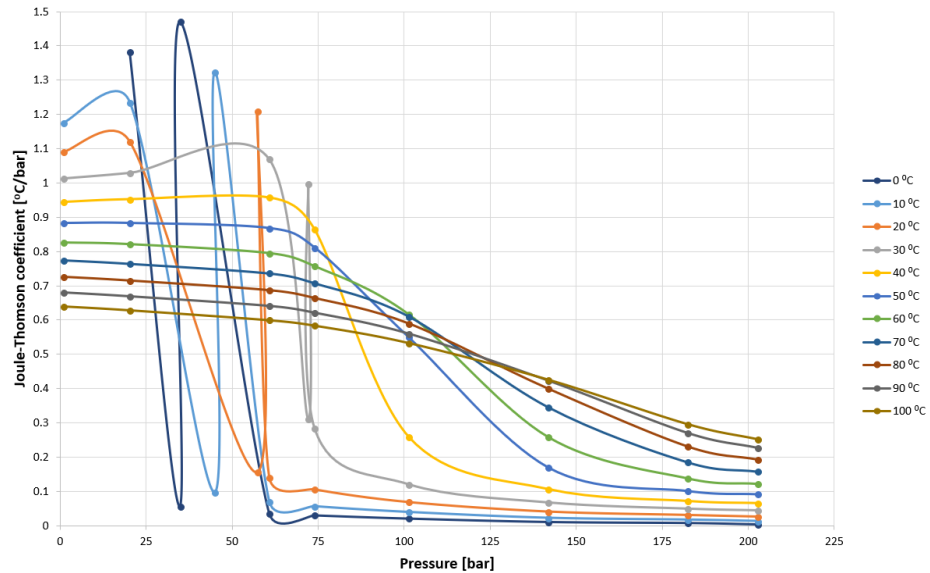


Figure 3.3: Joule-Thomson coefficients of pure CO<sub>2</sub> based on experimental data [59].

#### Joule-Thomson cooling induced by CO<sub>2</sub> injection in depleted gas fields

Depleted gas fields are commonly at extremely low pressure conditions (i.e. <50 bar) at the onset of the injection phase. To ensure flow of CO<sub>2</sub> from the wellbore into the reservoir, CO<sub>2</sub> is injected at pressures higher than reservoir pressures. As a consequence, a pressure differential arises in the near wellbore region, i.e.,

$$\Delta p = p_{bh} - p_{avg}. \quad (3.5)$$

This pressure differential is related to the CO<sub>2</sub> injection rate and injectivity of the formation [11], as shown in the equations provided in paragraph 2.3.4. By combining equation 3.4 and 3.5, it can be stated that the amount of cooling of injected CO<sub>2</sub> is a combination of the magnitude of this pressure differential and the JT coefficient. Nonetheless, as shown in figure 3.3, the value of the JT coefficient is highly dependent on the local pressure and temperature. These conditions strongly vary during the injection process and the magnitude of the Joule-Thomson cooling (JTC) is therefore also highly variable during the injection phase.

### Analytical solution for Joule-Thomson cooling

Mathias et al. [34] derived an analytical solution to quantify the cooling of the reservoir caused by the purely the JT effect of injected CO<sub>2</sub> in depleted gas reservoirs. Thermal effects other than the JTC as evaporation of water in the CO<sub>2</sub> phase or CO<sub>2</sub> dissolution are neglected. The steady-state analytical solution is based on a simplified heat transport equation and assumes incompressible single phase flow with constant fluid properties under steady-state conditions. Only two phases are considered, i.e. a non-aqueous phase and aqueous phase, entirely composed of CO<sub>2</sub> and H<sub>2</sub>O respectively. The minimum temperature, positioned at the discontinuity between the cooled reservoir by the JT effect and reservoir at initial condition outside the cooled region, is defined as

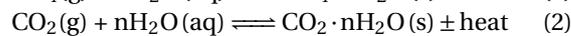
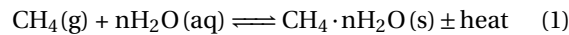
$$T_{min} = \frac{\mu_{jt} Q_{inj} \mu_{CO_2}}{4\pi h k_{r,CO_2} K \rho_{CO_2}} \times \ln \left\{ \left[ \frac{C_{p,CO_2}}{\phi(1 - S_{H_2O,r}) \rho_{CO_2} C_{p,CO_2} + \phi S_{H_2O,r} \rho_{H_2O} C_{p,H_2O} + (1 - \phi) \rho_r C_{p,r}} \right] \frac{Q_{inj} t}{\pi h r_w^2} + 1 \right\} + \begin{cases} T_0, & T_0 \leq T_w \\ T_w, & T_0 > T_w \end{cases} \quad (3.6)$$

where  $Q_{inj}$  is the CO<sub>2</sub> injection mass rate,  $h$  is the reservoir height,  $t$  is the time,  $T_0$  is the reference or initial temperature and  $T_w$  is the temperature at the well. In Appendix B.1, the full derivation of the analytical solution is presented.

## 3.2. Geochemical effects

### 3.2.1. Hydrate formation

Gas hydrates can be formed from hydrate forming guest molecules (i.e. CO<sub>2</sub> and CH<sub>4</sub>) and water [60]. Hydrates are defined as a solid phase composed of separate frameworks of connected water molecules in which the guest molecules are captured [17]. The kinetic reaction for the formation of CO<sub>2</sub> and CH<sub>4</sub> hydrates can be written [61] as



Formation of hydrates is an exothermic processes and releases heat to the reservoir. The quantity of hydrates formed is subject to the availability of the hydrate guest components and water and the magnitude of their contact surface. Scarcity of the water or guest molecules can constrain the hydrate formation. Favorable conditions for hydrate formation are generally high pressures and low temperatures. However, the exact hydrate stability conditions highly depend on the individual components and mixture composition present in the reservoir and in contact with the aqueous phase. Hydrate stability curves for pure methane and CO<sub>2</sub> are shown in figure 3.4a. The lines separating the phase regions represent three phase equilibria i.e. liquid water, hydrate and non-aqueous vapor (L<sub>w</sub>-H-V) or liquid water, hydrate and non-aqueous liquid (L<sub>w</sub>-H-L). The L<sub>w</sub>-H-L equilibrium can only exist for CO<sub>2</sub> at the conditions considered since CH<sub>4</sub> remains in vapor phase within the temperature and pressure range shown. Below pressures of approximately 73 bar, lower reservoir temperatures are required to form CH<sub>4</sub> hydrates compared to CO<sub>2</sub> hydrates. However, above 73 bar the opposite holds. Salinity of the formation water alters the hydrate deposition curves [19]. The curves shifts leftward as the salinity increases, indicating that a lower temperature is required before hydrates are formed. Moreover, stability conditions for CO<sub>2</sub>-CH<sub>4</sub> mixtures slightly deviate from the pure components but are bounded by the stability limits provided by the pure components [17].

In figure 3.4b, the hydrate deposition curve for a realistic hydrocarbon gas and CO<sub>2</sub> hydrates are depicted. Hydrates of hydrocarbon gases are stable at significantly higher reservoir temperatures compared to the pure CO<sub>2</sub> and methane at equivalent pressures. This is due to presence of additional components (e.g. ethane and propane) that alters the behavior of the hydrate system.

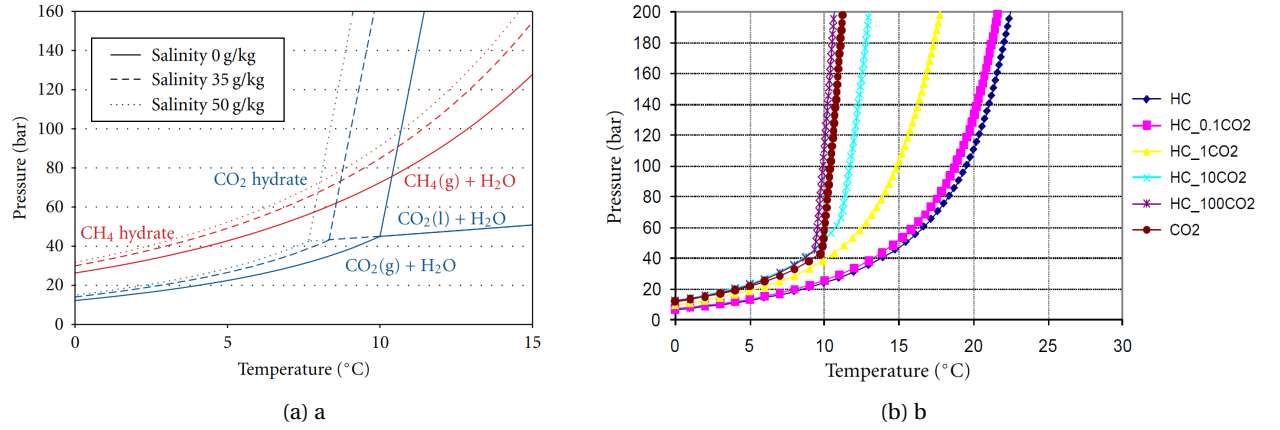
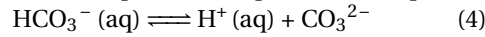
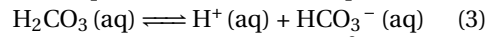
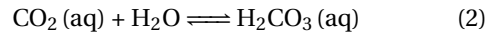
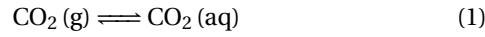


Figure 3.4: (a) Schematic phase diagram of a binary pure CO<sub>2</sub>-brine and CH<sub>4</sub>-brine system for different salinity values, modified after [19]; (b) Hydrate stability curves for pure CO<sub>2</sub> and mixtures with real natural hydrocarbon gas from a North Sea field [62].

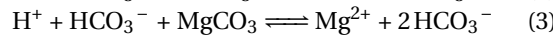
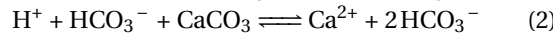
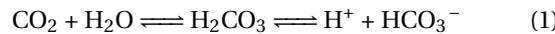
Because of the significant detrimental effect of hydrates on the permeability and subsequently on the injectivity of CO<sub>2</sub>, it is essential that the thermal processes related to CO<sub>2</sub> injection and the temperature distribution along the reservoir and in the near wellbore region are properly modeled [18]. Excessive JTC could lead to local temperatures and pressures within the hydrate formation region [11, 18, 34]. Eventually, effective operational measures should be adopted to prevent hydrate formation, which are preheating of CO<sub>2</sub> before injection, reduction of the CO<sub>2</sub> injection pressure, dehydration of the CO<sub>2</sub> to prevent condensation and the usage of inhibitors in order to reduce the formation temperature of hydrates [60].

### 3.2.2. Acid reactions

As CO<sub>2</sub> dissolves in water, it initiates a series of chemical reactions. Residual water starts to react with CO<sub>2</sub> directly after dissolution to form carbonic acid (H<sub>2</sub>CO<sub>3</sub>) that eventually dissociates in bicarbonate ions (HCO<sub>3</sub><sup>-</sup>). The latter can subsequently dissociate even further into carbonate ions (CO<sub>3</sub><sup>2-</sup>) [4]. Final equilibrium of these reactions depend on the amount of CO<sub>2</sub> dissolved and the local temperature. The induced chemical reactions by CO<sub>2</sub> dissolution are provided below:



Due to the creation of the carbonic acid, the pH of the water decreases. However, because carbonic acid is defined as a weak acid, the pH reduction is relatively limited. Nonetheless, precipitation or dissolution reactions will arise between the carbonic acid and formation minerals. Typical reactions stated below [63]:



The chemical reactions eventually lead to changes of the formation porosity and permeability due to the dissolution or precipitation of minerals. Especially for the integrity of the cap rock, it is essential that the geochemical reactions are well defined. Factors affecting the chemical reactions and equilibrium are the mineral composition of the formation, temperature, partial pressures, salinity of the reservoir fluids and gases and the pH of the aqueous phase. The aforementioned geochemical reactions act on different time scales and be divided accordingly [64]:

- Short term effects: dissolution of CO<sub>2</sub> in water and the formation of carbonic acid is characterized as short term effect.
- Mid and long term effects: precipitation and dissolution of minerals are generally slow reactions but the precipitation or dissolution rate strongly depends on the mineral type. In general, the dissolution or

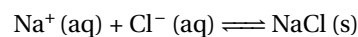
precipitation rates of carbonates and sulfides are relatively fast, in the order of days to weeks depending on the strength of the acid involved. On the other hand, mineral reactions with silicates or quartz can take up to thousands of years [4].

On the time scale considered in this research, where the main focus lays on the first years of the injection period, chemical reactions are trivial. In addition, majority of the depleted gas reservoirs, particularly in The Netherlands, are located in sandstone reservoirs. Clean sandstone reservoirs are primarily composed of the quartz that is not very reactive with the weak carbonic acid.

### 3.2.3. Salt precipitation reactions

Vaporization of the H<sub>2</sub>O into the CO<sub>2</sub> stream in the vicinity of the well during the injection process, causes precipitation of salt and reduces the local absolute permeability. The vaporization is a continuous process due to the constant supply of unsaturated CO<sub>2</sub>. Eventually, if an additional source brine source is absent and migration of water into the evaporation zone is obstructed (e.g. because the aqueous phase is immobile), the aqueous phase saturation decreases due the vaporization and the formation will dry-out [53, 65]. As the brine evaporates, the dissolved salt concentration increases and the aqueous phase becomes supersaturated, which initiates precipitation of the dissolved salt if the concentration limit has been reached. Over time, while assuming ongoing CO<sub>2</sub> injection, the dry-out front migrates further into the reservoir extending the dry-out zone and increasing the region with precipitated salt [65].

As mentioned earlier, in this research only the precipitation of sodium chloride (NaCl) is considered. The precipitation reaction of this salt is given by:



Salt precipitated in the near wellbore region reduces the local porosity and impairs the formation permeability. The permeability impairment has a detrimental effect on the injectivity of CO<sub>2</sub>. In certain cases, salt precipitation lead to a severe reduction of the permeability and eventually lead to entire clogging of the reservoir [53, 66]. The amount and area of salt precipitation in the near wellbore region is related to the initial salinity of the brine, salt solubility limit of the aqueous phase, initial brine saturation, solubility of water in the non-aqueous CO<sub>2</sub> phase, capillary pressures and CO<sub>2</sub> injection rate. Salt precipitation in the vicinity of the well consequently comprises a large variety of the physical processes and is therefore not a straightforward process [66].

The location of the salt precipitate in the porous medium, i.e. in the pore body or pore throat, determines the magnitude of the flow reduction through the pore network. Precipitation in the pore throat leads to a more significant reduction of the permeability compared to precipitation in the pore body. In experimental studies of formation dry-out by CO<sub>2</sub> injection on sandstone samples, two types of salt crystal morphologies were found, i.e. platy and hopper crystals. The formation of hopper type crystals indicate high crystallization rates by reaching highly super saturated conditions due to fast evaporation of water [16]. These salt crystals were found to precipitate and form a cover on both the pore throat and grain surfaces in the pore bodies during the dry-out process. Depleted gas reservoirs are generally characterized as water-wet, in which the injected CO<sub>2</sub> acts as the non-wetting phase and the brine acts as wetting phase [67]. Due to the water-wet behavior, the salt precipitate is not solely accumulating at the pore throat but also formed along the entire surface of the grain as laboratory experiments indicated. However, additional laboratory experiments are required for validation at the high injection rates considered, since the precipitation patterns and exact location of the precipitate are highly variable and depend on both rock and fluid parameters.

In reservoirs with high capillary pressures and mobile brine in combination with a low injection CO<sub>2</sub> injection rate, capillary backflow can occur. Capillary backflow is defined as the backward flow of brine from the region further in the reservoir into the dry-out zone that develops in the vicinity of the well due to vaporization of brine, in the opposite direction of the imposed CO<sub>2</sub> flow [53, 68]. This brine backflow is caused by the capillary pressure evolving due to the considerable contrast in brine saturation between the dry-out zone, where the saturation is zero, and the higher brine saturation outside the dry-out zone [65]. If the capillary pressure gradient evolving in the reservoir overcomes the pressure gradient in the reservoir induced by the injection, the brine backflow is initiated [68]. As a result of this backflow, more water will evaporate in the dry-out region, leading locally to a higher amount of salt precipitation and subsequently to higher permeability reduction or even full clogging of the reservoir.

### 3.3. Geomechanical

#### 3.3.1. Hydraulic and thermal fracturing

Depletion of a gas reservoir alters the stress regimes within the reservoir. During depletion the pore pressure and interrelated horizontal stresses in the reservoir reduce, causing compaction of the reservoir. The stress path followed during depletion process is entirely irreversible for the injection process, in case of elastic compaction and inflation [69]. Introduction of CO<sub>2</sub> in the reservoir perturbs the local stress regime [60]. At early injection stages, when the reservoir pressure is close to the initial pressure condition before the onset of injection and the horizontal stresses are small, injection of CO<sub>2</sub> at high rates can cause the bottom hole pressure to be high enough to exceed the pressure required to initiate a fracture.

The temperature difference between the injected cold CO<sub>2</sub> and warm formation, enhanced by JTC, causes a thermo-elastic stress to arise in the reservoir that reduces the critical pressure necessary to initiate fractures in the formation [58]. Hence, hydraulic and thermal fracturing are a combined inseparable effect. The relation between the temperature difference and the thermo-elastic stress is given by [70]

$$\Delta\sigma_t = \frac{\alpha_T E \Delta T}{1 - \nu}, \quad (3.7)$$

where  $\Delta T$  is the temperature difference between the cold CO<sub>2</sub> and the warm formation,  $\alpha_T$  is the thermo-elastic coefficient,  $E$  is the Young's modulus and  $\nu$  the Poisson's ratio.

The critical pore fluid pressure required to initiate a fracture in the formation can be calculated using [70]

$$p_b = 3S_{h,min} - S_{H,max} - p_p - \Delta\sigma_t, \quad (3.8)$$

where  $p_p$  is the pore fluid pressure and  $S_{h,min}$  and  $S_{H,max}$  are the minimum and maximum principal horizontal stress in the subsurface respectively.

Especially for cases with excessive reservoir cooling due to the JT effect, the thermo-elastic stress increase will be substantial. Therefore, significantly less pressure is required to initiate fractures. Development of fractures are favorable for the injectivity in the formation, but at the same time also impact the CO<sub>2</sub> flow pattern and could potentially threaten caprock integrity or wellbore stability if the fractures migrate towards and penetrate through these boundaries [58, 60].

# 4

## Numerical simulators and simulation overview

For injection of CO<sub>2</sub> in gas reservoirs at depleted conditions, it is essential that the simulator appropriately incorporates the corresponding thermal processes, phase changes and allows coexistence of multiple non-aqueous phases. Because the phase behavior of CO<sub>2</sub> is highly sensitive at depleted conditions, the CO<sub>2</sub> easily changes phase which significantly impacts its thermophysical properties. As a matter of fact, phase changes along the reservoir during the sequestration processes are inevitable.

### 4.1. Numerical simulators

To investigate the strongly coupled near wellbore effects, two compositional simulators are used: the academic simulator TOUGH2 developed by LBNL and the commercial simulator CMG GEM. The former consist of distinct fluid property (EOS) modules of which the ECO2MG module, developed by TNO, is utilized in this research. Both the TOUGH2 module and GEM are capable of performing non-isothermal compositional multi-phase simulations including salt precipitation and phase changes. However, the internal thermodynamic models and capabilities deviate. A comprehensive overview of the capabilities of each individual simulators is provided in table 4.1. Compared to other numerical simulators, ECO2MG and GEM are found to be currently the only modules able to incorporate all the considered (thermo)physical effects addressed in this thesis in coupled manner. The simulation packages are discussed in more detail in the following paragraphs.

#### 4.1.1. TOUGH2 ECO2MG

ECO2MG is an extended version of the original ECO2M module, which was explicitly developed for CO<sub>2</sub>-H<sub>2</sub>O-NaCl systems. The ECO2MG module has the ability to simulate CO<sub>2</sub>-CH<sub>4</sub>-H<sub>2</sub>O-NaCl system including phase transitions and accounts for the presence of a brine and solid salt phase [32]. The salt can dissolve in or precipitate from the aqueous phase perturbing the local permeability of the formation. ECO2MG contains, in contrast to the ECO2M module which is based on Altuniz correlations, 3-dimensional PVT-x tables to obtain the thermophysical properties (i.e. density, viscosity and specific enthalpy) of the mixture according to the composition and pressure and temperature conditions. PVT data is provided for distinct CO<sub>2</sub>-CH<sub>4</sub> compositions, i.e. 0%, 20%, 33% and 100% CO<sub>2</sub>. Intermediate compositions are interpolated using an interpolation algorithm. However, this algorithm requires a unique temperature on the dew-point and bubble-point line. Therefore, to meet this criterion the dew-point lines and pseudo critical points of the CO<sub>2</sub>-CH<sub>4</sub> phase envelopes are slightly adjusted to ensure monotonically increasing dew-point lines (see Appendix C.1) [32]. This causes a slight error close to the critical point in the phase envelopes.

### 4.1.2. CMG GEM

GEM is capable of non-isothermal compositional multi-phase modeling of both CO<sub>2</sub> storage in saline aquifers and depleted gas reservoirs. Besides componential transport, energy and thermodynamic equilibrium equations, CMG also incorporates geochemistry and geomechanical equations in a coupled approach. Hence, compared to ECO2MG, GEM allows for further examination of the impact of CO<sub>2</sub> injection on potential chemical and geomechanical processes. Due to the flexible handling of components in the EOS in GEM, the fluid system is not limited to straightforward CO<sub>2</sub>-(CH<sub>4</sub>-)brine systems but can be extended to include contaminants as H<sub>2</sub>S and SO<sub>2</sub>. Similar to ECO2MG, thermal and physical effects of vaporization of H<sub>2</sub>O into the non-aqueous phase and dissolution of the non-aqueous phase components into the aqueous can be modeled in GEM. The EOS utilized for the properties of the non-aqueous phase is the PR EOS (1978). Aqueous phase properties are obtained from the Rowe and Chou (1970) and Kestin et al. (1981) correlations [27].

Table 4.1: Comparison of the internal numerical models and capabilities of the ECO2MG and GEM simulator.

	ECO2MG	GEM
<b>Multi-phase</b>	✓	✓
<b>Non-isothermal</b>	✓	✓
<b>Components sytem</b>	CO <sub>2</sub> -CH <sub>4</sub> -H <sub>2</sub> O-NaCl	CO <sub>2</sub> -CH <sub>4</sub> -H <sub>2</sub> O-NaCl <sup>a</sup>
<b>Phase partitioning model (EOS)</b>	Modified Spycher & Pruess (2005) <sup>b</sup> (tabular PVT-x)	Undisclosed (PR-EOS)
<b>Salt precipitation</b>	✓	✓
<b>Permeability reduction</b>	✓ (Verma-Pruess eq. 2.14)	✓ (Carman-Kozeny eq. 2.18)
<b>Water vaporization</b>	✓	✓
<b>CO<sub>2</sub> solubility</b>	✓ (Henry's law)	✓ (Harvey's (1996) correlation)
<b>Geochemical reactions</b>	X	✓ <sup>c</sup>
<b>Geomechanics</b>	X	X <sup>d</sup>
<b>Relative perm.</b>	Modified Corey (eq. 2.47)	tabular <sup>e</sup>
<b>Capillary press.</b>	Van Genuchten (eq. 2.52)	tabular <sup>e</sup>

<sup>a</sup> the component system in GEM is flexible and components can be added or removed.

<sup>b</sup> a detailed description of the phase partitioning and EOS is provided by Loeve [32].

<sup>c</sup> the salt precipitation reaction in GEM is referred to as an aqueous chemical reaction; rock mineral reactions are possible but not considered in this research.

<sup>d</sup> possible, but not included.

<sup>e</sup> values are set equivalent to the Modified Corey and Van Genuchten models.

The interactions and partitioning of the components between the different phases for a depleted gas reservoir system (i.e. CO<sub>2</sub>-CH<sub>4</sub>-H<sub>2</sub>O-NaCl) modeled in GEM and ECO2MG is schematically displayed in figure 4.1 along side the less complex saline aquifer system (i.e. CO<sub>2</sub>-H<sub>2</sub>O-NaCl). Note that the chemical reactions of the carbonic acid are not included in this work.

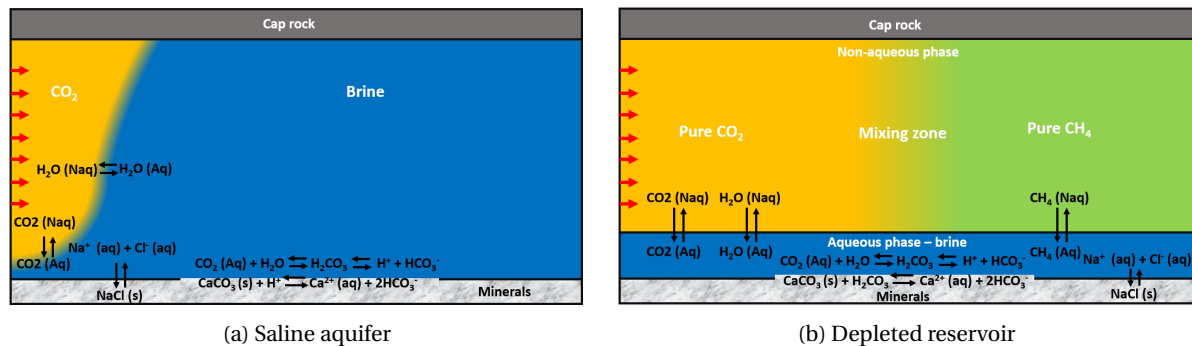


Figure 4.1: Schematic representations of CO<sub>2</sub> injection in a saline aquifer (a) and depleted gas reservoir with initial CH<sub>4</sub> (b), including the component exchange between phases due to vaporization, dissolution and chemical reactions.

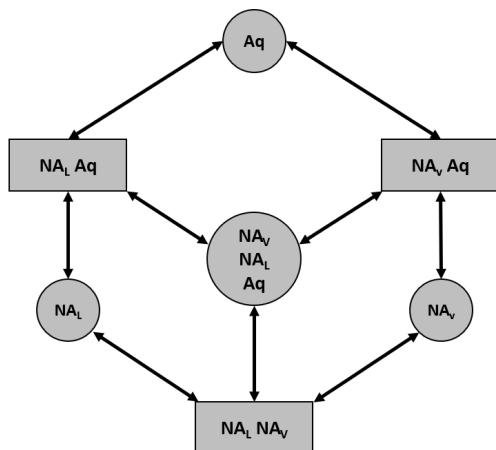


Figure 4.2: Overview of the phase combinations and transitions captured by ECO2MG and GEM (excluding the solid salt phase), modified after [29, 32].

Table 4.2: Primary variables for the phase conditions in ECO2MG [32].

Phase condition	Primary variables				
Aqueous only	$p$	$x_{NaCl}$	$x_{CO_2}$	$x_{CH_4}$	$T$
Liquid only	$p$	$x_{NaCl}$	$x_{CO_2}$	$x_{CH_4}$	$T$
Gas only	$p$	$x_{NaCl}$	$x_{CO_2}$	$x_{CH_4}$	$T$
Aqueous and liquid	$p$	$x_{NaCl}$	$S_{Aq}$	$x_{CH_4}$	$T$
Aqueous and gas	$p$	$x_{NaCl}$	$S_{Aq}$	$x_{CH_4}$	$T$
Liquid and gas	$p$	$x_{NaCl}$	$S_{NA_V}$	$x_{CH_4}$	$x_{H_2O}$
Three phase	$p$	$x_{NaCl}$	$S_{Aq}$	$x_{CH_4}$	$S_{NA_V}$

## 4.2. Phase combinations and simulation variables

As mentioned, ECO2MG and GEM are capable of modeling non-isothermal multi-phase  $CO_2$ - $CH_4$ - $H_2O$ - $NaCl$  systems and the corresponding phase changes. In figure 4.2, the possible phase combinations and transitions are depicted. It should be noted that an additional solid phase can be present simultaneously with the phases indicated in the figure, but is intentionally disregarded in the figure for brevity. To solve the flow and balance equations in these numerical models, primary thermodynamic variables need to be specified. The number of primary variables for a system, equivalent to the total degrees of freedom defined by the Gibbs' phase rule, is given by [71]

$$N_{pv} = D_f + N_p - 1 = N_c + 1, \quad (4.1)$$

where  $N_{pv}$  denotes the total number of primary variables and  $D_f$  denotes the degrees of freedom. In the considered depleted gas reservoir system consisting of 4 components, 5 primary variables should be defined. The primary variables required in ECO2MG, depend on the initial phase conditions within the system and are listed in table 4.2. Based on these primary variables, secondary parameters are calculated by the EOS which are necessary to assemble the balance equations. After each iteration the primary variables are updated and re-initialized in case of phase changes [71]. The secondary parameters, determined for each separate phase are the saturation, density, viscosity, specific enthalpy, relative permeability, capillary pressure, component mass fractions (i.e.  $CO_2$ ,  $H_2O$ ,  $NaCl$  and  $CH_4$ ) and diffusion coefficients. Contrary to ECO2MG, having a highly modular structure with a distinct primary variable and secondary parameter format, a fixed set of parameters needs to be specified in GEM regardless of the phase condition due to its model structure.

## 4.3. Simulation overview and work flow

To comprehensively examine the appearance and magnitude of the near wellbore effects, various simulation studies are conducted in a structured order throughout this research. Overall, the complexity of the simulations with respect to the involved physics and reservoir heterogeneity are increased for each consecutive study. First a sensitivity study is performed on a simplistic 1D radial reservoir, which is subsequently extended to 2D cylindrical domains with more complex heterogeneities. Thereafter, the injection scenarios and impurities are simulated. Finally, a realistic geological model is implemented to study the near wellbore effects on a field scale. For the sensitivity study and first part of the near wellbore cooling management (i.e. injection scenarios), the ECO2MG module is utilized because of the obvious handling of salt precipitation and the easily tune-able permeability reduction model. On the other hand, the second part of the near wellbore cooling management (i.e. introduction of impurities) and the full 3D field case is simulated with CMG GEM, due to higher flexibility of GEM's EOS for addition or removal of components and the straightforward processing of 3D geological models. An overview of the simulations and corresponding simulator for each part is shown in figure 4.3.

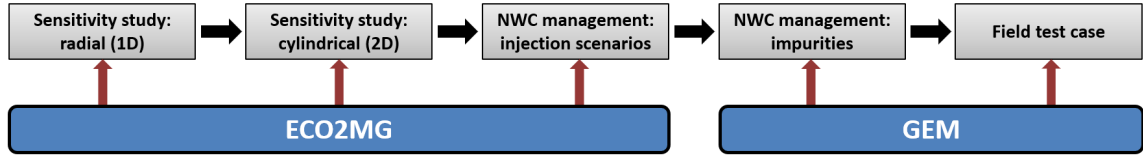


Figure 4.3: Overview of the sequence of performed simulation studies in this research, in which the simulator utilized for each study is indicated.

## 4.4. Simulation models

### 4.4.1. 1D and 2D sensitivity study and near wellbore cooling management

For the sensitivity study, a base case scenario is defined to determine the influence of perturbations on relative change with respect to the base case. The input parameters for this base case are listed in table 4.3. Injection temperature and reservoir temperature are set to be equal in order to minimize the influence of the undisturbed reservoir on the effects in the near wellbore region. Changes to the input parameters will be mentioned for each case and remain the same if not mentioned otherwise.

Table 4.3: Input parameters and initial conditions for the base case scenario of the sensitivity study.

Parameter	Value (unit)	Parameter	Value (unit)	Parameter	Value (unit)
$Q_{inj}$	35 (kg/s)	$x_{NaCl}$	15 (wt%)	$k_{r,\alpha}$	modified Corey 2.47
$p_{res,ini}$	40 (bar)	$T_{inj}$	45 ( $^{\circ}$ C)	$S_{Aq,r}$	0.2 (-)
$\phi$	0.12 (-)	$T_{res,ini}$	45 ( $^{\circ}$ C)	$S_{NA_L,r}$	0.1 (-)
$K$	100 (mD)	$\Gamma$	0.8 (-)	$S_{NA_V,r}$	0.01 (-)
$h$	50 (m)	$\phi_r$	0.8 (-)	$n$	3 (-)
$R$	4000 (m)	$\rho_r$	2600 (kg/m <sup>3</sup> )	$p_c$	no capillary pressure
$S_{Aq}$	0.2 (-)	$C_{p,r}$	920 (J/kg/ $^{\circ}$ C)	$\lambda_r$	2.52 (W/m/ $^{\circ}$ C)

### Model geometries

Simulations in the 1D sensitivity study and near wellbore cooling management section are all conducted on a 1D radial homogeneous model with a constant CO<sub>2</sub> injection rate. The dimensions, number of grid cells and grid spacing of the radial model are shown in figure 4.4. Within the cell distribution given in the figure, the cells are logarithmically spaced to provide an adequate resolution in the near wellbore area, while having large cells close to the outer boundary. For the 2D sensitivity study, the initial radial model is converted into a cylindrical model by dividing the model in 20 equidistant grid cells of 2.5 m in vertical direction. The dimensions of the 2D reservoir are equivalent to the 1D case. However, in contrast to the 1D simulations, a grid with 400 logarithmic spaced cells divided over the entire domain in lateral direction is implemented, to enhance the stability of the ECO2MG simulator. In addition, as mentioned, different degrees of heterogeneity are applied which are discussed in detail in paragraph 5.2.

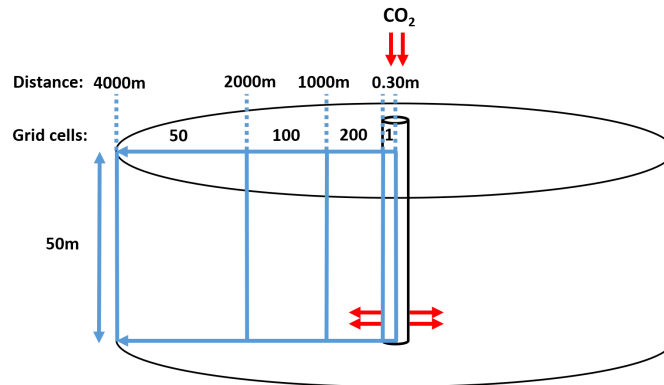


Figure 4.4: Radial model including the logarithmic grid distribution implemented in the 1D sensitivity study, injection rate scenarios and impurity simulations, modified after [23].

### Boundary conditions

The boundary conditions for this radial model are a no flux boundary (i.e. Dirichlet boundary condition) at outer boundary of the model domain and a constant (in)flux at the well location (i.e. Neumann boundary condition).

#### 4.4.2. P18-4 test case

As basis for the P18-4 field test case, a geological field model of the P18 field received from TNO and initially developed by TAQA, is utilized. The geological features and properties of the P18-4 compartment are exported to CMG GEM and non-isothermal CO<sub>2</sub> injection simulations are conducted. The model geometry and initialization are further discussed in chapter 7.

#### 4.4.3. Case overview and incorporated physics

In the numerous simulations conducted, certain physical effects are in- and excluded, to test the influence of this physical effect on the behavior of the system, or are not incorporated due to modeling limitations. Therefore, each simulation case has been numbered and a clarifying overview of the simulation characteristics and incorporated physics are provided in table 4.4.

Table 4.4: Overview of the incorporated physics and characteristics for each simulation case.

Simulator /method*	Case no.	Ther.	Salt prec.	Perm. red.	Grav.	H <sub>2</sub> O vap.	CO <sub>2</sub> diss.	Mob. brine	Cap. press.	Geom.	Hetro.	Heat exc.
<b>ECO2MG</b>	1-10	✓	✓	X	X	✓	✓	X	X	1D-R	X	X
	11	✓	✓	✓	X	✓	✓	X	X	1D-R	X	X
	12-14	✓	✓	X	X	✓	✓	X	X	1D-R	X	X
	15	✓	✓	X	X	✓	✓	✓	X	1D-R	X	X
	16-17	✓	✓	✓	✓	✓	✓	X	X	2D-C	X	X
	18	✓	✓	✓	✓	✓	✓	X	X	2D-C	X	✓
	19-20	✓	✓	✓	✓	✓	✓	X	X	2D-C	✓	X
	21	✓	X	X	X	X	X	X	X	1D-R	X	X
	22	✓	✓	✓	X	✓	✓	X	X	1D-R	X	X
<b>GEM</b>	21	✓	X	X	X	X	X	X	X	1D-R	X	X
	22	✓	✓	✓	X	✓	✓	X	X	1D-R	X	X
	24-25	✓	X	X	X	✓	✓	X	X	1D-R	X	X
	26	✓	X	X	✓	✓	✓	✓	✓	3D	✓	X
<b>Analytical</b>	21	✓	X	X	X	X	X	X	X	1D-R	X	X

\* the abbreviations in the headlines of the columns are respectively: thermal (ther.), salt precipitation (salt prec.), permeability reduction (perm. red.), gravity (grav.), water vaporization (H<sub>2</sub>O vap.), CO<sub>2</sub> dissolution (CO<sub>2</sub> diss.), mobile brine phase at initial condition (mob. brine), capillary pressure (cap. press.), geometry (geom.), heterogeneity (hetro.) and heat exchange with confining layers (heat exc.).

# 5

## Simulation results and discussion

The distribution of CO<sub>2</sub> injected in depleted gas fields are, at the time scale considered, primarily controlled by the following flow and transport mechanisms [4]:

- Migration of CO<sub>2</sub> as a results of the imposed pressure gradient due to injection;
- Migration of CO<sub>2</sub> induced by natural hydraulic gradients and capillary pressures;
- Buoyancy and gravitational forces due to the density contrasts between the injected CO<sub>2</sub> and initial reservoir fluids, intensified by induced thermal effects during injection.
- Fingering and dispersion induced by mobility differences between the injected CO<sub>2</sub> and initial reservoir fluids and by local reservoir heterogeneity;
- Dissolution of CO<sub>2</sub> in reservoir fluids and vaporization of H<sub>2</sub>O;
- Mineral precipitation and dissolution;
- Diffusion caused by concentration gradients.

Near wellbore effects induced by CO<sub>2</sub> injection comprises and impacts several of the mentioned mechanisms. In this chapter, the CO<sub>2</sub> injection simulation results are displayed and discussed. First a sensitivity study is conducted on the influence of the injection parameters and reservoir properties on the magnitude of near wellbore effects and their influence on flow processes in the reservoir. Thereafter, the change of effective permeability due to physical effects as dry-out and salt precipitation is examined, and a comparison study between the numerical models and analytical solution is performed.

### 5.1. 1D sensitivity study

#### 5.1.1. Base case - Reservoir dynamics: thermal effects, flow behavior and phase change Thermal effects and saturation distribution

Injection of CO<sub>2</sub> in the reservoir, initiates the extensively discussed (thermo)physical effects, causing a distinct temperature, pressure and saturation profile to arise in the reservoir. The simulation results of the base case scenario after one year of injection are shown in figure 5.1.

In the saturation profile three flow regions can be identified: (1) Single phase fluid region close to the well, where the brine phase is entirely evaporated into the continuously injected dry CO<sub>2</sub> and salt has been precipitated, in the so called dry-out zone; (2) Two phase fluid region behind the CO<sub>2</sub>-CH<sub>4</sub> mixing front with a non-aqueous phase fully composed of CO<sub>2</sub> and the initially present aqueous phase; (3) Two phase region ahead of the CO<sub>2</sub>-CH<sub>4</sub> mixing front with a non-aqueous phase composed of initial CH<sub>4</sub> and an initially present aqueous phase.

Various thermal processes occur simultaneously in the reservoir during the injection. The thermal processes explicitly treated are JTC, endothermic water vaporization and exothermic CO<sub>2</sub> dissolution. As Han et al. [23] substantiated, the mentioned thermal processes act and dominate in different regions in the reservoir. To define these regions properly, three simulations are conducted, in which for each simulation different thermal effects are included. The corresponding regions, indicated in the temperature profile shown in 5.1 (bottom), are discussed below:

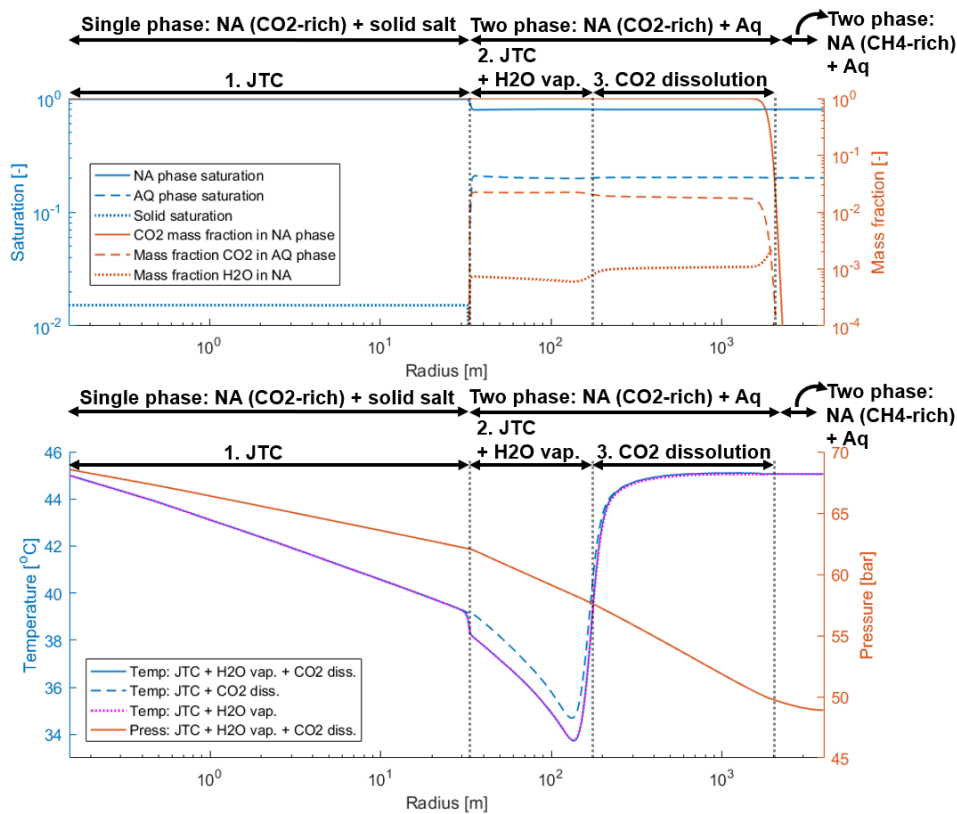


Figure 5.1: (Case 1)(top) Components and saturation distribution after 1 year of injection for a simulation in which all thermal effects are enabled and (bottom) temperature and pressure profiles in the reservoir after 1 year of injection for 3 simulations with different thermal effects included, where the region in which each thermal effect dominates is indicated at the top. Here, the abbreviations NA, Aq, JTC and vap. represent non-aqueous phase, aqueous phase, Joule-Thomson cooling and vaporization respectively.

- Region 1 (Joule-Thomson cooling): the aqueous phase in this region closest to the well has been entirely evaporated and the reservoir is locally dried-out. Cooling in this part of the reservoir is therefore only caused by the JTC of the injected CO<sub>2</sub> phase.
- Region 2 (Joule-Thomson cooling and water vaporization): in this region the temperature in the reservoir is dominated by a combination of water vaporization and JTC. Water evaporation induces an additional temperature drop of 2°C on top of the JTC effect with the considered base case parameters. The contribution of the exothermic CO<sub>2</sub> dissolution on the reservoir temperature in this region negligible.
- Region 3 (CO<sub>2</sub> dissolution): at larger distances from the well, the dominance of particularly the JTC reduces due to the lower pressure gradient and the exothermic dissolution effect of CO<sub>2</sub> becomes more exposed. Due to reduction of the JTC and heat conduction of the warm undistributed reservoir, the temperature profile restores to initial reservoir temperature. The exothermic dissolution causes the temperature to rise slightly above the initial reservoir temperature. This final region extends upto the CO<sub>2</sub> mixing front. However, the exothermic effect of dissolution is small at the prevailing pressure.

The boundaries of the mentioned regions are not static, but migrate further into the reservoir over the injection time. The migration rate of these boundaries are directly related to the CO<sub>2</sub> injection rate. Based on the figure, it can be stated that, for the given injection rate and initial pressure, the cooling is predominantly caused by the JT effect. Due to the large pressure gradient induced in the reservoir by the imposed injection and high JT coefficient of the CO<sub>2</sub> at the prevailing conditions, the JTC is quite substantial.

In the pressure profile a distinct deflection in pressure at the boundary between the single phase zone and two phase zone is observed, that is caused by the abrupt change in relative permeability due to the transition from a dried-out region to a region where the aqueous phase is present. This alters the pressure behavior and enhances the pressure gradient, subsequently increasing the JTC. Due to the assumption of instantaneous thermodynamic equilibrium, the transition from a dried-out to undried region, marked by the evaporation front, is sharp [68].

### Flow behavior

Transport in this multi-component system is driven by advection and diffusion [26]. Advection is the combined effect of gravitational and injection forces. The gravitational forces are oriented perpendicular to the horizontal injection forces. In the vicinity of the well the transport is dominated by advection, in particular by the injection forces due to large imposed flow rates. Far from the well, diffusion, which is induced by concentration gradients, becomes more important due to the reduction of the flow velocity in radial models as the radius increases [26]. Since this research focuses on the advection dominated near wellbore region, diffusion is neglected.

The pressure behavior in the reservoir during injection, i.e. the spatial distribution, pressure gradient and rate of the pressure buildup, is affected by injection parameters, reservoir properties (e.g. reservoir geometry and heterogeneity) and presence of reservoir fluids and their properties [4]. As given in equations 2.44 and 2.45, the imposed pressure gradient by constant rate injection is attributed to the injectivity of the CO<sub>2</sub> in the formation while the rate of the pressure buildup is for a given injection rate directly related to size of the reservoir.

As CO<sub>2</sub> is injected in a depleted gas reservoir, it starts to mix with the CH<sub>4</sub> and due to their miscible characteristics [4, 72]. The flow behavior of the phases in the reservoir depend on the individual thermophysical properties of present components. In the reservoir a mixing zone will establish with the initial CH<sub>4</sub> components and injected CO<sub>2</sub> components at the leading and trailing edge respectively. This mixing zone migrates further into the reservoir over time. Displacement of brine by the injected CO<sub>2</sub> is assumed to be negligible, because the brine phase in depleted gas fields is regularly close to or at residual saturation and therefore hardly mobile. The efficiency of the displacement of the initial CH<sub>4</sub> by CO<sub>2</sub> within the non-aqueous phase can be expressed using the mobility ratio  $m = \mu_{CH_4} / \mu_{CO_2}$ . Since the viscosity of CO<sub>2</sub> in the pressure and temperature range of depleted gas reservoirs remains for the considered conditions higher than the viscosity CH<sub>4</sub>. The mobility ratio between CO<sub>2</sub> and CH<sub>4</sub> is therefore less than 1, indicating that stable displacement front will develop and viscous instabilities as fingering are limited [4]. In addition, this displacement process becomes even more stable as the reservoir repressurizes during the injection process, due to the increase in viscosity of CO<sub>2</sub> with increasing pressure.

Of significant importance for the near wellbore effects is that, shortly after the start of injection, all the CH<sub>4</sub> will be displaced by the injected CO<sub>2</sub> in the near wellbore region. At an injection rate of 35 kg/s with a reservoir height of 50 m, it takes only 10 days for the mixing front to reach a distance of 100 m from the well. The near wellbore region will therefore be fully saturated with CO<sub>2</sub> and brine. Nevertheless, the thermal front migrates significantly slower and retards far behind the mixing front (see figure 5.1). It can therefore be substantiated that the region in which the dominant thermal effects occur, converts rapidly in a CO<sub>2</sub>-brine system when assuming no capillary trapping of the CH<sub>4</sub> components. The thermophysical effects arising in the near wellbore region are therefore not directly attributed to the initial CH<sub>4</sub>. However, the presence of initial CH<sub>4</sub> remains to have an indirect influence on the pressure gradient throughout the reservoir, because it affects the flow behavior further in the reservoir. In Appendix D.1, a comparison is given between simulations on a CO<sub>2</sub>-brine system in which the initial CH<sub>4</sub> components are substituted by CO<sub>2</sub> and the CO<sub>2</sub>-CH<sub>4</sub>-brine considered in this research. At both sub- and supercritical condition, the outcome of the CO<sub>2</sub>-brine and CO<sub>2</sub>-CH<sub>4</sub>-brine systems are in reasonable correspondence.

### Phase change

The phase in which the CO<sub>2</sub> is injected in the reservoir is exceptionally important for the magnitude of the JTC in the near wellbore region. Injection of CO<sub>2</sub> in depleted reservoirs results in the buildup of the reservoir pressure. To examine the effect of phase changes on the JTC, a simulation is conducted in which CO<sub>2</sub> is injected over a period of 2 years. To accelerate the pressure buildup, a reservoir with radius of 1000 m is implemented instead of the original 4000 m used in the model of the sensitivity study. This reduces the required injection time to reach critical pressure from 11 years to 1 year, hereby shortening simulation time and enhancing visualization of the thermal fronts.

In figure 5.2, the temperature and pressure profiles over the injection time are depicted. Directly after the start of injection, a transient pressure behavior is observed in the reservoir. After approximately 20 days, the

boundary of the reservoir is reached and a semi-steady state flow develops. Due to the continuous injection, the reservoir pressure gradually increases over time. Eventually, the pressure in the reservoir reaches the critical pressure  $\text{CO}_2$ . When the reservoir pressure exceeds the critical pressure, the  $\text{CO}_2$  changes from gaseous to supercritical phase. The JT coefficient of  $\text{CO}_2$  depends on the local pressure and temperature in the reservoir, as shown in figure 3.3. Above the critical pressure the JT coefficient significantly reduces. Up to an injection time of 100 days in figure 5.2, in which the reservoir pressure has not exceeded the critical pressure yet, the minimum temperature in the reservoir reduces over time due to the strong JTC effect of the injected  $\text{CO}_2$ . The thermal front migrates away from the well into the reservoir. However, as the critical pressure is reached and the JT coefficient of  $\text{CO}_2$  reduces, the induced JTC becomes less. Hence, the minimum temperature in the reservoir starts to rise due to the lower magnitude of cooling and the heat conduction from the undisturbed formation and pore fluids at initial temperature further into the reservoir.

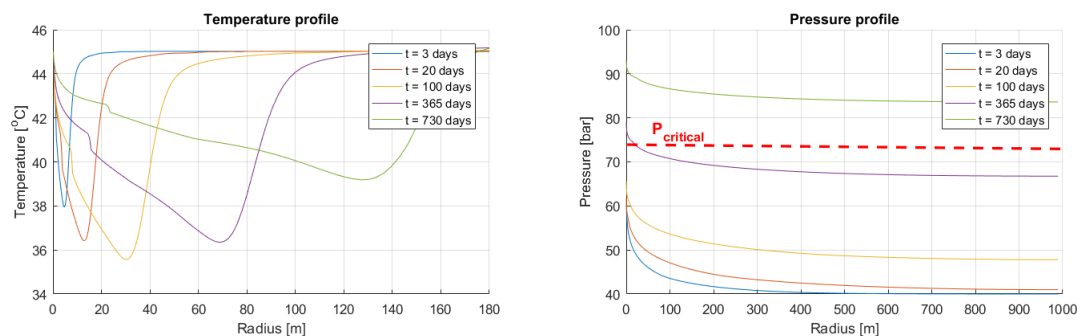


Figure 5.2: (Case 2)(left) Temperature profiles at different times during the injection process for a reservoir with a radius of 1000 m and (right) corresponding pressure profiles in which the red line indicates the critical pressure of  $\text{CO}_2$ .

### 5.1.2. Injection rate

The imposed injection rate of  $\text{CO}_2$  determines the induced pressure gradient in the reservoir. This gradient directly impacts the magnitude of the JTC in the reservoir, as indicated by equation 2.45. Figure 5.3 shows the temperature and pressure profiles for different injection rates. For higher injection rates, larger pressure gradients will establish which subsequently result in a higher JTC and lower minimum temperature in the reservoir. In addition, it should be noted that at higher injection rates, more  $\text{CO}_2$  is being injected. This leads to a larger cooling source compared to the low injection rate cases and therefore increases the discrepancy in minimum temperature reached for the different injection rates. Besides, the evaporation rate of water into the dry  $\text{CO}_2$  is directly related to the injection rate [68]. As a result, a higher injection rates, more water will evaporate and the dry-out front and the corresponding salt precipitation region will be further advanced into the reservoir.

### 5.1.3. Injection temperature

The temperature at which the  $\text{CO}_2$  is injected in the reservoir affects the magnitude of the thermophysical effects in the near wellbore region. In figure 5.4, the temperature profile, pressure profile, fraction of  $\text{H}_2\text{O}$  in the non aqueous  $\text{CO}_2$ -rich phase and phase distribution in the reservoir is shown. At an injection temperature of  $15^\circ\text{C}$  combined with a pressure above the vapor pressure of  $\text{CO}_2$ , the  $\text{CO}_2$  is in liquid phase as shown in the saturation distribution graph (see figure 5.4b). In liquid phase, the JT coefficient of  $\text{CO}_2$  is extremely low and the JTC is therefore limited. The cooling observed in the temperature profile is mainly due to the vaporization of water (only  $1.5^\circ\text{C}$ ). For the remaining injection temperatures, the  $\text{CO}_2$  is injected in gaseous phase. As the injection temperature is raised, the cooling induced by the JT effect reduces since the JT coefficient decreases with increasing temperature. However, this is opposed by the cooling caused by endothermic vaporization of water, (i.e. the sharp drop in temperature at the dry-out front). Water vaporization becomes more significant as the injection temperature is increased, because more water can evaporate in the  $\text{CO}_2$  stream as the temperature is raised.

### 5.1.4. Permeability

The permeability of the formation has an important influence of the injectivity of the  $\text{CO}_2$ . In low permeable formations, a higher pressure gradient is required to result in an equal rate in comparison to high permeable

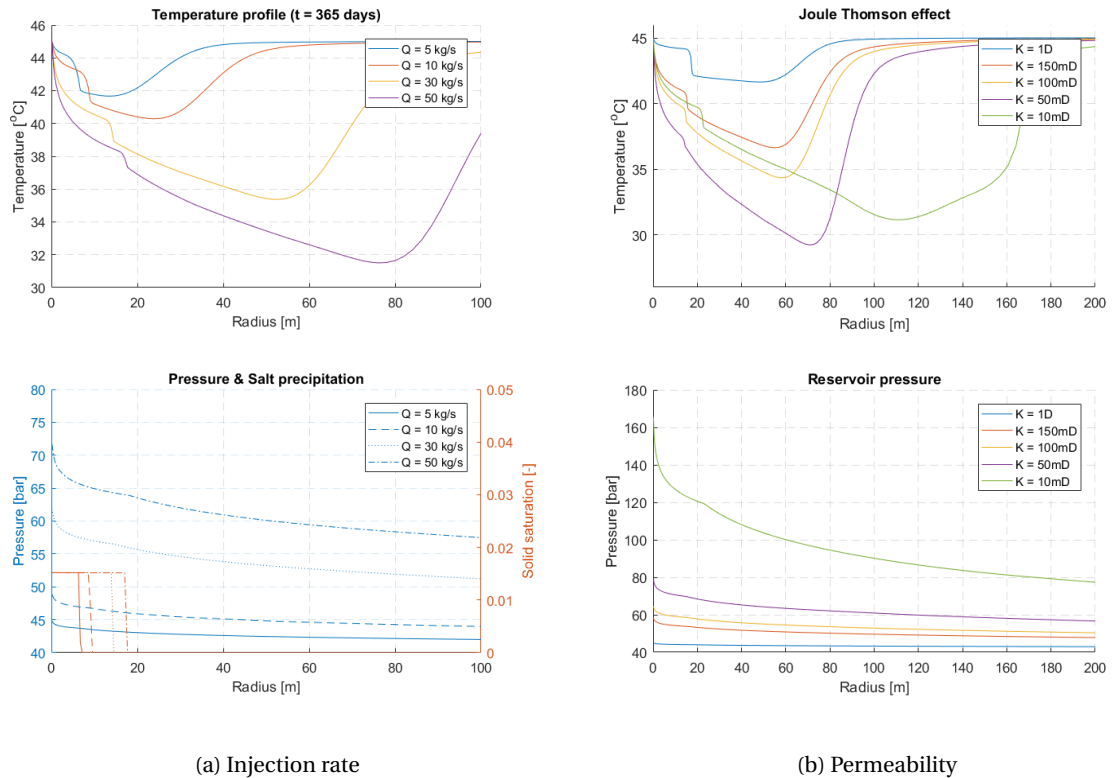


Figure 5.3: (Case 3&4) (a) Temperature, pressure and salt distribution for different CO<sub>2</sub> injection rates; (b) Temperature, pressure and salt distribution for different formation permeabilities.

formations. Figure 5.3b shows the simulation results for different absolute rock permeabilities. The cooling in the reservoir increases with decreasing permeability due to the higher pressure gradients in the reservoir. Deviant behavior is observed for the lowest simulated permeability (i.e. 10 mD). The minimum temperature reached is less than the 50 mD case, contradictory to the statement that the cooling increases for decreasing temperature. As mentioned earlier the magnitude of the JTC is a combination of the gradient of the pressure and the JT coefficient. Since the imposed flow rate causes a significant pressure gradient in the lowest permeability case, the absolute value of the pressure in the near wellbore region already exceeds the critical pressure of CO<sub>2</sub> shortly after injection. Hence, the CO<sub>2</sub> changes from gaseous phase to supercritical and the JT coefficient reduces. Therefore, although the pressure gradient in the lowest permeability case is larger than the 50 mD case, the cooling is less.

### 5.1.5. Porosity

The initial porosity of the formation describes the ratio between voids in the porous medium and the solid matrix. To reduce the temperature of the system consisting of fluid filled pores and the solid matrix, a particular amount of heat is required. This amount of heat required can be described by the effective volumetric heat capacity given in equation 2.7. The volumetric heat capacity is dependent on the porosity. A decrease in the porosity results in an increase of the volumetric heat capacity, due to the significant differences the rock and pore fluids especially the if non-aqueous phase is in gaseous conditions. Therefore, for lower porosity values more heat is required to change the temperature of the system. In figure 5.5, the simulation results for different porosity values are shown. The minimum temperature reached in the reservoir due to the cooling effects is lowest for the highest porosity (i.e. 0.24) and vice versa, as substantiated. In addition, as the porosity is reduced, less pore space will be available in the formation, leading to a faster buildup of the reservoir pressure and faster decrease JT coefficient and correlated cooling. Besides, although the vaporization rate remains constant for each simulation, the drying process in the reservoir is faster for lower porosity values. This is due to the fact that less water is present in the pores because of the constant simulation input value for the water saturation.

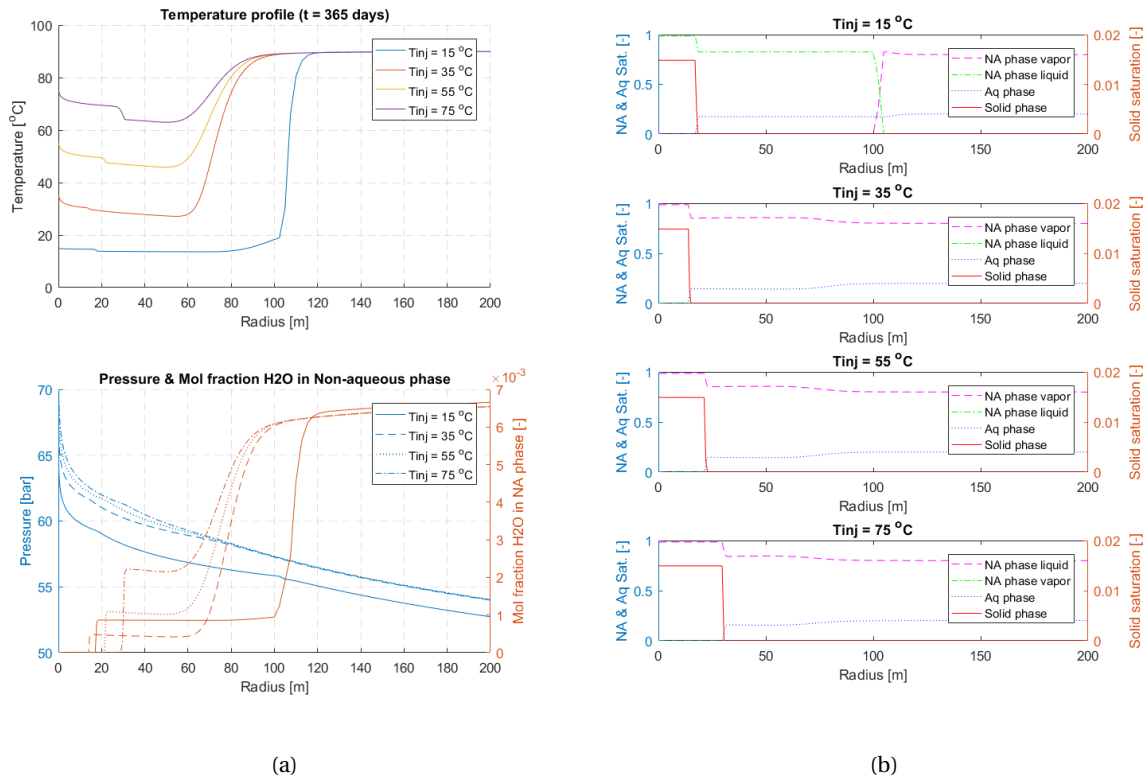


Figure 5.4: (Case 5) (a) Temperature, pressure and mole fraction of water in the non-aqueous phase and (b) saturation distributions for different CO<sub>2</sub> injection temperatures after 1 year of injection.

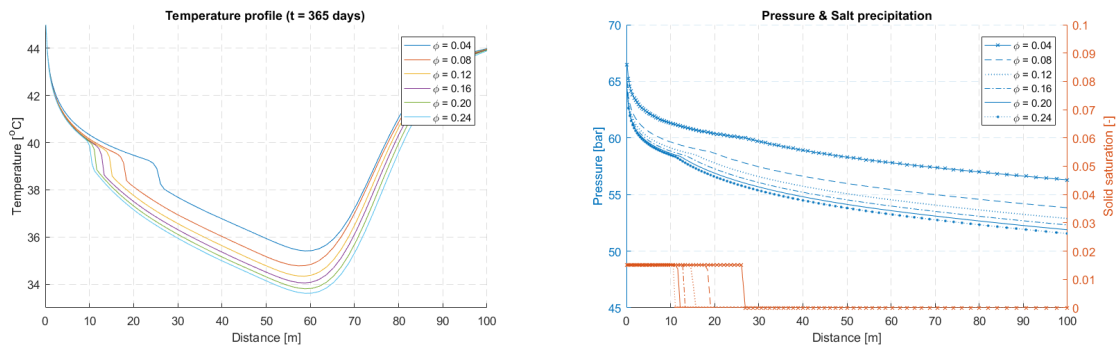


Figure 5.5: (Case 6) (left) Temperature profile for different rock porosity values and (right) corresponding pressure and solid salt profiles.

### 5.1.6. Initial reservoir pressure and temperature

The impact of the absolute value of the pressure on the JT coefficient and consequently on the cooling in the reservoir can be studied by implementing different initial reservoir pressures (see figure 5.6a). The induced gradient by injection in the reservoirs is roughly the same, but some deviations are visible due to the dependency of the fluid properties (e.g. viscosity, density and compressibility) on the pressure and temperature. At very low initial reservoir pressures, corresponding to highly depleted gas reservoirs, the JT coefficient of CO<sub>2</sub> is high, leading to significant JTC (i.e. approximately 13°C for an initial pressure of 20 bar). As the initial reservoir pressure is increased, the JT coefficient decreases and cooling reduces. In fields with a higher initial reservoir pressure for instance 100 bar, the JT coefficient is considerably smaller which results in a reservoir cooling of only 3°C.

In the base case scenario of this sensitivity study, the initial reservoir temperature is equal to the injection temperature (i.e. 45°C), to minimize the effect of the heat provided through conduction from the undis-

turbed reservoir ahead of the thermal front on the thermal effects in the near wellbore region. To examine the impact of this choice in initial reservoir temperature on the cooling and minimum temperature reached in the reservoir, simulations are conducted with different initial temperatures. As shown in figure 5.6b, the minimum temperature reached in the formation remains closer to the initial injection temperature as the reservoir temperature increases. This reduction in cooling of the formation can be attributed to a combination of a difference in absolute pressure value in the near wellbore region, affecting the JT coefficient, and difference in heat provided through conduction between the studied cases. At higher reservoir temperatures, the fluid properties of the phases (e.g. viscosity and density) become less favorable. As a result, the absolute pressure value is higher and the JT coefficient lower. Besides, more heat is provided through conduction from the reservoir ahead of the thermal front at higher reservoir temperatures, which reduces the cooling of the reservoir. Ultimately, the difference in minimum temperature reached in the reservoir for an initial reservoir temperature of 45 and 100°C is approximately 3°C and is therefore not substantial.

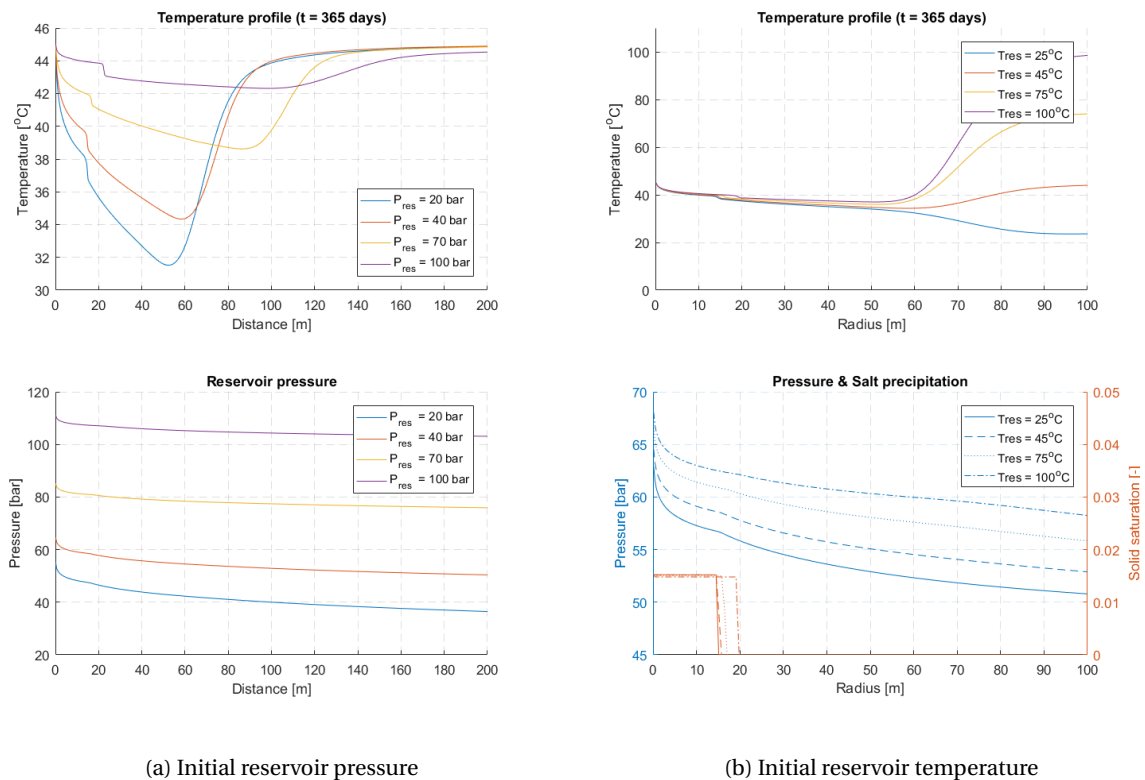


Figure 5.6: (Case 7&8)(a) Temperature and pressure profiles for different initial reservoir pressures; (b) Temperature and pressure profiles for different initial reservoir temperatures.

### 5.1.7. Reservoir size

The reservoir geometry and volume influence the rate of the pressure buildup of the reservoir. To study the effect of the reservoir repressurization rate on the cooling in the reservoir, the radius of the radial reservoir has been perturbed while the remaining parameters were fixed. The tested reservoirs therefore have different volumes and consequently different rates of pressure buildup. In figure 5.7a, temperature and pressure profiles are depicted. Obviously, the fastest pressure buildup occurs in the reservoir with the lowest volume (i.e. 0.04 bcm). After 1 year of injection, the pressure in the reservoir with the lowest volume is therefore already far above critical pressure. Hence, the cooling effect is small and the temperature remains close to initial injection temperature. As the reservoir volume increases, the rate of the pressure buildup reduces. For the remaining cases, the pressure remains below critical pressure after 1 year and the CO<sub>2</sub> is therefore injected in gaseous phase. Due to the slow pressure buildup, the absolute value of the pressure in the large volume reservoirs is close to initial pressure and the JT coefficient is high, which causes a stronger cooling effect. The temperature and pressure profile of the simulation on a 10 bcm reservoir overlaps the profiles of

the 2.5 bcm reservoir. This is due to the fact that in both reservoirs the flow remains in transient state since the outer boundary of the domain has not been reached by the pressure wave. Moreover, as a consequence of the high pressure in the reservoir with the smallest volume, more CO<sub>2</sub> dissolves in the aqueous phase. Since the dissolution of CO<sub>2</sub> is exothermic, the temperature subsequently increases above initial reservoir temperature.

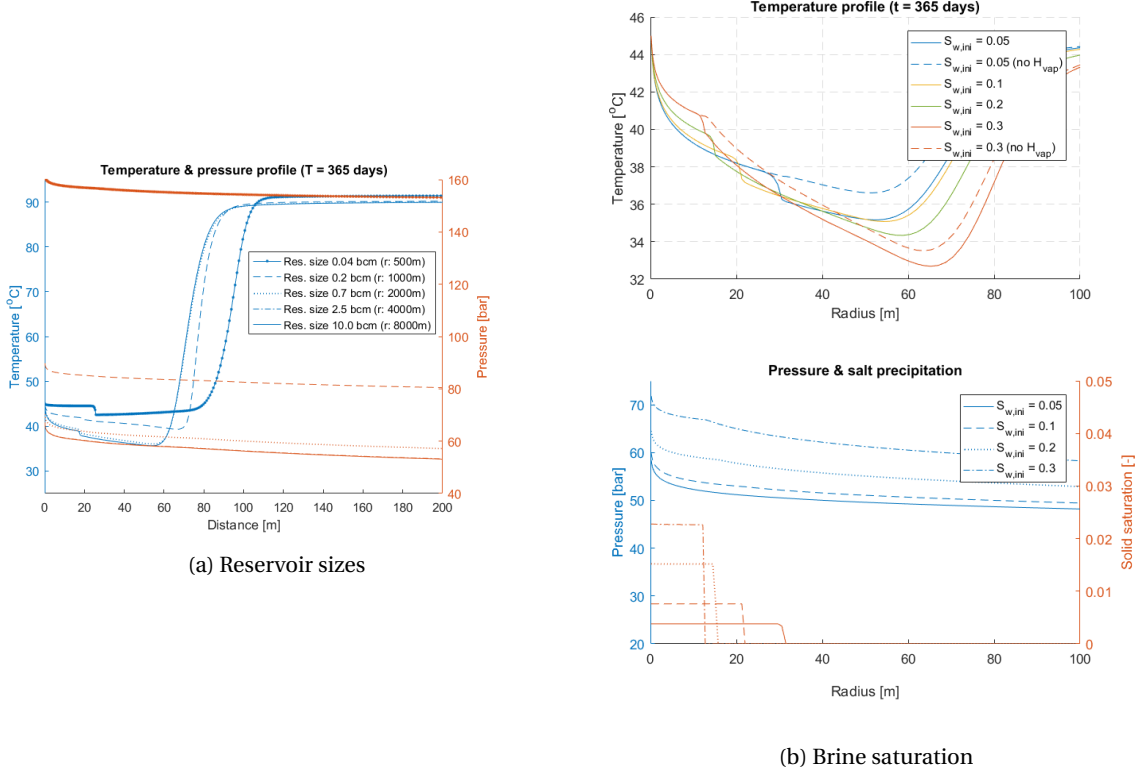


Figure 5.7: (Case 9&10) (a) Temperature and pressure profiles for different reservoir sizes ; (b) Temperature, pressure and saturation distribution for different initial brine saturations.

### 5.1.8. Brine saturation

The initial brine saturation and its salinity in the reservoir plays an important role on the near wellbore physics (e.g. the salt precipitation, water vaporization, relative permeability of the non-aqueous phase and the cooling effect). In figure 5.7b, the simulation results for different brine saturations are displayed. Brine is set to be immobile for all saturation values. As a consequence, the H<sub>2</sub>O components in the reservoir can only migrate after evaporation in and subsequently advection by the injected CO<sub>2</sub> phase [66]. Since the aqueous phase is immobile, the solid salt saturation after the aqueous phase is entire evaporated can be determined by an analytical solution, i.e. [68],

$$S_s = \frac{S_{Aq} \rho_{Aq} x_{NaCl}}{\rho_s} \quad (5.1)$$

Because the salinity for each case is equal, more salt has been precipitated in the simulation with the highest brine saturation (i.e.  $S_{Aq} = 0.3$ ). Since the salinity and injection rate for each case are constant, the evaporation rates are equal. Hence, the dry-out front is least advanced for the highest saturation case due to the fact that more time is required to evaporate the higher amount of water compared to the other cases.

Presence of brine reduces the relative permeability of the injected CO<sub>2</sub>. In the dry-out zone no water is present and the relative permeability of the CO<sub>2</sub>-rich phase equals unity. As mentioned, the distinct deflection in the pressure profile at the location of the dry-out front is caused by the sudden change in relative permeability of CO<sub>2</sub> before and behind the dry-out front. As the water saturation increases, the relative permeability change

increases which enlarges the deflection in the pressure profile. In front of the deflection, the pressure gradient is smallest for the highest water saturation while, on the other hand, the pressure gradient behind the dry-out front is largest for the highest brine case. This eventually causes a higher JTC and consequently reduction of the temperature compared in the highest brine case compared the other cases.

### 5.1.9. Salt precipitation

Various simulations have been conducted with different salinity values to study the salt precipitation of which the results are presented in figure 5.8a. The vaporization rate of water is influenced by the salinity of the aqueous phase. In the mutual solubility section in paragraph 2.1.5. it was shown that the amount of water that can evaporate in the CO<sub>2</sub> rich phase decreases with increasing salinity. Therefore, as displayed in figure 5.8, representing a time profile at a location 10 m from the well, dry-out is achieved earliest for the lowest brine salinity value. The reduction of permeability in the dry-out zone developed around the well, negatively affects the injectivity and induces a higher pressure gradient of this region as shown in the pressure profiles. This permeability reduction obviously increases with higher salinity values, because of the higher salt precipitation (see figure 5.8b). The increased permeability reduction, leading to a higher pressure gradient, enhances the cooling effect. However, the additional cooling observed in the temperature profiles due to the salt precipitation over the range of salinities studied, i.e. no salinity (0 wt% to extremely saline 25 wt%), is limited to 1.5°C for the implemented values in the Verma-Pruess reduction model.

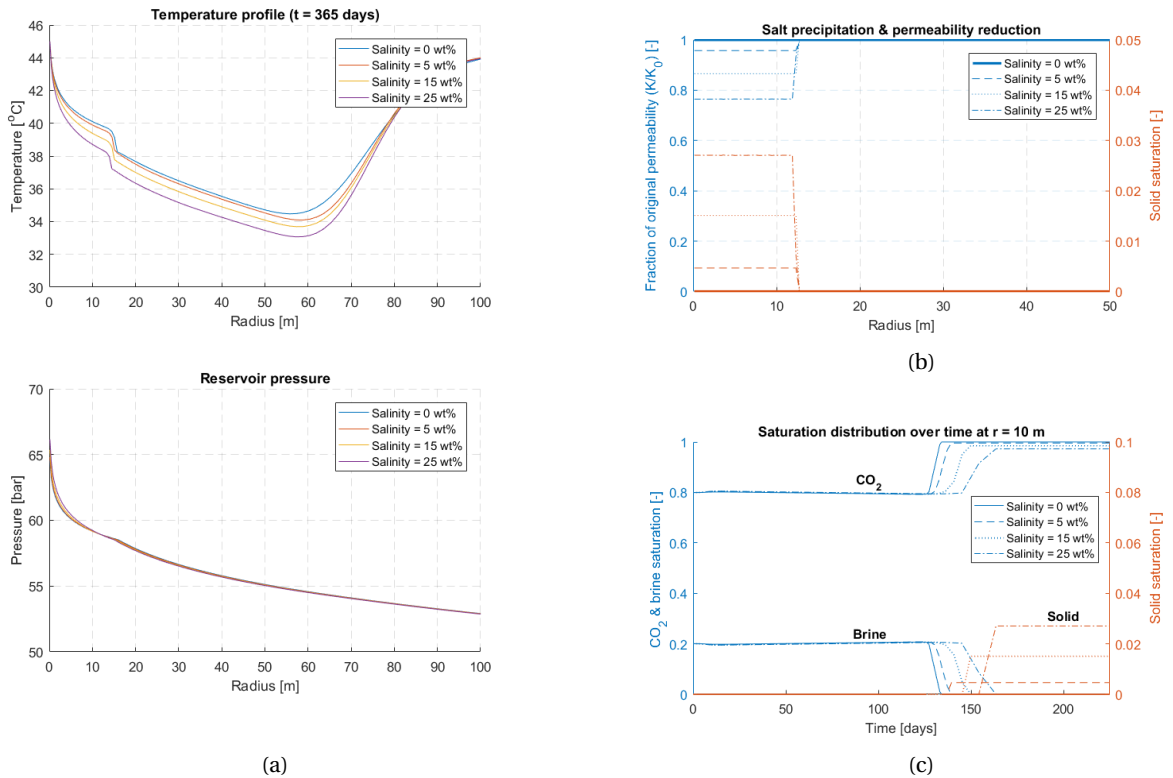


Figure 5.8: (Case 11)(a) Temperature and pressure profiles for different brine salinities; (b) Salt precipitation and corresponding permeability reduction profiles; (c) Saturation distribution over time at a radial distance of 10 m with respect to the well.

This Verma-Pruess model addressed in 2.3.1, used to calculate the permeability reduction, can be tuned by the parameters  $\phi_r$  and  $\Gamma$ . Particularly the parameter  $\phi_r$ , defining solid salt saturation at which complete clogging of the formation occurs, is important [46]. In literature, many values for these parameters have been proposed, ranging from 0.5 to 0.8 for  $\phi_r$  and 0.2 to 0.95 for  $\Gamma$  [15, 28, 38, 46, 53, 68, 73, 74]. For most modeling practices on sandstones, where experimental data of permeability reduction is absent, the parameters are set to the same values used in this research i.e.  $\Gamma = \phi_r = 0.8$ . The sensitivity with respect to these parameters is given in Appendix D.2. As expected, the cooling is mostly affected by changes in the critical porosity. In-

ing the critical porosity from 0.8 to 0.9, leads to a reduction of the permeability due to the salt precipitation of 0.73 instead of 0.85. However, this lowers the minimum temperature reached in the reservoir with only 1°C. Despite the considerable salinity of the brine, the amount of salt that precipitates in the near wellbore region is limited due to the low residual brine saturation. Hence, the permeability reduction at a critical porosity of 0.9 is not substantial enough.

#### 5.1.10. Relative permeability

The relative permeability curves of the phases impact the pressure distribution in the reservoir. Different relative permeability curves, obtained by implementing different end point values in the modified Corey model, have been studied. The simulation results are shown plotted in Appendix D figure D.2. For the range of relative permeability curves examined, the discrepancy in minimum temperature reached in the reservoir is small (i.e. less than 2°C). The cooling is most sensitive to changes in the Corey exponent of the relative permeability curve of the gaseous phase.

#### 5.1.11. Rock thermal properties

The rock density, heat capacity and thermal conductivity of the formation determine the rock thermal diffusivity. As indicated in equation 2.6, 2.8 and the effective volumetric heat capacity terms, the thermal properties of the rock highly affect the response of the temperature in the system to cooling effects induced by the injection of CO<sub>2</sub>. In Appendix D.4 the simulation results are shown for variations in values of these parameters. The density and heat capacity both influence the amount of heat required to change the temperature of the system. Increase in density or heat capacity with the same amount of cooling therefore results in lower reduction of the temperature in the system. Thermal conductivity of the formation determines the shape of the temperature front. For higher thermal conductivity values the thermal front will stretch out due to better conductance of the formation, while for lower thermal conductivity values the front sharpens. The deviations in minimum temperature reached for the wide range of values tested for the rock thermal properties are constrained within 2°C.

#### 5.1.12. Capillary pressure

In the previously discussed sensitivity cases, the brine phase was assumed to be immobile and capillary pressures were neglected. Potential effects of capillary pressure in ECO2MG are only relevant if the aqueous phase is mobile. Hence, the relative permeability functions, previously ensuring an immobile aqueous phase, have been slightly modified to enable flow of the aqueous phase by lowering the irreducible water saturation to 0.05 instead of 0.20. In total 4 different capillary pressure curves have been tested (see figure 5.9b), ranging from extremely high capillary pressure values (CP1) to extremely low values (CP4). A realistic pressure curve for sandstones is given by CP2 [68] and capillary hysteresis is neglected. The obtained temperature and pressure profiles are plotted in figure 5.9a. It can be observed that, for equal injection rates, more cooling occurs in the reservoir as a capillary pressure curve with higher values is implemented. The enhanced cooling at higher capillary pressure is caused by the higher impairment of the formation by salt precipitation and additional vaporization of water, as a result of a stronger capillary backflow effect. Due to a combination of vaporization of water in the vicinity of the well and displacement of the mobile brine phase by CO<sub>2</sub>, a brine saturation gradient evolves outside the dry-out zone (see figure 5.10 (left)). If the capillary pressure gradient is substantial, backward flow of water will be initiated towards the dry-out zone.

The backflow effect is visualized by the fluxes of CO<sub>2</sub> and brine shown in figure 5.10 (right) for CP1. Here, negative flux indicates migration away from the well while positive flux indicates migration towards the well. In the region behind the dry-out front upto a radius of approximately 40 m, the brine flux is positive and brine is migrating towards the dry-out zone. In the remaining part of the reservoir, the brine is flowing radially outwards along with the non-aqueous CO<sub>2</sub>-rich phase.

Figure 5.11 (left) depicts the salt precipitated in the near wellbore region and the corresponding permeability reduction for the various capillary pressure curves simulated. The solid saturation and the corresponding permeability reduction in the dry-out zone increases as more extreme capillary pressure curves (i.e. for instance CP1) is implemented. Due to the higher capillary pressure gradient that establishes in the reservoir at more extreme capillary pressure curves, a higher amount of water flows towards the well and more water will be evaporated in the vicinity of the well leading to higher salt concentrations. Severe permeability reduction can occur due to the capillary backflow effect and it should be noted that the critical porosity in the Verma-

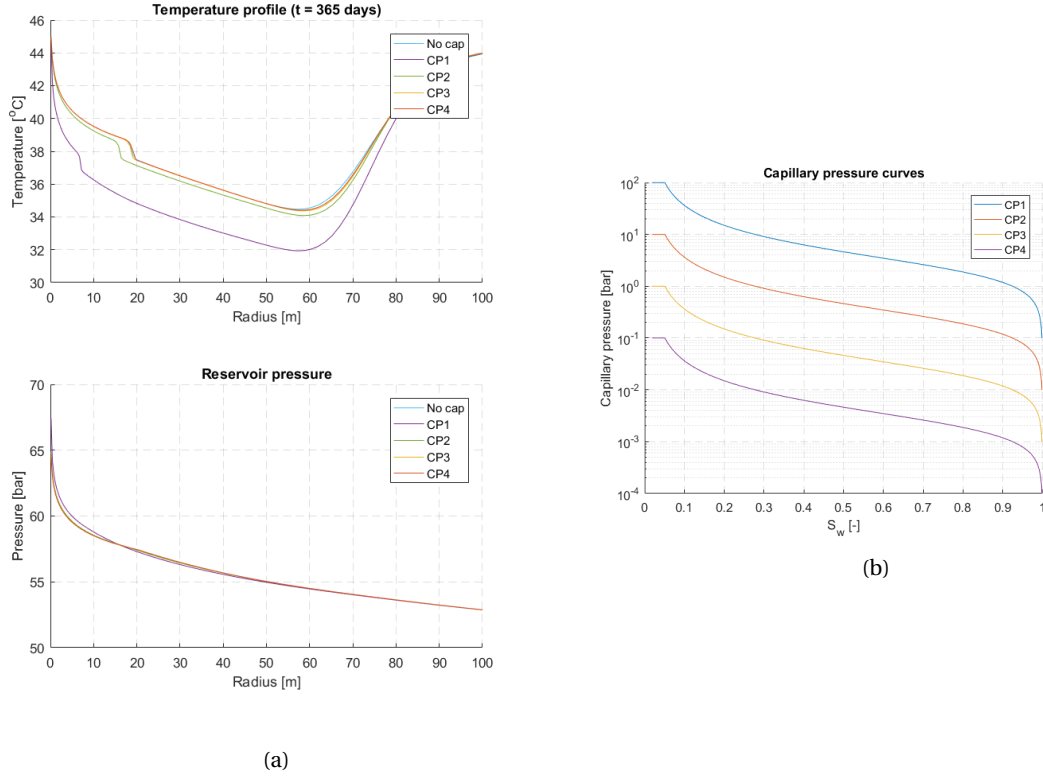


Figure 5.9: (Case 15)(a) Temperature and pressure distribution for different capillary pressures and (b) implemented capillary pressure curves.

Pruess model was changed to 0.6 instead of 0.8 for the simulation case with CP1, to prevent full clogging of the reservoir and termination of the simulation. Hence, the temperature reduction due to cooling shown in figure 5.9a is for the CP1 case slightly underestimated with respect to the other cases.

To determine the importance of the imposed flow rate relative to the capillary pressure for the capillary backflow effect, a displacement ratio and average solid saturation in the dry-out zone have been plotted over the flow rate in figure 5.11 (right) for the realistic capillary pressure curve (CP2), together with the solid saturation for the immobile brine case without capillary pressure. The displacement ratio provides a measure of the brine flux towards the well induced by capillary pressure and the brine flux away from the well. The higher the displacement ratio the more significant the backflow effect. At low flow rates, the capillary backflow becomes more significant due to the low opposing injection induced pressure gradient and lower vaporization rate which provides the brine phase additional time to migrate toward the dry-out zone [68]. Therefore, the highest solid saturation for the mobile brine is observed at the lowest flow rate which has the strongest backflow effect. As the flow rate increases, the backflow effect reduces and vaporization rate increases. At a flow rate of 20 kg/s the average solid saturation for the mobile case intersects the solid saturation line of immobile case. Above flow rates of 20 kg/s the average solid saturation for the mobile case becomes in fact less than for the immobile case. It can therefore be stated that the critical flow rate, defining the flow rate at which capillary backflow effect can be neglected [53], for this particular combination of capillary pressure and simulation input parameters is approximately at 20 kg/s. Hence, at the considered injection rate of 35 kg/s in this sensitivity study, the capillary effect is negligible. But, from a practical perspective, an injection well will not be permanently on stream. In between shut-in and re-start periods the injection rate will drop below the critical injection rate and a stronger capillary backflow effect will occur. The effects of shut-in and re-starts on the capillary backflow effect should be further investigated.

Especially for the higher capillary pressure curves, the salt accumulation close to the well can reach extreme values of solid saturation in the first meter around the well. Roels [53] argued that this phenomena is caused

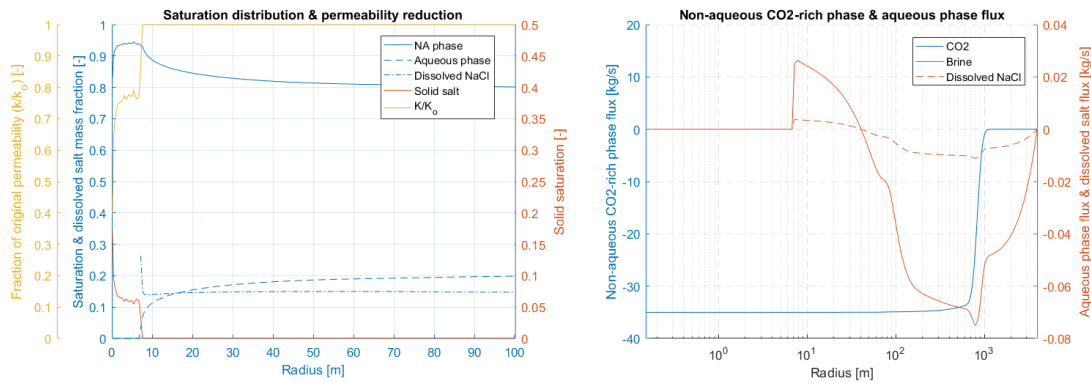


Figure 5.10: (left) Saturation distribution of the non-aqueous phase, aqueous phase, solid saturation and dissolved salt concentration for the simulation case with mobile brine and capillary pressure (CP1) after 1 year of injection; (right) Fluxes of the injected CO<sub>2</sub>, aqueous phase and dissolved salt plotted on a logarithmic scale after 1 year of injection.

by overestimation of the salt precipitation in the numerical module due to the instantaneous local equilibrium assumption in ECO2MG (and GEM) and was not clearly observed in laboratory measurements. The instantaneous local equilibrium assumption overestimates the evaporation of brine, particularly at high injection rates since realistic evaporation rates are several magnitudes smaller. Hence, in reality potential clogging due to salt precipitation is expected further into the reservoir where CO<sub>2</sub> flow velocities are significantly lower and the capillary backflow effect will consequently become more important [53]. Modeling of capillary backflow requires therefore requires a detailed water vaporization kinetics approach instead of instantaneous local equilibrium [53, 66, 74].

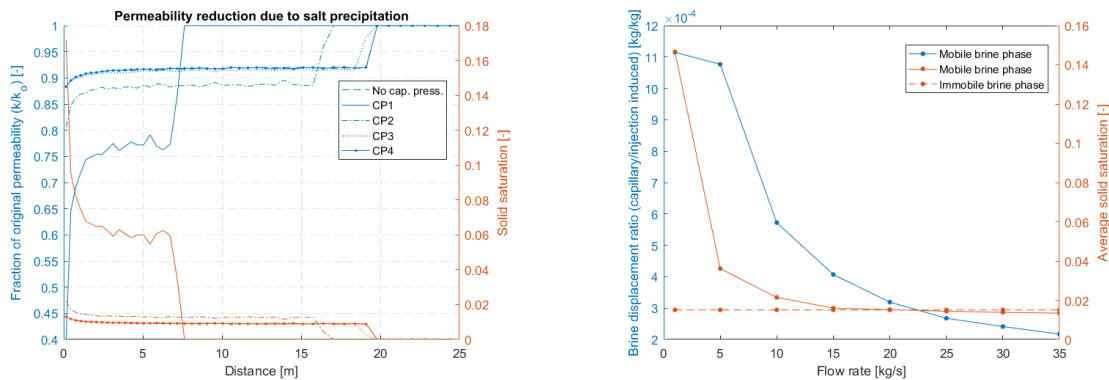


Figure 5.11: (left) Precipitated salt and corresponding permeability reduction in the near wellbore region for different capillary pressure curves after 1 year of injection; (right) Displacement ratio and salt precipitated in the dry-out zone for an immobile and mobile case with capillary pressure (CP2) plotted as function of the flow rate.

### 5.1.13. 1D Sensitivity study results analysis

When analyzing the results of the sensitivity study, it becomes clear that the cooling of the near wellbore region is highly dominated by the JTC and other thermal effects have a less significant contribution. Parameters directly affecting the JT effect, by influencing the JT coefficient of the injected stream or imposed pressure gradient, have the largest impact on the induced cooling during injection. These parameters are the injection rate, injection temperature, reservoir pressure and reservoir permeability. Equally important is the rate of the pressure buildup in reservoir at low initial pressures, being directly proportional to the reservoir size for constant injection rate. The rate of the pressure buildup will determine the time-span in which the CO<sub>2</sub> will be injected in gaseous phase, before transitioning to liquid or supercritical conditions with considerably lower JT coefficients. The faster this transition occurs, the lower the magnitude of the JTC and the less time the reservoir is exposed to the JT induced cooling. Hence, reduction of the reservoir temperature will be consequently less for reservoirs with a high pressure buildup rate.

## 5.2. 2D sensitivity study

The implemented parameters for the 2D simulations are identical to the 1D case, except for the reservoir temperature which is raised to 90°C in favor of the exposure of gravitational effects caused by temperature induced density differences. Three reservoir models with different grades of heterogeneity are defined to study the impact of heterogeneity on the thermophysical effects of CO<sub>2</sub> injection. These models, shown in figure 5.12, are: a homogeneous, 3-layer and heterogeneous model. The three layer model consists of layers with an increasing permeability from top to bottom, separated by impermeable layers. Permeability values in the heterogeneous model have been generated using a Gaussian distribution combined with Dykstra-Parsons coefficients. The minimum and maximum permeability are 40 and 150 mD respectively, with an average value of approximately 100 mD.

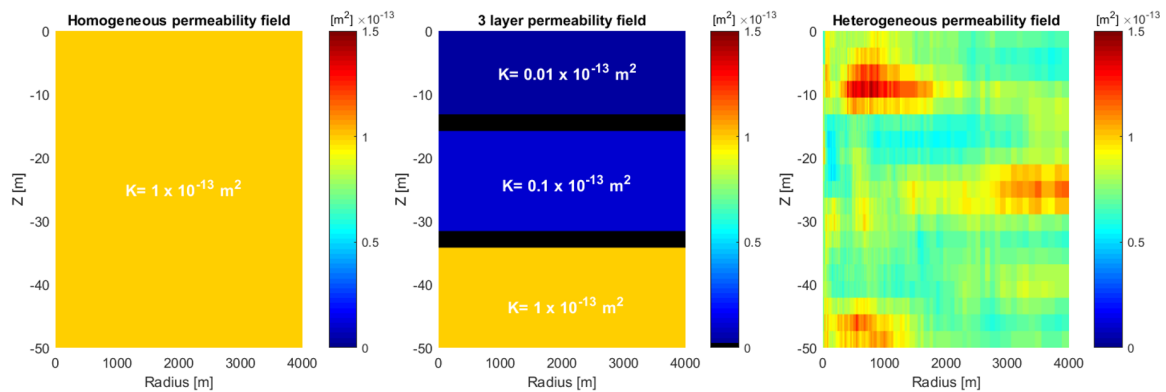


Figure 5.12: Permeability models for the homogeneous (left), 3-layer (middle) and heterogeneous (right) simulation cases. In the 3-layer model the non permeable layers are indicated with black and the permeability distribution from top to bottom is 1 mD, 10 mD and 100 mD respectively.

### 5.2.1. Homogeneous model

In the homogeneous model, the permeability is constant in the entire reservoir, identical to the 1D simulations. However, complementary to the 1D simulation cases, gravitational effects can be captured. The CO<sub>2</sub> is for all simulation equally injected over the entire height of the reservoir. In figure 5.13b, the simulation results for the homogeneous field are shown. For better visualization of the results, only the first 1000 m of the 4000 m reservoir are plotted throughout this section of the report.

Figure 5.13a shows that the cooling front migrates further into the reservoir over the injection time and a slight underride effect appears in the temperature profiles after 5 years. This gravity underride effect is caused by the density difference between the warm CO<sub>2</sub> ahead of the cooling front and the injected cold CO<sub>2</sub>. Due to the density difference the warm CO<sub>2</sub> migrates upwards due to buoyancy forces while the cold CO<sub>2</sub> migrates downward as a consequence of gravity. As a result, the cool and dense CO<sub>2</sub> starts to under ride the warmer and less dense CO<sub>2</sub> at the top of the reservoir. Hence, in the lower part of the domain the cooling front is extended. Cooling induced by the JT effect and water vaporization enhances the density difference and consequently the underride effect. The significance of the underride effect can be defined using a dimensionless gravity number  $N$ . The gravity number is a ratio between the viscous forces, induced by the imposed pressure gradient from the horizontal CO<sub>2</sub> injection, and gravitational forces (i.e.  $\Delta\rho g$ ) and depends on the distance of the density or thermal front the well. A ratio larger than 1 implies that the gravitational forces are dominant over the viscous forces while a ratio smaller than 1 implies that the viscous forces are dominant over the gravitational forces [75]. Close to the well, the viscous forces dominate over the gravitational forces ( $N \ll 1$ ). Hence, after 1 year of injection the temperature profile in figure 5.13a shows a straight thermal front. As the thermal front migrates further into the reservoir the viscous force becomes less dominant and the density difference larger due to the JTC effect. Therefore the underride effect becomes more exposed over time.

The underride effect alters the CO<sub>2</sub> flow and subsequently the temperature and pressure distribution in the reservoir. However, the evaporation profile and distribution of the salt precipitation is not largely affected as figure 5.13b indicates; a relatively uniformly distributed solid is observed. This is caused by the fact that the dry-out zone is still close to the well where the viscous forces dominate over the gravitational forces.

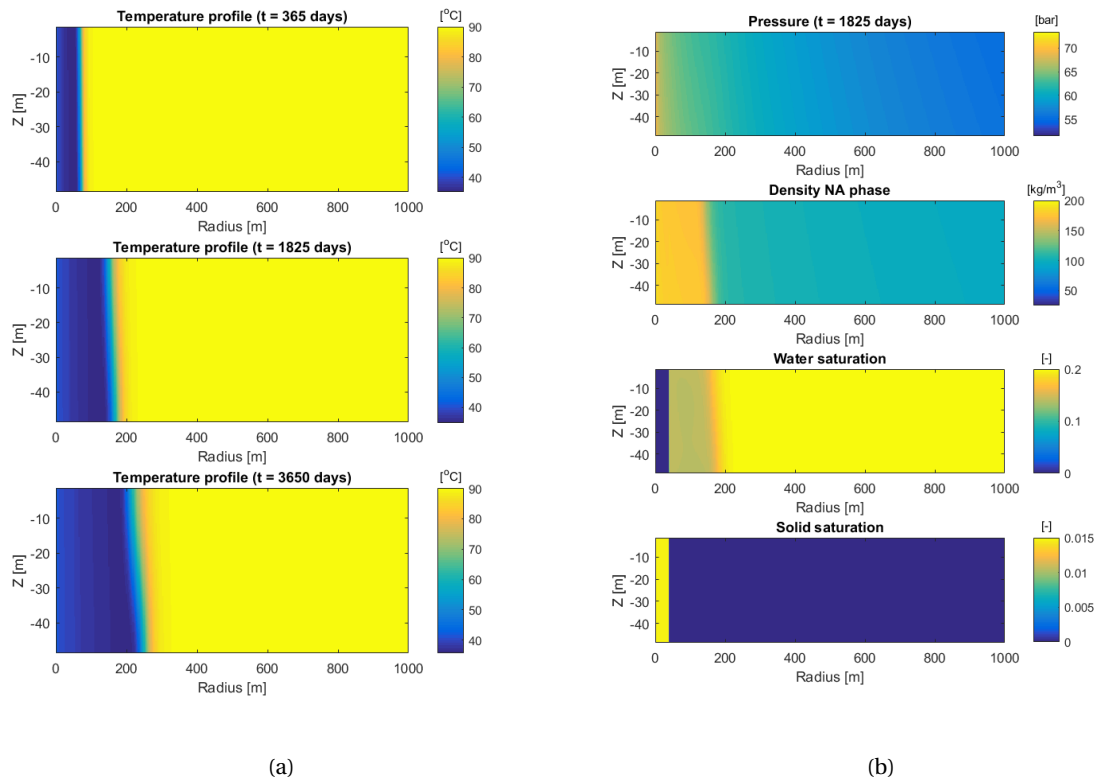


Figure 5.13: (Case 16)(a) 2D temperature profiles for a homogeneous reservoir after 1, 5 and 10 years of injection and (b) pressure, density, water saturation and solid saturation profiles after 5 years of injection

Vertical permeability has an impact on the the underride effect. A lower value reduces the downward migration of the denser CO<sub>2</sub> by gravitational forces. The  $K_v/K_h$  parameter indicates the ratio between the vertical and horizontal permeability. Accordingly, as shown in figure 5.14, the underride effect is less for lower  $K_v/K_h$  ratios. In addition, gravity underride effect will become more exposed as the pressure in the reservoir builds up over the injection time. The density contrast between the CO<sub>2</sub> at the location of the minimum temperature within the cooling zone and the CO<sub>2</sub> at initial temperature behind the thermal front is larger for higher pressures. This consequently leads to a stronger underride effect.

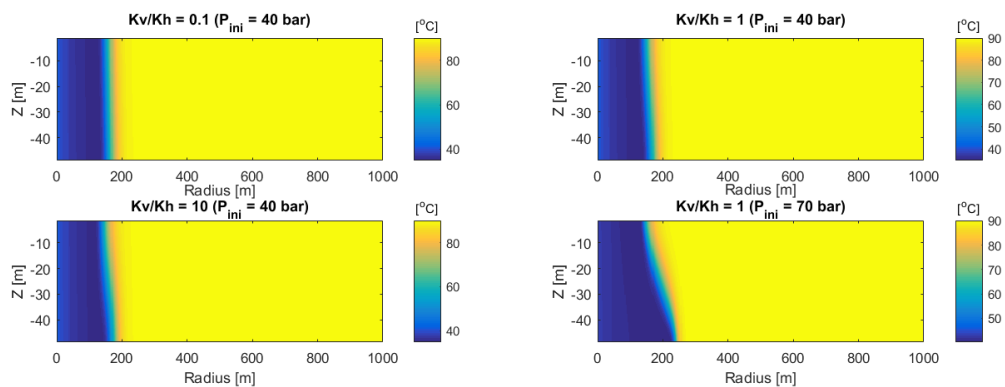


Figure 5.14: (Case 17) Temperature profiles for different  $K_v/K_h$  ratios after 5 years of injection at initial reservoir pressures of 40 and 70 bar.

### Heat exchange with over- and underburden

In the formerly shown simulation results, heat exchange with the reservoir confining formations was neglected. As discussed in paragraph 2.3.2, the confining formations, being at initial reservoir temperature, affect the temperature distribution along the depth of the reservoir. The under- and overburden act as heat source, transferring heat into the reservoir through conduction. In figure 5.15, the temperature profiles for a simulation with and without heat exchange are depicted.

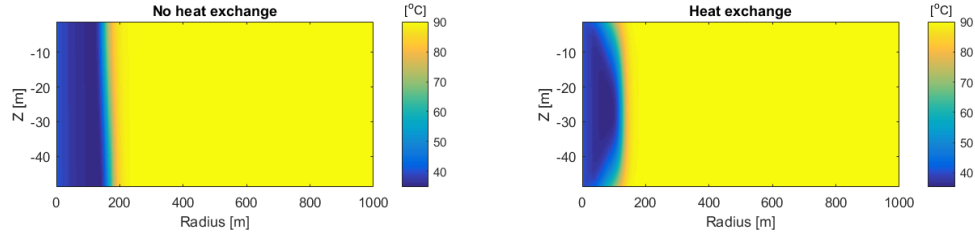


Figure 5.15: (Case 18) Temperature profiles for simulations with (left) and without (right) heat exchange with the confining over- and underburden formations after 5 years of injection.

The temperature profile of the simulation in which the heat exchange with confining layers is enabled, strongly deviates from the temperature profile obtained in the simulation without heat exchange. At the top and bottom of the reservoir, the magnitude of cooling and extent of the thermal front are significantly less compared to the middle section of the reservoir. As a result, the underdrive effect present in the simulation without heat exchange is nearly absent. The extent to which the provided heat affects the temperature profile in the reservoir, depends on the combination of the formation thermal diffusivity and the height of the injection column. The influence on the temperature profile would be highest for reservoirs with a low thickness and high thermal diffusivity, corresponding to the implemented parameters in this sensitivity study. As a consequence of the provided heat from the adjacent formations and undisturbed section of the reservoir, the cooled reservoir will gradually heat up to the initial reservoir temperature after the injection of CO<sub>2</sub> is finished.

### 5.2.2. 3-layer model

To realistically model the distribution of the injected CO<sub>2</sub>, according to the injectivity of the formation in absence of a wellbore model in ECO2MG, the vertical permeability at the first cell where the CO<sub>2</sub> source is located, is set to an infinitely high value. This ensures that the injection behavior is mimicking the behavior of a wellbore model. In the 3-layer model, the injectivity of CO<sub>2</sub> increases per layer from top to bottom due to the increase in permeability, except for the impermeable layers in between (see figure 5.16 (left)). Because of the difference in permeability, with constant rate injection, a higher injection pressure is required to inject the same amount of CO<sub>2</sub> in the top layer compared to the middle and bottom layer. Since the pressure at the well location is fairly constant over the height of the reservoir, most CO<sub>2</sub> is injected in the layer in the lowest layer while least CO<sub>2</sub> is injected in the upper layer, as shown by the extends of the mixing front in figure 5.17 (left bottom). The mixing front in the upper layer is at roughly 350 m while the front in the lowest layer is already at 2250 m. Moreover, because a higher amount of dry CO<sub>2</sub> is injected in the lower layer, more water evaporates which increases the extent of the dry-out region and associated salt precipitation.

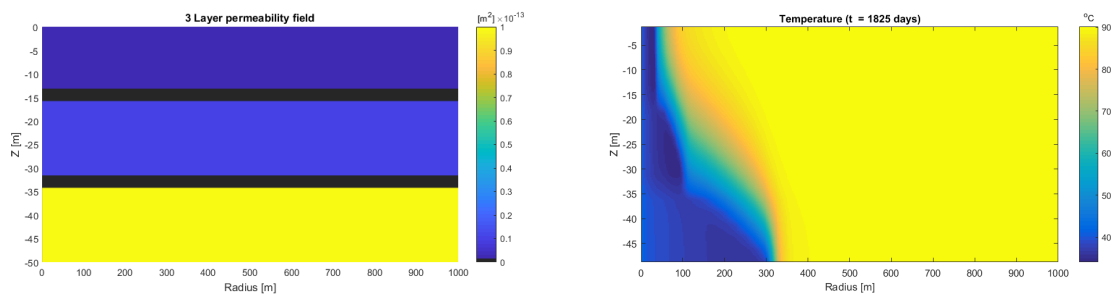


Figure 5.16: (Case 19)(a) Permeability field for the 3-layered system with a permeability distribution from top to bottom of 1 mD, 10 mD and 100 mD respectively and (b) corresponding temperature profile after 5 years of injection.

Because of the unequal injection of CO<sub>2</sub> over the layers, the thermal front provided in figure 5.16 (right) has advanced further into the reservoir in the lowest layer compared to the other layers. The enclosed impermeable layers are approximately at the same temperature as the surrounding permeable layers (i.e. where CO<sub>2</sub> flow occurs) due to the heat conduction. The difference in minimum temperature reached after 5 years of injection between the layers is less than 2°C, where the lowest minimum temperature is observed in the upper layer and highest in the lower layer. This discrepancy in minimum temperature, indicating that more cooling occurs in the upper layer, is caused by a combination of the difference in pressure drop over the near wellbore region in each layers and heat exchange with the surroundings. Note that heat exchange only happens between the reservoir layers; heat exchange with the confining layers is not enabled. The pressure drop is highest in the upper layer, causing the largest JTC, and becomes less for middle and lower layer. In addition, the simultaneously occurring heat exchange between layers dampens the temperature reduction in the middle and lower layers and enlarges the discrepancy in temperature reduction with respect to the upper layer. Since the cooling fronts migrate faster in the middle and lower layer, the temperature profile in these layers are affected by the considerable heat exchange with the upper layer, which is at the location of the thermal front still at initial reservoir temperature.

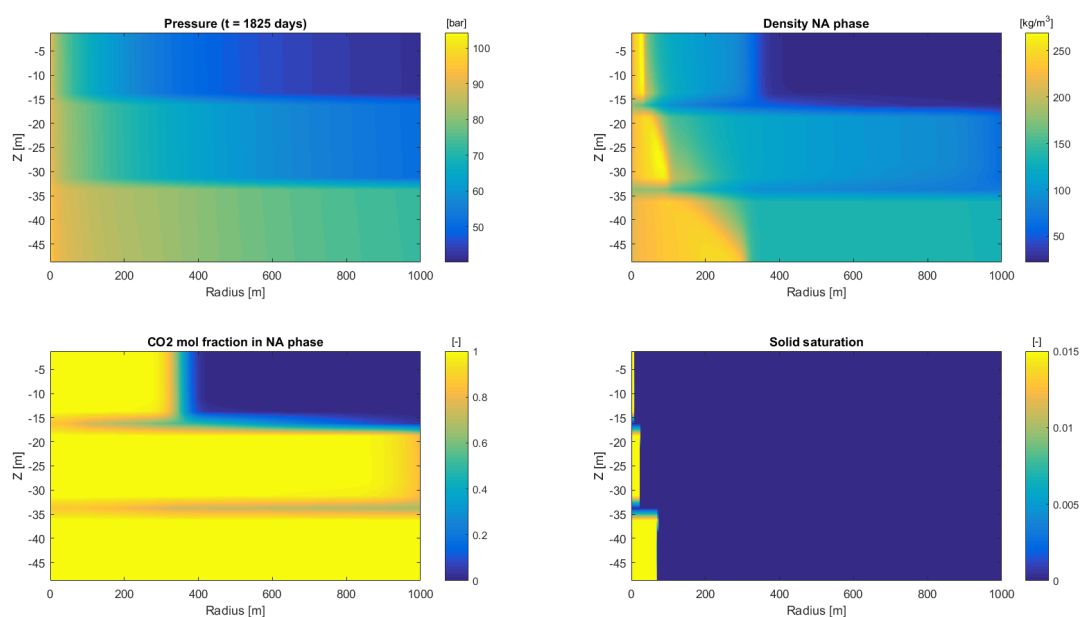


Figure 5.17: Pressure, density of the NA phase, CO<sub>2</sub> mole fraction in the NA phase and solid saturation profile for the 3-layer model after 5 years of injection.

### 5.2.3. Heterogeneous model

The heterogeneity in the considered reservoir, consisting of several randomly generated high and low permeable zones, significantly alters the CO<sub>2</sub> flow patterns and therefore the spatial distribution of the induced physical effects in the reservoir and near wellbore region. In figure 5.18, the permeability field along with the temperature profile upon which the CO<sub>2</sub> mass flux vectors and corresponding streamlines are plotted. These streamlines indicate the direction flow direction and the magnitude of the mass flux; the closer these streamlines the higher the flux. As visible, the flow pattern is closely correlated to the heterogeneous structure in the reservoir. In the close vicinity of the well, the direction of the CO<sub>2</sub> mass fluxes are mainly dominated by the horizontal injection forces and local heterogeneities. For instance, the injected CO<sub>2</sub> tends to bypass the low permeable zone located at a radius of roughly 150 m and depth of -20 m. As a result, the JTC is less in this low permeable part of the reservoir. The thermal front is therefore also not as far advanced in this region compared to the higher permeability regions above and below. Accordingly, the dry-out region indicated by the aqueous phase saturation in figure 5.19 and the corresponding solid saturation profile is affected in a similar manner and follows the contours of the permeability distribution. Less water vaporization occurs in the low permeability regions due to the lower CO<sub>2</sub> mass flux locally and consequently less salt precipitates.

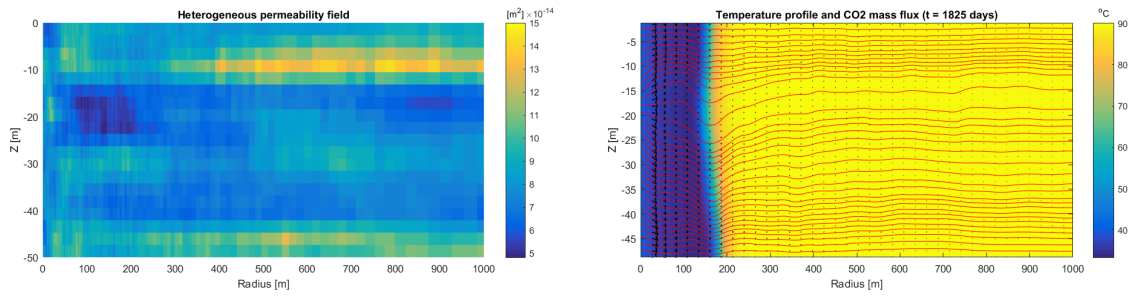


Figure 5.18: (Case 20)(a) Heterogeneous permeability field and (b) temperature profile including  $\text{CO}_2$  mass flux vectors (black arrows) and streamlines (red lines) after 5 year of injection.

Over time, as a higher volume of  $\text{CO}_2$  is injected and the thermal front has advanced further into the reservoir, the influence of injection forces reduces and the downward migration of the cold  $\text{CO}_2$  due to gravity becomes more exposed. This downward migration of  $\text{CO}_2$  is shown by the downward deflection in the stream lines at the location of the thermal front. However, in contrast to the homogeneous model, the underride effect is affected by the local variations in permeability.

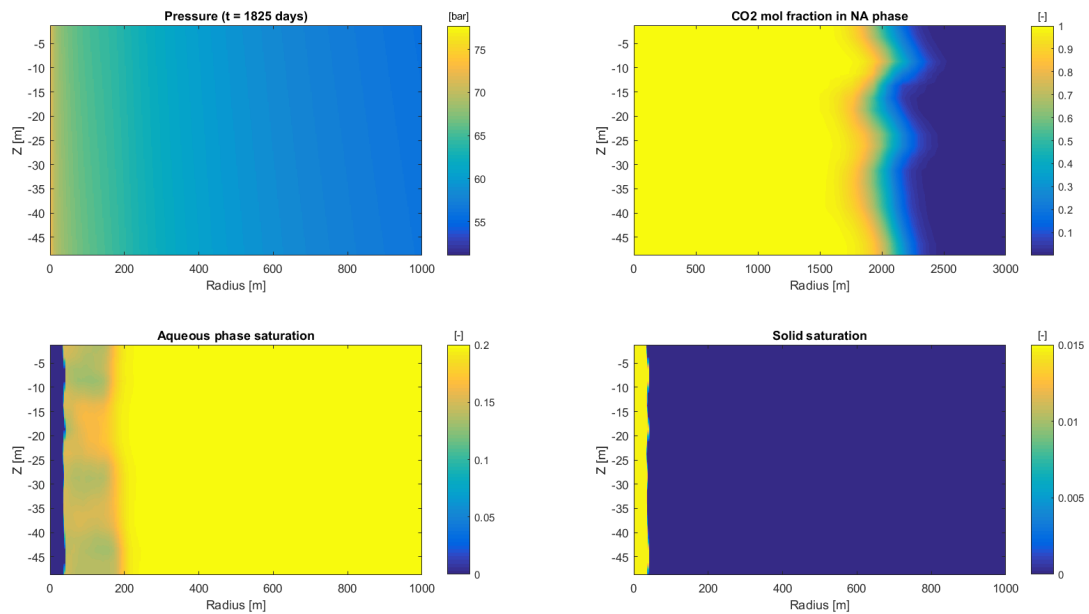


Figure 5.19: Pressure, composition, aqueous phase saturation and solid saturation profiles for the heterogeneous model after 5 years of injection. Note the extended plot radius for the composition profile.

Furthermore, in the 3-layer model it was shown that a straight mixing front develops between the  $\text{CO}_2$  and  $\text{CH}_4$  due to the favorable mobility ratio. The mixing front in this heterogeneous model shows some irregularities, attributed to the heterogeneity (see figure 5.19). Nevertheless, this irregular front does not affect the physical effects occurring in the near wellbore region.

### 5.3. Influence of dry-out and salt precipitation on effective permeability

Vaporization during CO<sub>2</sub> injection enhances the relative permeability of CO<sub>2</sub> by reducing the aqueous phase saturation, while on the other hand, the associated precipitation of salt causes a reduction of the absolute permeability of the formation. As a result, the dry-out process simultaneously enhances and reduces the effective permeability and thus affects the injectivity of CO<sub>2</sub> into the formation. Effective permeability of CO<sub>2</sub> in the reservoir is defined as

$$K_{eff,\alpha} = k_{r,\alpha} \cdot \psi \cdot K_0 \quad (5.2)$$

where  $K_{eff,\alpha}$  is the effective phase permeability,  $K_0$  is the initial rock permeability and  $\psi$  is the permeability reduction factor by salt precipitation (i.e.  $K/K_0$ ). In this paragraph simulations are conducted in ECO2MG, for an immobile phase, to examine which of the aforementioned effects is most dominant and whether the injectivity increases or decreases.

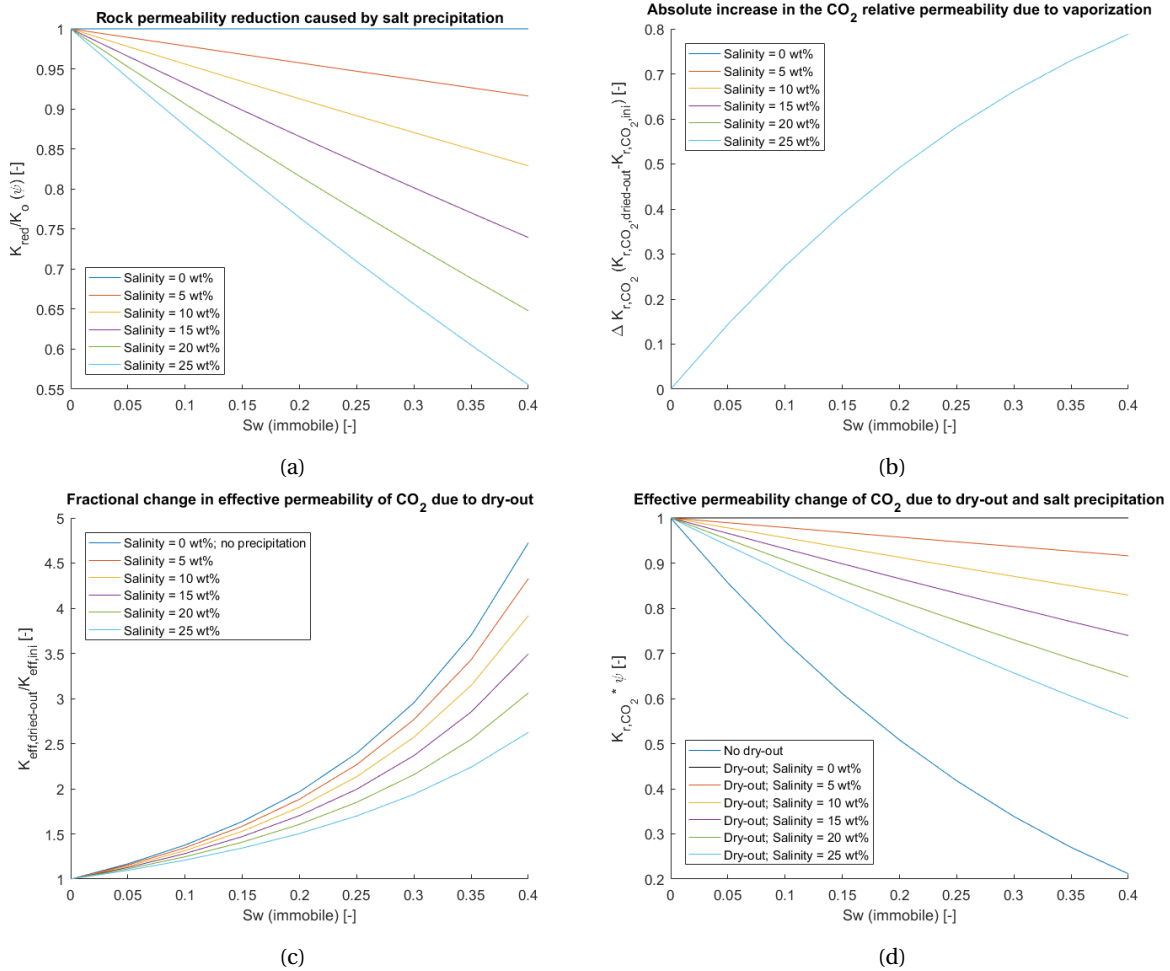


Figure 5.20: (a) Permeability reduction due to salt precipitation as a function of water saturation at different salinities (with  $\phi_r = \Gamma = 0.8$ ) and assuming immobile brine; (b) The absolute increase in relative permeability caused by water vaporization with respect to the initial relative permeability in presence of a brine phase (i.e.  $K_{r,CO_2,dried-out} - K_{r,CO_2,ini}$ ); (c) Fractional change in effective permeability as a consequence of relative permeability increase and absolute permeability decrease; (d) Effective permeability change between the initial situation (without dry-out and salt precipitation indicated by the blue no dry-out line) and after dry-out and salt precipitation for different water saturations and salinities.

In the determination of the increase in relative permeability during the dry-out and precipitation process, active saturations are used. Active saturation ( $S_{\beta,\alpha}$ ) describes the saturation of a non-solid phase  $\beta$  in presence of a solid phase and reads as [68]

$$S_{\beta,\alpha} = \frac{S_\beta}{1 - S_s} \quad (5.3)$$

Reduction of the permeability due to salt precipitation and the increase in relative permeability over the initial water saturation for different salinity values are shown in figure 5.20a and 5.20b respectively. Salinity values upto 25 wt% are tested, which is close to the salt solubility limit (i.e. 26.75 wt% at the initial reservoir temperature). The permeability reduction increases with increasing salinity, while the increase of relative permeability is equal for all salinity values due to usage of active saturations. The effective permeability with dry-out and precipitation can be divided by the effective permeability without dry-out to provide a fractional change (see figure 5.20c) or plotted as absolute change (see figure 5.20d). From the figures it can be concluded that the effective permeability increases due to dry-out. Relative permeability increase due to vaporization of the brine is dominant over the absolute permeability reduction as a result of salt precipitation, for the considered water saturation and permeability reduction parameters. Thus, the injectivity increases due to dry-out; this enhancement of injectivity becomes larger for higher initial water saturations. Similar results are obtained and conclusions can be drawn for the influence of the dry-out process on the injectivity in case of implementation of a mobile brine phase where the capillary pressure is taken into account. The obtained changes in effective permeability due to dry-out are highly dependent on the permeability reduction parameters used in the permeability reduction model. However, to obtain a negative impact on the effective permeability due to dry-out and salt precipitation, for the water saturation range considered, exceptionally high critical porosities with values above 0.95 are required.

## 5.4. Simulator comparison

### 5.4.1. Comparison of JTC between analytical solution and numerical models

The steady-state analytical solution by Mathias et al. [34], can be compared to the output of the numerical simulators (i.e. GEM and ECO2MG). In contrast to the latter, the simplistic analytical solution does not account for thermal effects other than the JT effect. Hence, vaporization and dissolution are not included. To provide a sound comparison between the analytical and numerical solutions, the water saturation is set to a value of 0.0001, which minimizes the thermal contributions of vaporization and dissolution in ECO2MG and GEM. Figure 5.21 shows the obtained temperature profiles for the input parameters given in table 5.1.

Table 5.1: Simulation input parameters for the analytical model, ECO2MG and GEM.

Parameter	Value (unit)	Parameter	Value (unit)
Porosity ( $\phi$ )	0.12 (-)	Injection temperature ( $T_{inj}$ )	45 ( $^{\circ}$ C)
Permeability ( $K$ )	100 (mD)	Reservoir temperature ( $T_{res}$ )	45 ( $^{\circ}$ C)
Reservoir radius ( $r$ )	4000 (m)	Initial pressure ( $P_{ini}$ )	40 (bar)
Reservoir height ( $h$ )	50 (m)	Joule-Thomson coefficient ( $\mu_{jt}$ )	0.92 ( $^{\circ}$ C/bar)
Injection rate ( $Q_{inj}$ )	20 (kg/s)	Aqueous phase saturation ( $S_{aq}$ )	0.0001 (-)

The figure indicates that the analytical, GEM and ECO2MG solutions are in close correspondence for a wellbore radius of 0.15 m in the analytical solution. The minimum temperature obtained in the GEM simulation slightly deviates from the value obtained by ECO2MG. In GEM, the JT effect is slightly lower compared to ECO2MG due to difference in the pressure behavior of the grid cells adjacent to the well location, which will be discussed in detail in the following paragraph. This discrepancy in pressure is particularly important at early injection times. Hence, the difference in minimum temperature reached reduces from 0.15 $^{\circ}$ C at 30 days after injection to 0.03 $^{\circ}$ C after two years of injection. Nonetheless, the location of the minimum temperatures in temperature profiles of ECO2MG and GEM are in close agreement.

When comparing the analytical solution to the numerical simulation results, it can be observed that the temperature profile of the analytical solution have marginally lower minimum temperatures (approximately 0.02 to 0.04 $^{\circ}$ C). However, the location of the minimum temperature is slightly further extended into the reservoir. This difference enhances over time and is caused by the constant thermophysical properties (e.g. density and viscosity) in the analytical solution. Due to injection and the JT effect, the pressure and temperature changes in the near wellbore region. This subsequently leads to changes in the thermophysical properties. The predefined constant thermophysical properties in the analytical solution consequently become less accurate over time. As the implemented flow rate is increased, the variation in pressure and temperature conditions in the vicinity of the well increases and leads to a slightly higher discrepancy between the analytical and numerical solution. At a flow rate of 35 kg/s the observed discrepancy with respect to the ECO2MG solution was in the

range of 0.65°C at early injection times to 1°C after 2 years of injection. Approximately the same discrepancy was obtained for implementation of a matching wellbore radius with the numerical solution (i.e. 0.3 m). In case the water saturation is set to 0.2 in the analytical model and numerical model, enabling other thermal effects and salt precipitation in the numerical simulation, the discrepancy in minimum temperature increases to more than 4°C. Hence, the analytical solution is therefore only useful to quickly examine the cooling induced by solely the JT effect.

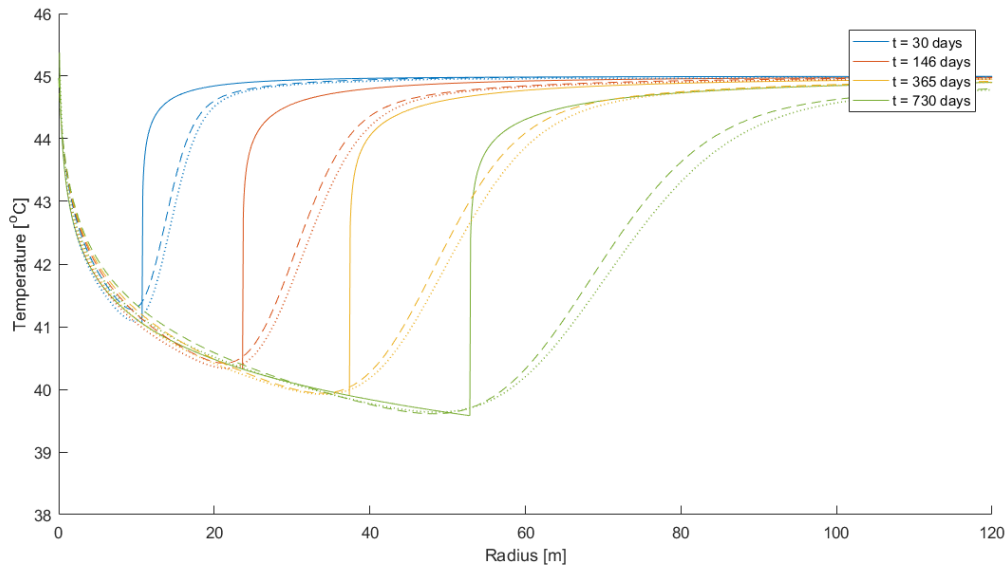


Figure 5.21: (Case 21) Comparison of the analytical solution (solid), ECO2MG (dashed) and GEM (dotted).

**5.4.2. Comparison of ECO2MG and GEM simulation results**

A second comparison study is performed between both numerical simulators to determine deviations between the calculated output for an identical test case in which all physical effects are included, i.e. JT effect, H<sub>2</sub>O vaporization, CO<sub>2</sub> dissolution, salt precipitation and the corresponding reduction of the permeability. The parameters, reservoir domain and grid spacing used in this test case are equivalent to the 1D sensitivity study. Due to absence of a wellbore model in ECO2MG, the first grid cell in the ECO2MG model is treated as the wellbore and is given the same radius as the wellbore in GEM. To match the permeability reduction due to salt precipitation calculated by the enhanced Verma-Pruess model in ECO2MG, the resistance factor exponent was adjusted in the Carman-Kozeny model in GEM.

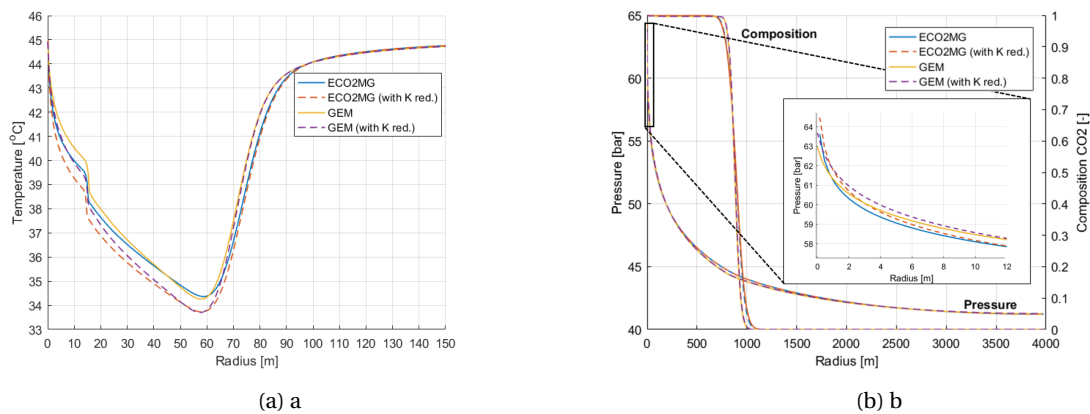


Figure 5.22: (Case 22)(a) Temperature profiles and (b) pressure and composition profiles obtained from ECO2MG and GEM with and without permeability reduction after 1 year of injection, with equivalent model geometries and simulation parameters.

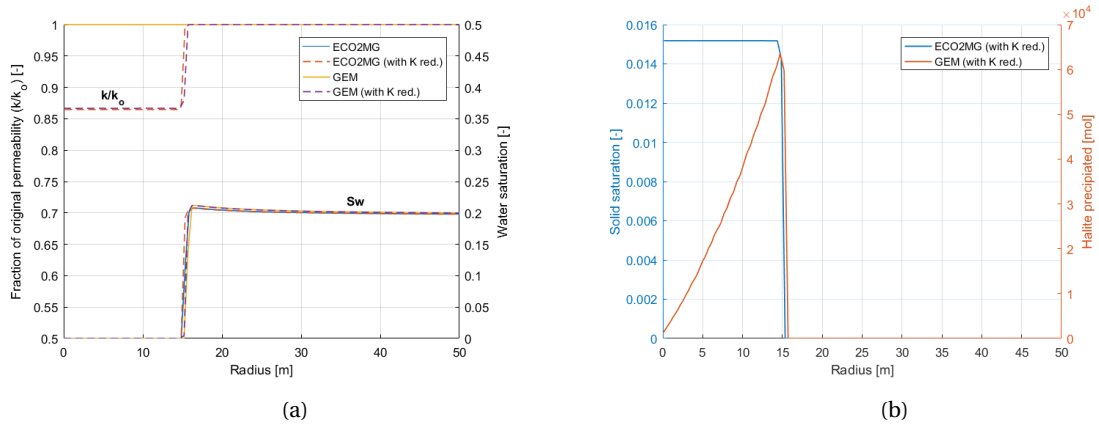


Figure 5.23: (a) Permeability reduction and (b) aqueous phase saturation simulated obtained from ECO2MG and GEM after 1 year of injection, with equivalent model geometries and simulation parameters.

In figure 5.22, the temperature, composition and pressure profiles after 1 year of injection are depicted. The temperature profiles indicate that the minimum temperature reached in the reservoir and the extent of the thermal front between ECO2MG and GEM are in close correspondence in both simulations with and without permeability reduction enabled. Nonetheless, when the temperature curves are thoroughly analyzed it becomes clear that the temperature profiles from both simulators diverge from the injection point towards the end of the dry-out zone (at  $\pm 15$  m). The radii of the dry-out zones shown in figure 5.23a are almost identical for both simulators. But, at the dry-out front the temperature difference is approximately  $0.5^\circ\text{C}$ , indicating that less JTC occurs in the GEM simulation. This is caused by the difference in pressure gradient between both simulators within the dry-out region. Since the pressure gradient in this part of the domain is larger in the ECO2MG simulation compared to GEM, more JTC cooling occurs in this region in ECO2MG. The temperature drop induced by the vaporization of water is slightly larger for GEM (i.e. approximately  $0.1^\circ\text{C}$ ), slightly lowering the discrepancy. Further into the domain, after the dry-out zone, the pressure gradient in ECO2MG reduces with respect to pressure curve in GEM and therefore the curves start to converge and overlap each other again.

Figure 5.23b shows the distribution of the precipitated salt. In both simulators the salt precipitation in the dry-out is constant because the brine phase is assumed to be immobile. However, the output of the precipitated salt is given in moles in GEM while in ECO2MG it is provided as saturation value. Since a radial grid with logarithmically increasing cell radii is implemented, the cell area successively increases further away from the well. Therefore, the amount of precipitated NaCl expressed in moles in GEM step-by-step increases.

It can be stated that although the simulators utilize different phase partitioning and EOS models, the magnitudes of the modeled thermophysical effects are very similar and the output accurately matches in this particular test case.

# 6

## Near wellbore cooling management

To mitigate potential reservoir impairments during the CO<sub>2</sub> injection process, it is essential that the reservoir conditions are managed accordingly. Injection rate, pressure, temperature and CO<sub>2</sub> composition are the key parameters to control the occurring effects and conditions down hole. As the results in the sensitivity study indicated, the reservoir cooling can reach more than 15°C with respect to the initial CO<sub>2</sub> injection temperature. If CO<sub>2</sub> is injected at low temperatures potential risks of hydrate formation and freezing of the residual water exist.

The temperature at which the CO<sub>2</sub> enters the reservoir, deviates from the injection temperature at the surface. During transport through the injection well several mechanisms as frictional energy losses, gravitational effects, conductive heat exchange between surrounding formations and the injected CO<sub>2</sub> and JT effects due to compression and expansion of the CO<sub>2</sub> alter the CO<sub>2</sub> temperature [23]. Therefore, the temperature behavior of the CO<sub>2</sub> stream from surface to bottom hole is complex and requires detailed modeling. However, temperature modeling inside the wellbore is outside the scope of this research.

In CO<sub>2</sub> storage operations in offshore depleted gas fields, the arrival temperature of the CO<sub>2</sub> stream is approximately between 4 and 10°C depending on the seawater temperature. Recent modeling studies on the temperature behavior along the injection well indicated that arrival temperature of CO<sub>2</sub> temperature at the bottom of the well is in the range of 20 to 30°C for a well depth 3200 m, imposed rate of approximately 35 kg/s and low initial reservoir pressures [76] (see Appendix E figure E.1). It should be noted that in these cases the cold CO<sub>2</sub> arriving at the platform is directly injected without preheating. As CO<sub>2</sub> enters the reservoir at these low temperatures and high injection rates, significant cooling will occur in the near wellbore region which could lead to hazardous situations.

Presence of contaminants in the CO<sub>2</sub> stream alter the thermophysical and dynamic behavior. This causes changes, in a positive and negative way, to effects happening in the near wellbore regions as vaporization, dissolution and JTC with respect to pure CO<sub>2</sub>. Hence, the CO<sub>2</sub> stream composition should be studied and managed accordingly. In addition, injection of impure CO<sub>2</sub> can be economically attractive because less purification of the CO<sub>2</sub> streams is required, reducing the costs of CCS significantly. However, injection of impurities in the reservoir can also induce undesirable chemical reactions, but that is outside the scope of this research.

Besides mitigation of hydrate formation by modifying the operational injection conditions or CO<sub>2</sub> stream composition, also hydrate inhibitors as methanol, ethylene glycol and diethylene glycol can be used to prevent or remediate hydrate formation in the reservoir [77, 78]. Usage of additives can be beneficial if the hydrate formation is infrequent or subject to a small region in the reservoir but consequently affects the CO<sub>2</sub> injection operation in terms of downtime and costs [78].

## 6.1. Injection scenarios

Operational injection parameters, i.e. injection temperature and rate (or injection pressure instead), can be modified to control the reservoir conditions and magnitude of the occurring thermal effects in the near wellbore region. At an injection rate of 35 kg/s and fixed injection temperature of 20°C, conditions in the reservoir within the hydrate formation zone are rapidly reached at early injection stages, when the reservoir pressure is close to initial pressure. Therefore, injection scenarios are defined in which modifications of injection parameters are applied during the injection period based on the reservoir pressure in order to reduce the reservoir cooling and prevent dangerous conditions.

For the injection scenarios a reservoir with a radius of 2000 m is implemented instead of the 4000 m used in the sensitivity study to accelerate the pressure buildup and reduce computational time. In addition, the reservoir pressure and fixed injection temperature are set to extreme values of 20 bar and 20°C respectively. Changes of the injection temperature due to different flow rates caused by effects in the wellbore are not taken into account. Besides, the presented scenarios in this paragraph are only manually optimized.

### 6.1.1. Variable injection rate with fixed injection temperature

The injection rate and cumulative volume injected over time are shown in figure 6.1a for the base case scenario with a constant flow rate (dashed lines) and scenario with modified injection rate (solid lines). In both cases the CO<sub>2</sub> is injected at a fixed temperature of 20°C. At early injection time, when the pressure is close to initial conditions corresponding to a large JT coefficient of the injected CO<sub>2</sub> stream, a low rate is applied in the modified injection scenario. This in order to reduce the induced the pressure gradient over near wellbore region and to regulate the cooling. As the reservoir pressure increases, the JT coefficient of the injected stream decreases and a higher flow rate can be implemented without reaching hazardous conditions.

In figure 6.2, the minimum temperature in the reservoir and corresponding pressure are plotted for the base case scenario (blue), injection scenario with modified injection rate (red) and injection scenario with modified injection temperature (yellow), of which the latter will be treated in the next paragraph. The connected dots represent consecutive time steps in months. As visible, for the base case shown in figure 6.2 by the dashed lines, the temperature in the reservoir reduces fast during injection. The hydrate formation conditions are quickly reached, terminating the injection process. However, for the scenario with adjusted rates, the conditions remain outside of the the formation zone. Hence, by gradually increasing flow rate based on the prevailing reservoir pressure, the cooling can be adequately controlled.

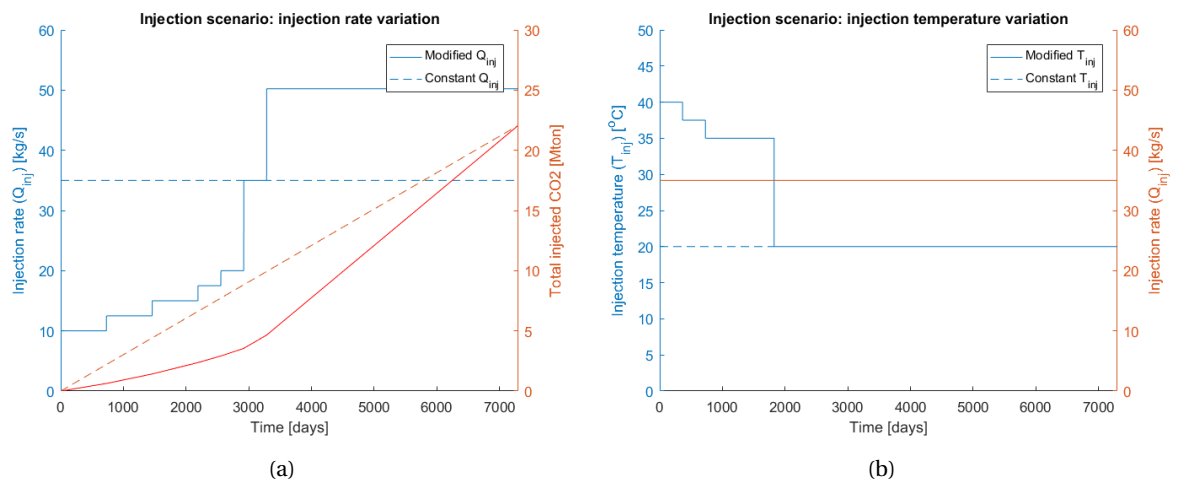


Figure 6.1: (Case 23)(a) Injection rate plotted over time for the variable injection rate scenario (solid lines) and base case scenario with fixed injection rate (dashed lines) and (b) Injection temperature for the variable injection temperature scenario (solid lines) and base case with fixed injection temperature (dashed lines).

### 6.1.2. Variable injection temperature with fixed flow rate

An alternative option to mitigate potential risky situations in the reservoir, while maintaining a fixed injection rate, is increasing the CO<sub>2</sub> injection temperature by heating the supplied CO<sub>2</sub> before injection. Heating of CO<sub>2</sub> is however not preferred due to economical reasons.

In figure 6.1b, the injection temperature is shown for the modified temperature injection scenario (solid) along with the base case scenario (dashed) having a fixed injection temperature 20°C. Both scenarios have a fixed injection rate. At the beginning of injection, the CO<sub>2</sub> is heated in the modified injection temperature scenario, to reduce the JT coefficient of the CO<sub>2</sub> stream and consequently lower the JTC effect. The yellow dots in figure 6.2 indicate that the temperature maintains outside the hydrate formation zone throughout the injection period.

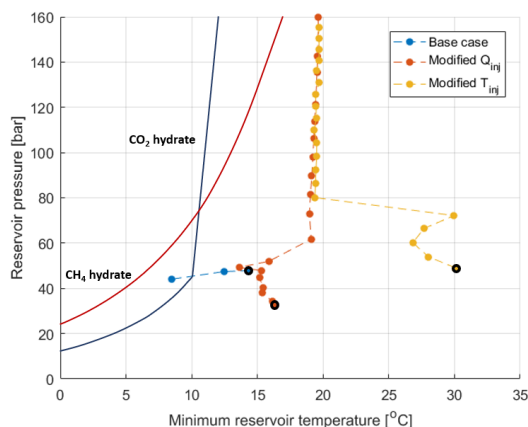


Figure 6.2: Minimum reservoir temperature and corresponding pressure for the 3 injection scenarios considered, in which the dots represent the pressure and temperature condition at consecutive time steps of one month (the first month is indicated by the black outline) and the solid lines mark the outer boundaries of the hydrate formation region.

## 6.2. Impurities in CO<sub>2</sub> injection stream

In the previously conducted simulations, an injected CO<sub>2</sub> stream consisting of 100% CO<sub>2</sub> was assumed. However, in reality the injected CO<sub>2</sub> stream contains impurities and is not completely pure. The type and amount of impurities present in the CO<sub>2</sub> stream depend on the source and purification process [79]. Common impurities found in CO<sub>2</sub> injection streams are N<sub>2</sub>, O<sub>2</sub>, Ar, SO<sub>2</sub>, H<sub>2</sub>S, CH<sub>4</sub> and H<sub>2</sub>. Impurities in the injected CO<sub>2</sub> stream alter the PVT and VLE characteristics of the mixture. Presence of impurities in the reservoir will therefore lead to changes in pressure response of the reservoir during injection and near wellbore cooling with respect to pure CO<sub>2</sub> injection.

Prior research by ZiabakhshGanji [25] on contaminants indicate that, the change of the specific heat capacity of the mixture due to presence of a contaminant has a dominant impact on the extent of the cooling front (at constant injection rate) and this extent is not largely affected by changes in density or the JT coefficient. On the other hand, the magnitude of JTC and the corresponding minimum temperature reached in the reservoir is primarily dominated by the corresponding JT coefficient but also influenced by specific heat capacity of the mixture and density. The dependency of the cooling effect on the thermophysical and dynamic properties of the mixture is therefore less straightforward than for pure CO<sub>2</sub> injection [25].

In figure 6.3, the JT coefficient and specific heat capacity of individual components are plotted as function of pressure. The figure shows significant differences between magnitudes of these characteristic properties. The majority of the components have a considerable lower JT coefficient than pure CO<sub>2</sub>. JT coefficients of H<sub>2</sub> and SO<sub>2</sub> are even negative in the current pressure range, implying that these components will heat up during expansion. Also the specific heat capacities are generally lower for the impurities.

The changes in density and enthalpy for different CO<sub>2</sub>-impurity mixtures with respect to pure CO<sub>2</sub> are given in figure 6.4. The majority of components reduce the enthalpy of the mixture but also the density of the mixture

as the impurity mole fraction increases. Most obvious are the significant reduction of enthalpy and density for the mixture with H<sub>2</sub>. In addition, presence of Ar leads to a notable increase in enthalpy while SO<sub>2</sub> strongly increases the density.

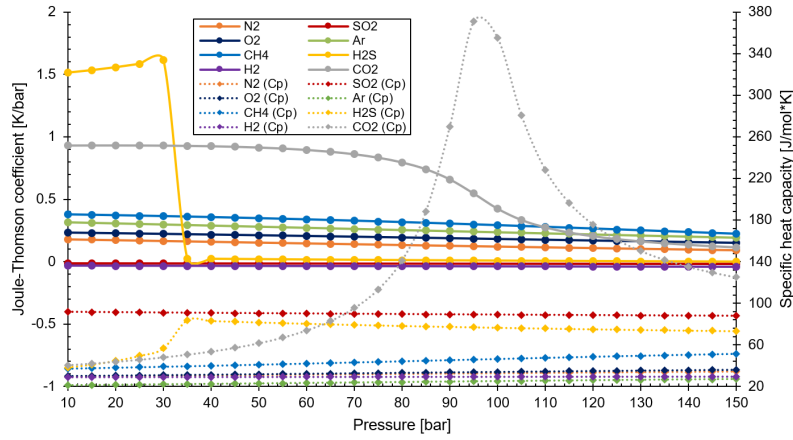


Figure 6.3: Joule-Thomson coefficient (solid) and specific heat capacity (dotted) of different pure components at a fixed temperature of 318K, after [35].

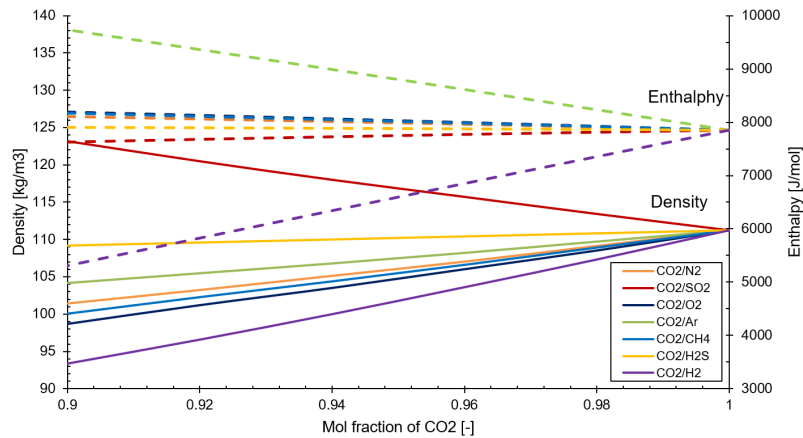


Figure 6.4: Density and enthalpy values of the CO<sub>2</sub>/impurity mixtures for various mixture compositions at 318K and 50 bar, after [35].

Simulations for impure CO<sub>2</sub> streams in this research have been conducted with GEM, which offers flexibility for implementation of additional gaseous components in its PR-EOS. Complementary to the simulations performed in earlier work by ZiabakhshGanji [25], vaporization of water in the gaseous phase is taken into account in these simulation cases and additional components are studied. Both the binary interaction coefficients ( $k_{ij}$ ) for the CO<sub>2</sub>-impurity mixture (see table 6.1) and the Henry coefficient, to quantify the solubility of the impurity initially not present in GEM (i.e. O<sub>2</sub>, SO<sub>2</sub>, H<sub>2</sub> and Ar), have been manually implemented. For the determination of the Henry coefficient of the CO<sub>2</sub>, H<sub>2</sub>S, CH<sub>4</sub> and N<sub>2</sub> components an enhanced correlation for solubility by Harvey (1996) is utilized, making the Henry coefficients a function of pressure, temperature and salinity. The Henry coefficients of the manually implemented components in GEM are adjusted for elevated pressures using the following equation [27], i.e.,

$$\ln(k_{H,i}) = \ln(k_{H,i}^o) + \frac{V_i^\infty(p - p_i^o)}{RT}, \quad (6.1)$$

where  $V_i^\infty$  is the partial molar volume in the water at infinite dilution and the superscript  $o$  refers to the reference condition. The reference Henry coefficient for each component (see table 6.4) are taken at a temperature of 306K, providing the best correspondence to the solubility calculated by the Harvey's correlation

in the region where the most significant cooling occurs with an injection rate of 35 kg/s and injection temperature of 45°C. However this leads to slight overestimation of the solubility calculated by the equation above in the regions behind and in front of the cooling front.

Table 6.1: Binary interaction coefficients implemented in GEM [80].

Mixture	CO <sub>2</sub> /N <sub>2</sub>	CO <sub>2</sub> /O <sub>2</sub>	CO <sub>2</sub> /CH <sub>4</sub>	CO <sub>2</sub> /H <sub>2</sub>	CO <sub>2</sub> /Ar	CO <sub>2</sub> /SO <sub>2</sub>	CO <sub>2</sub> /H <sub>2</sub> S
Interaction coefficient	-0.007	0.114	0.100	0.1582	0.163	0.046	0.099

To study the effect of each impurity individually, injection streams consisting of 95 mole% CO<sub>2</sub> and 5 mole% of the particular impurity are implemented. Since the effect of the salinity on solubility of the manually implemented components in GEM is not taken into account, a non-saline aqueous phase is implemented to obtain comparable results. The results of the simulations with an injection rate of 35 kg/s and injection temperature of 45°C are shown in figure 6.5. Similar to results obtained by ZiabkhshGhanji [25], the figure indicates that the cooling in the near wellbore region reduces for the majority of the impurities but increases for H<sub>2</sub> and SO<sub>2</sub>. It can be observed in figure 6.5a, that in the dry-out region where the thermal response is only affected by JTC, the presence of Ar results in a reduction and H<sub>2</sub> in an increase the cooling compared to pure CO<sub>2</sub>. For Ar this can be directly related to the increase of the heat capacity. Therefore, more heat is required to change the temperature of the mixture. The strong cooling effect of H<sub>2</sub> is caused by a combination of the considerable reduction of the density and heat capacity of the CO<sub>2</sub> stream in presence of H<sub>2</sub>. Apparently, this dominates over counteracting reduction in JT coefficient by H<sub>2</sub>. Besides, due to the lower temperature, less water evaporates in the CO<sub>2</sub>/H<sub>2</sub> stream as shown in figure 6.5d. The radial extent of the dry-out zone for this stream is therefore slightly less compared to other stream (<1 m).

The discrepancies in radial extent of the fronts in presence of the impurities with respect to pure CO<sub>2</sub> are negligible, except for SO<sub>2</sub> and H<sub>2</sub>. Presence of SO<sub>2</sub> significantly enlarges the dry-out front. As illustrated in figure 6.5c, the mole fraction of water in the CO<sub>2</sub> stream is significantly higher compared to other components and pure CO<sub>2</sub>. This indicates that more water vaporization takes place which enhances the cooling and extends the dry-out front. In addition, the injected SO<sub>2</sub> dissolves most easily in the aqueous phase and therefore the mole fraction of SO<sub>2</sub> dissolved in the aqueous phase is notably higher. As a result, in the region advancing the thermal front, where dissolution is the dominant thermal effect, the temperature increase is largest for the SO<sub>2</sub>-case. However, as mentioned above, the solubility and temperature increase is slightly overestimated in this region for the manually implemented components (i.e. SO<sub>2</sub>, H<sub>2</sub>, O<sub>2</sub> and Ar).

In Appendix E.2, the results of the simulations with a injection stream consisting of 90 mole% CO<sub>2</sub> and 10 mole% impurity are given. Similar results are obtained as in the case with 5 mole% impurity but the effects are more exposed in this case. However, injection of CO<sub>2</sub> streams with less than 95 mole% CO<sub>2</sub> are currently not widely applied in practice. In addition to the simulations conducted with a stream of 95 mole% CO<sub>2</sub> and 5 mole% impurity at 35 kg/s, also a lower injection rate of 10 kg/s was tested (see Appendix E figure E.3). A similar behavior is observed with respect to injection case at higher rate. At lower injection rate the discrepancy between the cooling in presence of the different impurities reduces except for H<sub>2</sub>. The larger relative deviation for H<sub>2</sub> presumably originates from the deviant behavior with respect to density at the lower absolute pressure values.

Next to the binary injection streams (i.e. CO<sub>2</sub>- impurity), also mixtures of CO<sub>2</sub> with multiple impurities, providing a better representation of realistic CO<sub>2</sub> streams, were defined based on average literature values (see table 6.2). Similar to the impure injection stream, the residual gas in the reservoir is composed of multiple components instead of pure methane, altering the flow behavior in the reservoir. A gas composition was defined analogous to the composition of the natural gas composition in the Dutch North Sea P18-4 field (see table 6.3). The natural gas has a higher density and compressibility, due to presence of additional components, compared to the pure methane.

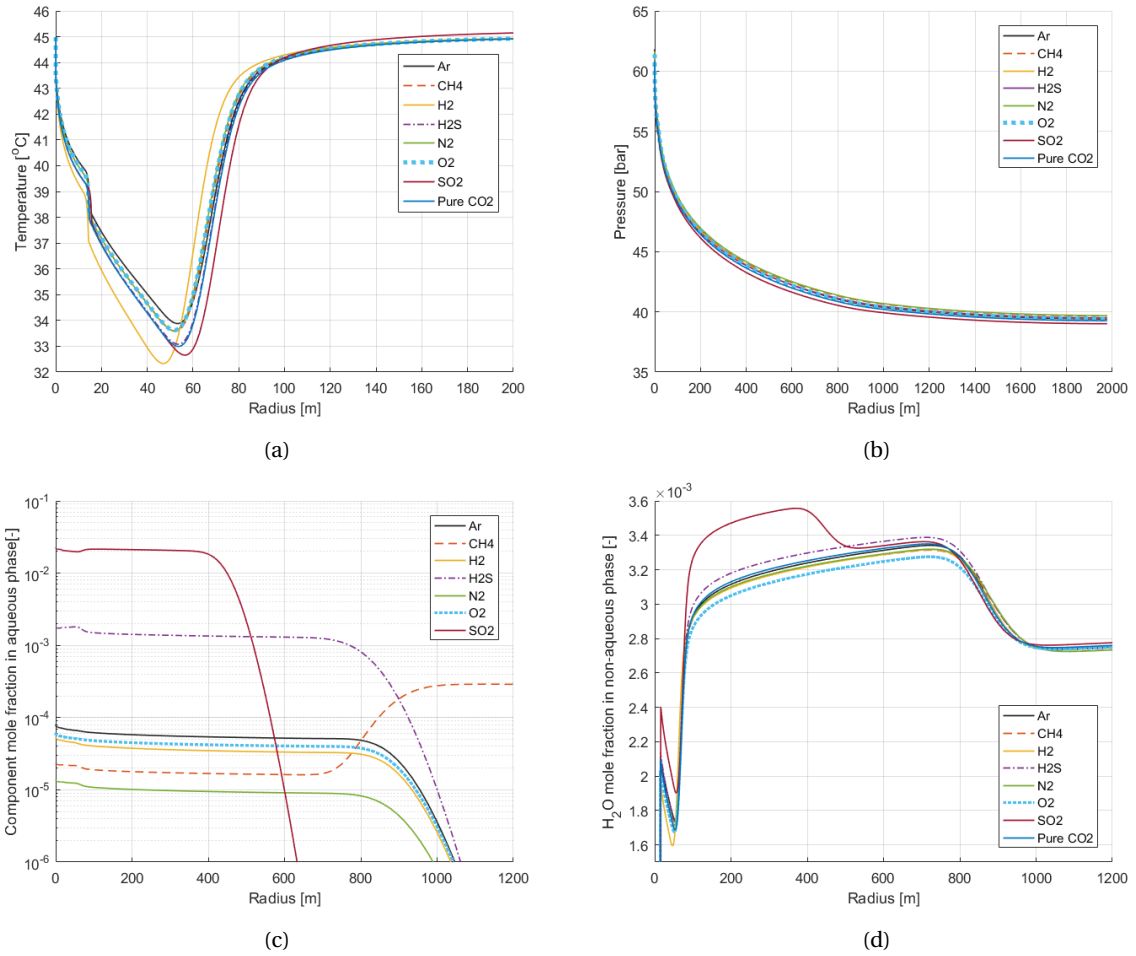


Figure 6.5: (Case 24) (a& b) Temperature and pressure profiles for the various impurities with injection composition of (95 mole% CO<sub>2</sub> + 5 mole% impurities) and for pure CO<sub>2</sub> after 1 year of injection at 35 kg/s; (c) Dissolution profile of the impurities in the aqueous phase and (d) profile of H<sub>2</sub>O components in the non-aqueous phase.

Table 6.2: Example of an impure CO<sub>2</sub> injection stream composition [79, 81].

Component	Mole fraction
CO <sub>2</sub>	0.945
N <sub>2</sub>	0.020
O <sub>2</sub>	0.010
CH <sub>4</sub>	0.008
H <sub>2</sub>	0.008
Ar	0.006
SO <sub>2</sub>	0.002
H <sub>2</sub> S	0.001

Table 6.3: Example of a natural gas composition (P18-4 field) [64].

Component	Mole fraction
CH <sub>4</sub>	0.865
C <sub>2</sub> H <sub>6</sub>	0.064
CO <sub>2</sub>	0.022
C <sub>3</sub> H <sub>8</sub>	0.019
C <sub>7+</sub>	0.013
C <sub>4</sub> H <sub>10</sub> (i,n)	0.008
N <sub>2</sub>	0.005
C <sub>5</sub> H <sub>12</sub> (i,n)	0.003
C <sub>6</sub> H <sub>14</sub> (n)	0.002

Table 6.4: Henry coefficients in (mole/kg/bar) at 306K and 1 atm [35].

Component	Henry coefficient
CO <sub>2</sub>	$2.59 \times 10^{-2}$
N <sub>2</sub>	$5.80 \times 10^{-4}$
O <sub>2</sub>	$1.02 \times 10^{-3}$
CH <sub>4</sub>	$1.22 \times 10^{-3}$
H <sub>2</sub>	$7.47 \times 10^{-4}$
Ar	$1.27 \times 10^{-3}$
SO <sub>2</sub>	$9.15 \times 10^{-1}$
H <sub>2</sub> S	$8.32 \times 10^{-2}$

The results of the simulations of the realistic CO<sub>2</sub> stream and the realistic gas composition are plotted in figure 6.6, concurrently with the original case with pure CO<sub>2</sub> injection in a reservoir containing pure CH<sub>4</sub>. As expected, the realistic impure CO<sub>2</sub> mixture reduces the near wellbore cooling since the mixture consists predominately of cooling reducing impurities. Besides, the effect on the extent of the dry-out front and the location of the minimum temperature in the reservoir compared to pure CO<sub>2</sub> injection is also negligible. The

cooling effect in a real gas however is slightly larger. In paragraph 5.1.1, it was substantiated that the near wellbore region converts rapidly to a CO<sub>2</sub>-brine system. Hence, the thermophysical properties of the injected CO<sub>2</sub> stream are only marginally influenced by the difference in initial gas composition. However, the composition does impact the flow behavior in the reservoir and corresponding pressure buildup. Because of the higher compressibility of the real gas, the pressure gradient in the near wellbore region is slightly higher compared to the pure methane case, causing additional JTC. Nonetheless, the effect is on the temperature profile is insignificant (below  $<1^{\circ}\text{C}$ ).

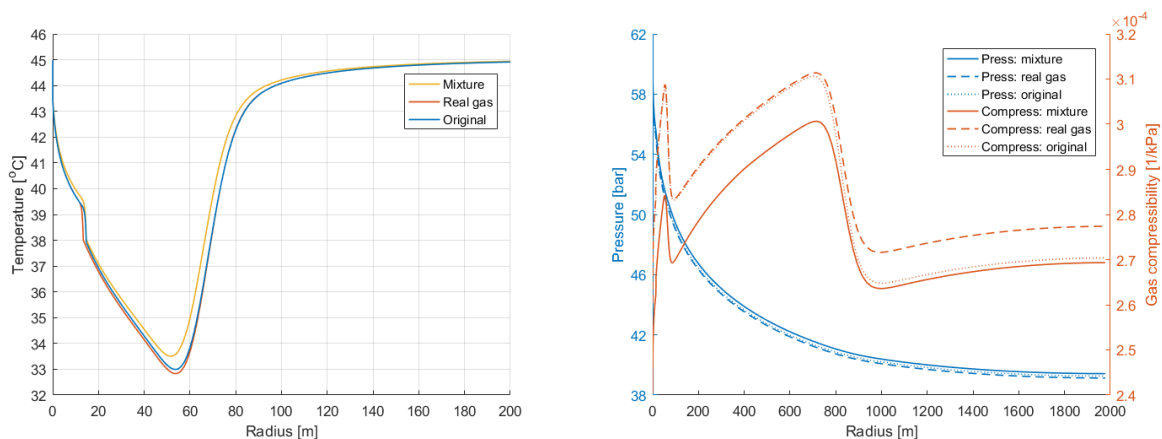


Figure 6.6: (Case 25) Temperature, pressure and compressibility profiles for a realistic CO<sub>2</sub> mixture with impurities injected in a pure methane reservoir (mixture), pure CO<sub>2</sub> injected in reservoir with a realistic natural gas composition (real gas) and pure CO<sub>2</sub> injected in a pure methane reservoir (original).

It should be noted that the simulations are conducted in absence of dissolved salt and salt precipitation. Although dissolved salt alters the solubility of the components, it is expected that the relative changes in solubility between components in presence of salt are equal. The permeability reduction due to salt precipitation is consequently also not incorporated. In earlier simulation, with equivalent simulation parameters, it was found that the cooling effect will be enhanced by approximately 0 to 2°C by salt precipitation.

## P18-4 test case

As a realistic test case, the currently nearly depleted P18-4 compartment of the P18 field in the North Sea is utilized. This field has been extensively studied in the CATO2 program and a wide variety of data is publicly available. For this test case, the geological field model of P18-4, containing properties for water saturation, permeability and porosity has been converted to a simulation model in GEM. In figure 7.1, an aerial overview of the model and a cross section intersecting the well are shown.

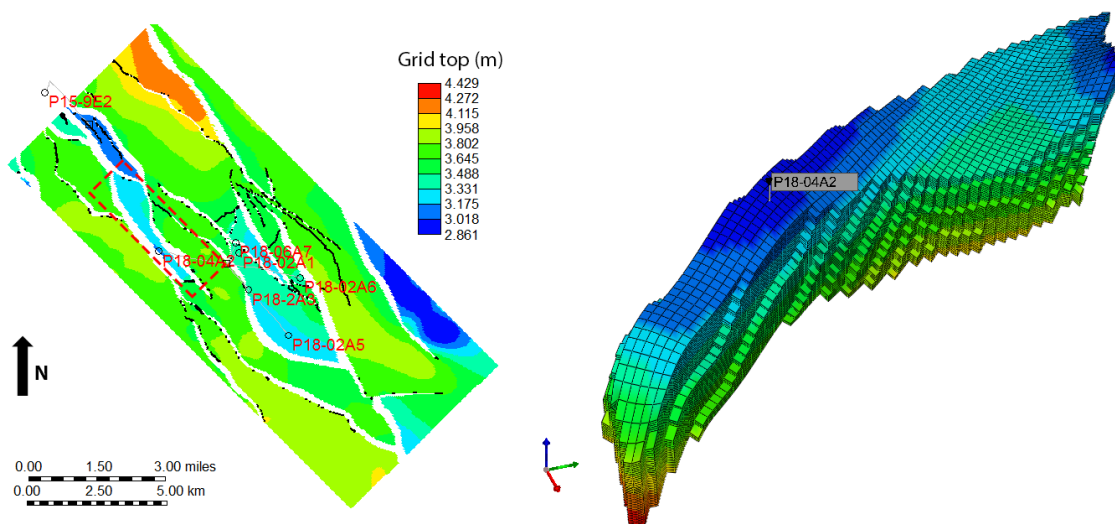


Figure 7.1: (left) Areal view of the complete P18 field in which the P18-4 compartment is indicated by the red box and (right) 3D view of the P18-4 compartment including the well location with an arbitrary color scheme.

P18-4 contains three distinct sandstone formations, i.e. the Hardegsen, Dethfurth and Volpriehausen, which are part of the Main Buntsandstein Subgroup [64] (see figure 7.2). The Dethfurth formation can be subdivided into Upper and Lower Dethfurth, each having different characteristic properties. The reservoir quality of the in the P18-4 model decreases over depth. As figure 7.1 illustrates, the P18-4 compartment within P18 field has an elongated geometry, widening towards the North-West and is bounded by two parallel faults. These faults intersect each other towards the South-West and resemble a horst-graben structure. The well is located in the narrow section in the South-Eastern part and perforates only the Hardegsen and Upper and Lower Dethfurth over an interval of approximately 100 m from the top of the reservoir.

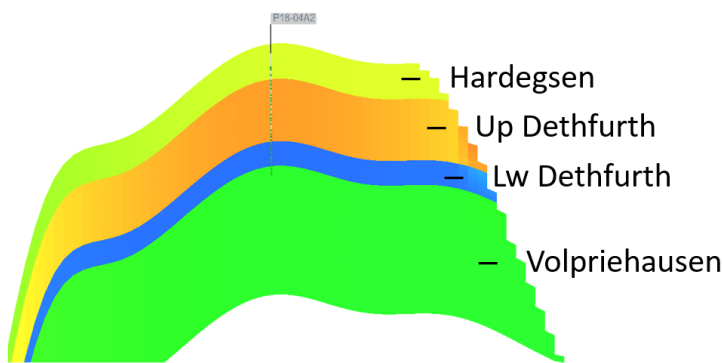


Figure 7.2: P18-4 cross section in NW-SE direction intersecting the well.

Table 7.1: Input values for the GEM simulation on the P18-4 field model.

Parameter	Value (unit)
$Q_{inj}$	1.1 (Mt/yr)
$T_{inj}$	45 ( $^{\circ}$ C)
$T_{ini,res}$	117 ( $^{\circ}$ C)
$p_{ini,res}$	30 (bar)
$\lambda_r$	2.56 (W/m/ $^{\circ}$ C)
$\rho_r$	2600 (kg/m <sup>3</sup> )
$C_{p,r}$	920 (J/kg/ $^{\circ}$ C)
$x_{NaCl}$	15 (wt%)
Gas composition	100% CH <sub>4</sub>
Stream composition	100% CO <sub>2</sub>

## 7.1. Model initialization

The simulation model has not been matched to the production history. The volume and reservoir properties (e.g. permeability and water saturation) of the simulated P18-4 model can therefore deviate from the properties that can be derived from the field production data acquired over the years. Nevertheless, special care is taken to match the permeability in the near wellbore region to available well test data to obtain an appropriate estimate of the injectivity. The average values for the permeability, porosity and water saturation of the formations in the model are indicated in table 7.2 combined with values obtained from petrophysical studies.

Table 7.2: P18-4 model and petrophysical properties.

Parameter	Hardegsen		Upper Dethfurth		Lower Dethfurth		Volpriehausen	
	Model	Petro.	Model	Petro.	Model	Petro.	Model	Petro.
Thickness (m)	30	24	53	47	21	19	110	101
Grid cells ( $z$ -direction)	5	-	7	-	5	-	20	-
Permeability (mD)	192	207	39	0.8	15	0.1	0.13	0.0
Porosity (-)	0.13	0.13	0.080	0.092	0.065	0.065	0.01	0.049
Water saturation (-)	0.30	0.24	0.54	0.47	0.52	0.39	0.97	0.92

### 7.1.1. Local grid refinement

The reservoir model consist of a grid with cell sizes of 50 m in the horizontal directions ( $x$  and  $y$ ) and 4.2 to 6.6 m in vertical direction ( $z$ ), depending on the formation. Due to the relatively limited resolution in  $x$  and  $y$  direction in the original grid, the physical effects in the near wellbore region are averaged over substantial horizontal distances. In order to accurately model the near wellbore region within the larger field model, grid refinement is applied to the cells intersected by the well and in the direct well vicinity. The effect of grid refinement on pressure and temperature distribution on a Cartesian grid is shown in Appendix F.1. For the final simulations with the P18-4 model, a block division of 8 in  $x$  and  $y$  direction is implemented, resulting in cells with approximately 6.25 m in  $x$  and  $y$  direction within the refined region. Higher refinement was restricted due to modeling limitations.

### 7.1.2. Permeability matching

Since the main focus of this study is on the near wellbore region and injectivity of the CO<sub>2</sub>, the permeability in this region is of major importance. Due to the lack of proper history matching, the permeability of this region has been matched to initial well tests of the P18-4A2 well, which indicated a Kh of 8200 mDm and with an average permeability of 85 mD. In addition, the skin factor of -3.1, derived from the well test data, is also implemented to accurately match the injectivity of the well.

### 7.1.3. Initial pressure, temperature and water saturation

The initial reservoir pressure before gas production was approximately 340 bar [64]. Based on the production history of the P18-4 compartment, showing a highly linear line in the  $p/Z$  curve, it can be concluded that the compartment has a strong tank-like behavior and aquifer influx or gas migration from adjacent fields is absent. Due to the absence of a history matched model, the pressure after depletion and at the onset of  $\text{CO}_2$  injection has been adopted from literature and was set to 30 bar. Likewise, the remaining parameters as reservoir temperature, thermal rock properties and brine salinity are also based on literature values.

### 7.1.4. Relative permeability and capillary pressure curves

To model the relative permeability of the non-wetting non-aqueous and wetting aqueous phase in the P18-4 model, generalized Corey functions are implemented, i.e.,

$$k_{r,nw} = k_{r,nw,wr} \left( \frac{S_{nw} - S_{nw,r}}{1 - S_{nw,r} - S_{w,r}} \right)^{n_{nw}} \quad (7.1)$$

and

$$k_{r,w} = k_{r,w,nwr} \left( \frac{S_w - S_{w,r}}{1 - S_{nw,r} - S_{w,r}} \right)^{n_w} \quad (7.2)$$

where  $k_{r,nw,wr}$  is the relative permeability of the non-wetting phase at residual wetting phase saturation,  $k_{r,w,nwr}$  is the relative permeability of the wetting phase at residual non-wetting phase saturation and  $n_{nw}$  and  $n_w$  are the non-wetting phase and wetting phase Corey exponents respectively. The Corey functions scale the relative permeability curves based on relative permeability endpoints of non-aqueous and aqueous phase at residual saturation of the other phase. Endpoint values for the non-aqueous and aqueous phase are 0.8 and 0.2 respectively. Furthermore, values of the Corey exponent for the aqueous brine phase and non-aqueous  $\text{CO}_2\text{-CH}_4$  mixture are 4 and 2 respectively, corresponding to average values for depletion driven gas reservoirs with reasonably sorted sandstone and a fairly stagnant brine phase.

Due to the relatively large porosity and related water saturation contrast within the formations, the relative permeability and capillary pressure curves are defined per porosity range instead of formation type. The following porosity ranges are defined: (1)  $\phi > 0.15$ , (2)  $0.12 < \phi \leq 0.15$ , (3)  $0.09 < \phi \leq 0.12$ , (4)  $0.06 < \phi \leq 0.09$ , (5)  $0.03 < \phi \leq 0.06$  and (6)  $\phi \leq 0.03$ . In figure 7.3, these curves are depicted. For the calculation of the capillary pressure, the gas-water contact was set at a depth of 3377 m [64].

Capillary pressure is modeled using the Van Genuchten equation given in equation 2.51, with generic fitting parameters corresponding to the Buntsandstein. The absolute value of the capillary pressure is based on the height above the gas water contact (GWC). In P18-4, the GWC was found at a depth of 3377 m [64], while the top of the reservoir structure was determined at 3160 m.

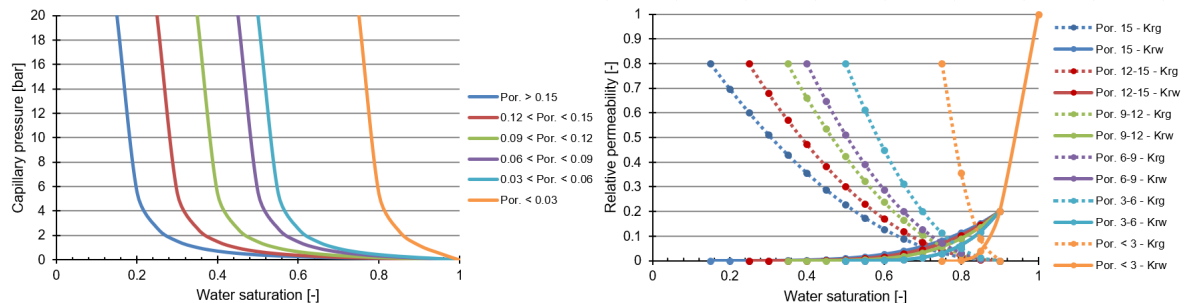


Figure 7.3: Capillary pressure and relative permeability curves for each of the porosity classes, implemented in the P18-4 simulation model.

An overview of the simulation input values is provided in table 7.1.

## 7.2. Simulation results

### 7.2.1. CO<sub>2</sub> flow, near wellbore cooling and pressure behavior

The CO<sub>2</sub> injected in the upper layers of the reservoir (i.e. Hardegsen, Upper Dethfurth and Lower Dethfurth), spreads out at a considerable rate shortly after the injection started. In figure 7.4, the mole fraction of the CO<sub>2</sub> component in the non-aqueous phase is shown. Due to the elongated geometry of the reservoir and the placement of the well in a thin section of the reservoir, the parallel boundaries are rapidly reached. The distribution therefore deviate significantly from a radial injection model and the mixing front converts shortly after injection from a circular to a fairly straight shape. Because of the better reservoir quality and therefore higher injectivity of the Hardegsen compared to the Dethfurth, a higher amount of CO<sub>2</sub> is injected in the Hardegsen formation and the mixing front is therefore further advanced in the reservoir. In addition, barely no CO<sub>2</sub> flow in the unperforated, nearly fully water saturated and low quality Volpriehausen formation is observed.

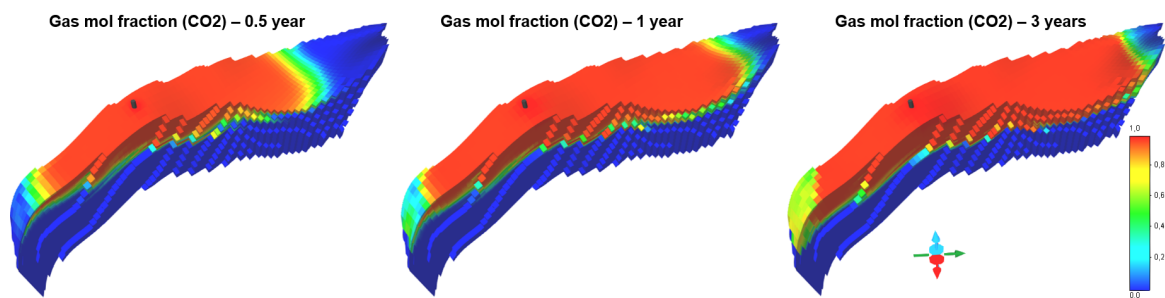


Figure 7.4: (Case 26) CO<sub>2</sub> distribution in the reservoir over time.

The corresponding temperature profiles are depicted in figure 7.5. These profiles indicate that the cooling in the near wellbore region remains within 2°C with respect to the initial CO<sub>2</sub> injection temperature and the JTC effect is negligible. For the cooling fronts the same holds as for the mixing fronts, namely that extent and distribution is closely correlated to the heterogeneity of the reservoir. The extent of the thermal fronts is higher in the upper layers. Due to the limited cooling effect, no discrepancy can be determined between the minimum temperature reached in each formation layer (i.e. Hardegsen, Upper Dethfurth and Lower Dethfurth) since it is roughly the same in each layer, except for layers with extraordinary low permeabilities which are indicated by a minimal extent of the temperature front.

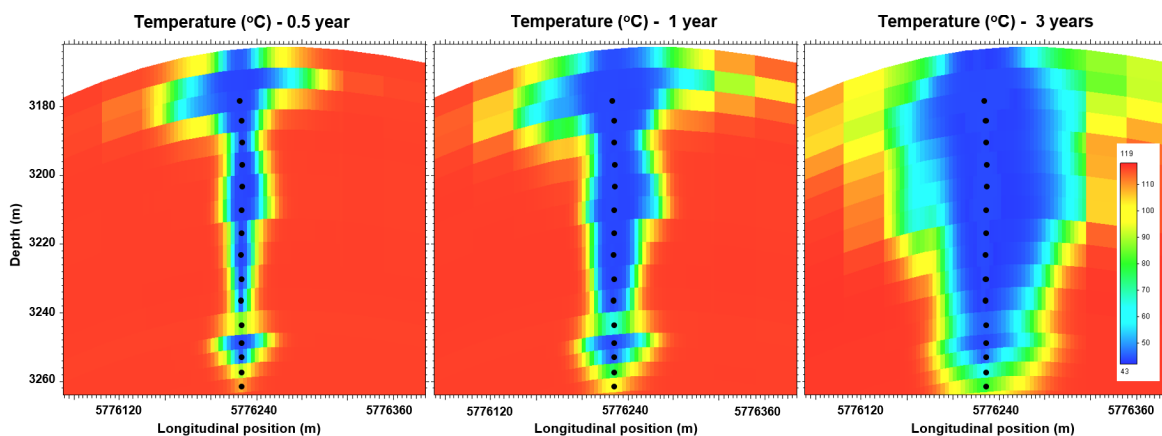


Figure 7.5: Temperature distribution plotted over time in a zoomed cross section (NW-SE direction) parallel to the reservoir boundary intersecting the well, wherein the perforated cells are indicated by the black dots. Note that the perforations in the upper two layers are not included in this slab, due to the inclined well trajectory, but do exist.

Reasons for the limited cooling in the reservoir are found by analyzing in the pressure behavior of the reservoir, displayed in figure 7.6. After 0.5 years of injection, the pressure in the area around the well already exceeds the critical pressure of CO<sub>2</sub>. The exact time required to reach critical pressure in the near wellbore

region is only 3 months. Hence, the time in which CO<sub>2</sub> is injected in gaseous phase, wherein the JT coefficient is large, is limited and the reduction of the reservoir temperature is consequently small.

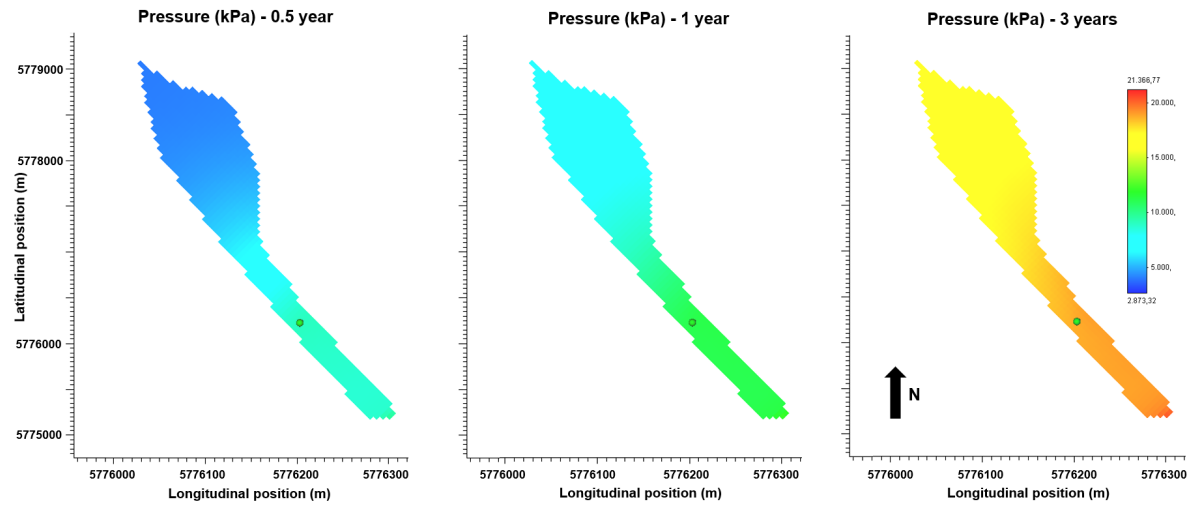


Figure 7.6: Pressure distribution in the reservoir over time in areal perspective, where the well location is indicated by the green dot.

The pressure buildup rate and gradient in the near wellbore area in the reservoir, controlling the cooling, can be directly related to both the volume in the reservoir, reservoir geometry and well location with respect to the reservoir boundaries. Influences of reservoir geometry of in combination with well location have been extensively tested in Appendix F.2. Because of the elongated geometry and location of the well close to the parallel no-flow boundaries, the pressure wave reaches the boundary shortly after injection and a very fast pressure buildup is observed in the region around the well.

In figure 7.7, near wellbore profiles after 1 year of injection are shown for the field model, a radial model with an identical volume and reservoir parameters as the field model, and the radial model with a volume and parameters identical to the model sensitivity study to compare the pressure behavior and corresponding cooling. In all models, identical effects occur, i.e. water vaporization, CO<sub>2</sub> dissolution, JTC. However, the magnitude particularly of the JT cooling varies strongly between the models.

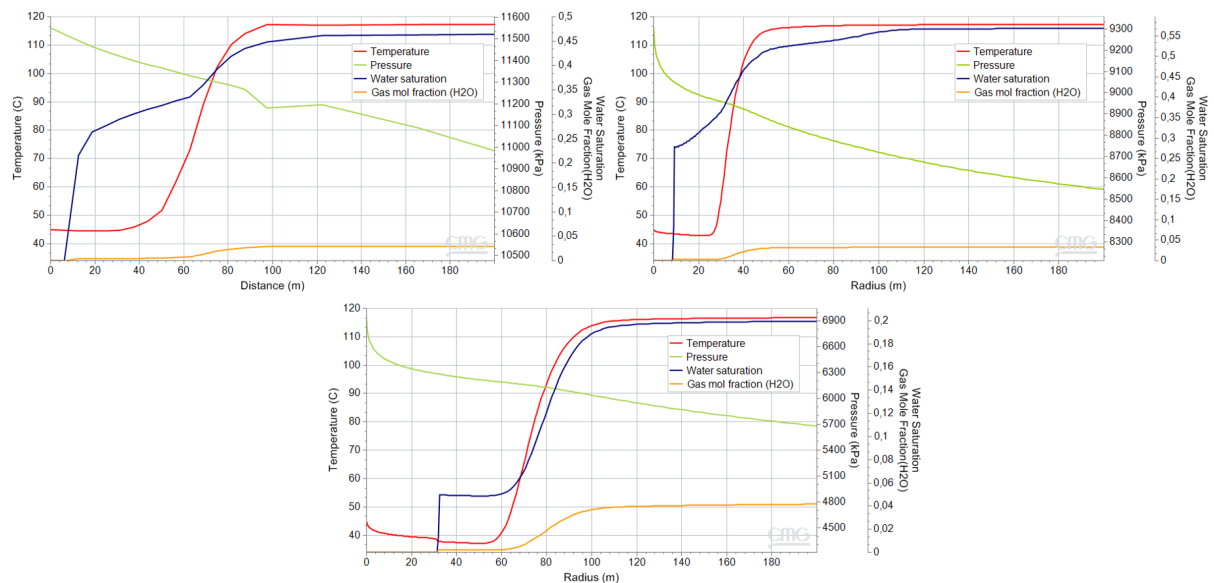


Figure 7.7: Comparison of field model (left top), radial model with parameters matching to the field model (right top) and radial model equivalent to the sensitivity study (bottom).

It can be observed that the absolute value of the pressure and gradient significantly deviate between the models. In the radial field model, the absolute value of the pressure is lower compared to the original field model, indicating a slower pressure buildup. In addition, the gradient in the near wellbore region is higher. These two factors result in a slightly higher cooling effect in the radial field model compared to the original field model. Since the volume in both models is roughly identical, the differences in pressure behavior can be mainly attributed to combination of the geometry of the field and well location with respect to the boundaries and slightly to the limited refinement around the well in the original field model. Moreover, because of the larger volume in the radial sensitivity study model, the pressure buildup is considerably slower compared to the other two models. Hence, the CO<sub>2</sub> is injected for a longer period in gaseous phase in the radial sensitivity model, because more time is required to reach the critical pressure. The reservoir system consequently has a longer time frame with considerable JTC and the reservoir temperature is therefore further reduced.

### 7.2.2. Well location

To study the effect of the well location on the pressure behavior, the well location is replaced within the field model (see figure 7.8 (right)). The reservoir quality of the cells perforated by the well at the modified location was adjusted to match the initial location and the grid refinement around the well is identical. In figure 7.8 (left), the temperature and pressure profiles are shown. A similar discrepancy is visible as in the comparison between the original field model and radial field model. Due to the fact that the well is placed at a greater distance from the boundary in a less confined area the influences of the boundaries on the pressure are less. At the new location, the pressure buildup is slower and gradient higher. Consequently, the cooling effect is slightly higher at the modified well location but remains negligible in comparison with the JTC observed in the sensitivity study because the critical pressure is rapidly reached.

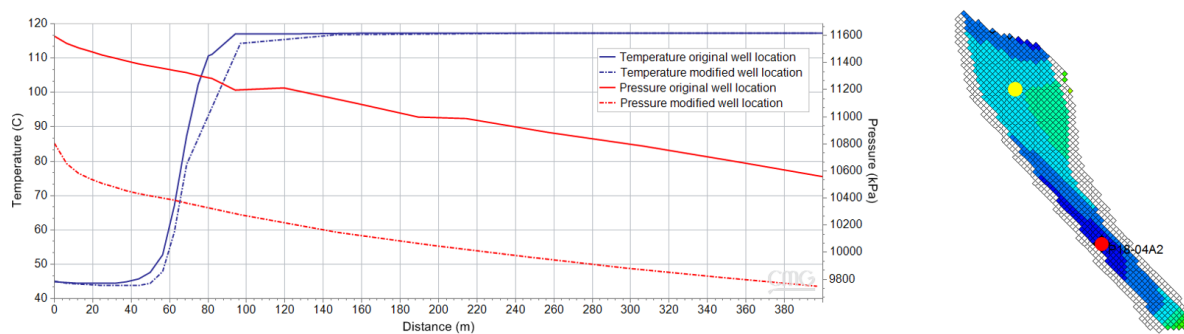
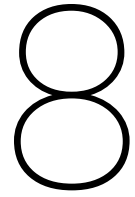


Figure 7.8: (left) Temperature and pressure profile for the original and modified well location after 1 year of injection and (right) position of the original (red) and modified well (yellow) in the P18-4 field.



# Discussion

## **Sensitivity study (ECO2MG)**

The radial models used in the sensitivity proved to provide highly favorable conditions for the appearance of a significant JTC effect. The large volume of the reservoir, due to the extensive radius in combination of the optimal location of the well with respect to the boundary, led to a slow buildup of the reservoir pressure. Hence, CO<sub>2</sub> was injected for a considerable time span in gaseous condition. This was intentionally done to exacerbate the maximum cooling in the near wellbore region and to amplify the sensitivity of the temperature response on the perturbed parameters in the sensitivity study. In reality, the gradient and pressure buildup are potentially not as ideal as was demonstrated in the field model test case. The distance of the well with respect to no-flow boundaries and geometry of the model notably changes the pressure behavior. As discussed, the cooling effect would reduce for smaller volumes, in which injection conditions of CO<sub>2</sub> would rapidly change from gaseous to supercritical.

A constant rate injection was implemented in the simulations displayed throughout this thesis. Usage of a fixed constant pressure injection over the injection period was also tested at the highly depleted reservoir conditions. However, constant pressure injection leads to an extreme pressure gradient between the wellbore and reservoir at early injection times. As a consequence, excessive and unrealistic cooling occurred and extraordinary injection rates were observed. In addition, also from a practical perspective constant rate injection is preferred due to the expected constant supply of CO<sub>2</sub> from the connected pipeline system but may not be always feasible.

The numerical stability of the ECO2MG module showed, in particular for the 2D cases, a high dependency on the implemented grid. The latitude of grid spacing and reservoir sizes was therefore constrained. As a matter of fact, the grid spacing used in the 1D simulation model did not provide converged solutions when extended to a 2D model while on the other hand with the current 2D grid and the parameters convergence could not be achieved for reservoirs smaller than 4 km. Due to the current grid spacing, which offers high resolution around the well but less further into the reservoir, processes taking place at greater distances to the well are affected by numerical dispersion.

Local thermal and instantaneous thermodynamic equilibrium have been assumed in the numerical simulators utilized in this thesis. At the high flow rate assumed, excessive cooling was found in several simulation cases shortly after the start of the injection. It can be argued that the assumption of the local thermal equilibrium only holds if the time required for conduction to establish a thermal equilibrium between rock and fluid is less than the cooling rate of the fluid. Therefore, as extreme JTC occurs at early injection times this assumption may lead to inaccuracies and the temperature of the injected CO<sub>2</sub> can actually reach lower values than currently calculated. Besides, due to the instantaneous thermodynamic equilibrium in combination with high injection rates, processes of vaporization and dissolution can be overestimated and in case of strong capillary pressure lead to unrealistic results. In these cases, a kinetics approach instead of the thermodynamic equilibrium is recommended [53].

The Verma-Prueess model, used to calculate the permeability reduction as a function of the salt precipitation, is highly sensitive to the fitting parameters. For this study average values corresponding to sandstones were implemented for these fitting parameters. However for better estimations, the parameters should be fitted to experimental data in order to provide an accurate indication of the permeability reduction.

#### **P18-4 test case (GEM)**

History matching of the P18-4 model was not conducted before the onset of the CO<sub>2</sub> injection phase. The pressure behavior of the modeled P18-4 model consequently differs from the realistic field, because of the mismatch in volume. However, since this field study is performed to determine the physical effects in the near wellbore region in a heterogeneous realistic framework, in terms of geometry, reservoir structure, well location and distribution of reservoir properties (e.g. water saturation, permeability and porosity), the inadequacy of the behavior of the model relative to the production history is rather irrelevant. Therefore, the modeling study was considered as a test case instead of a real field study. Besides, SCAL data (e.g. relative permeability and capillary pressure curves), affecting the flow behavior in the reservoir, were not available for the P18-4 field and interpreted values were used instead.

Grid refinement was applied to the grid cells intersected by and in the direct vicinity of the well. The grid refinement leads to better computational accuracy of the parameters and is especially important to capture the effect in the near wellbore region. However, because of numerical issues in GEM, the refinement was restricted to a factor of 8 times the original cell size. In addition, due to the large grid cell sizes outside the refined area the calculated output can be affected by numerical dispersion.

Salt precipitation has not been accounted for in the GEM simulations on the field model because of modeling limitations. Due to the fact that the water vaporization is included in the simulations but the detrimental effect of salt precipitation is absent, the effective permeability and resulting injectivity of CO<sub>2</sub> are overestimated. In the sensitivity study and comparison between GEM and ECO2MG it was observed that the salt precipitation causes a higher pressure gradient in the near wellbore region and therefore results in additional cooling between 0 and 2°C. Besides, when taking the high saturation values of the P18-4 model into account together with the relatively high salinity of the brine, more salt would precipitate compared to the sensitivity study. This leads to higher local salt saturations in the near wellbore region and eventually could cause the additional cooling effect, due to the increase in pressure gradient, to be even higher. The cooling observed in the temperature profiles of P18-4 are therefore presumably the absolute minimum amount of cooling that will occur.

# 9

## Conclusions

In this thesis, the near wellbore effect induced by CO<sub>2</sub> injection in gas reservoirs at depleted conditions and the influence of these effects on the CO<sub>2</sub> injectivity have been thoroughly studied. The following conclusions can be drawn:

### **Near wellbore cooling**

- Cooling in the near wellbore region is predominantly attributed to the, by injection induced, Joule-Thomson effect in case of highly depleted reservoir conditions. Other thermal effects as endothermic water vaporization and exothermic CO<sub>2</sub> dissolution have a less significant contribution to the temperature distribution in the near wellbore region, compared to the JTC effect at the high flow rates and remaining simulation parameters considered.
- The magnitude of the Joule-Thomson effect is primarily affected by parameters that directly impact the Joule-Thomson coefficient of the injected CO<sub>2</sub> stream or the induced pressure gradient by injection. Examples of these parameters are the CO<sub>2</sub> injection rate, CO<sub>2</sub> injection temperature, reservoir permeability and initial reservoir pressure.
- Excessive cooling in the order of 15 to 20<sup>o</sup>C can arise in the reservoir, particularly for large volume reservoirs in which considerable time is required to reach critical pressure, combined with CO<sub>2</sub> injection at high rates and low temperatures (i.e. 35 kg/s and <45<sup>o</sup>C respectively). Injection of gaseous CO<sub>2</sub> below 30<sup>o</sup>C at high flow rates can therefore potentially lead to risky conditions within the hydrate formation window in the near wellbore region.

### **Dry-out and salt precipitation**

- Effective permeability of CO<sub>2</sub> in the dry-out zone, that develops around the well during the injection process, increases for the considered reservoir systems, enhancing the overall injectivity of CO<sub>2</sub> into the reservoir. The increase in relative permeability of CO<sub>2</sub> due to the vaporization of water in the near wellbore region dominates over the decrease in absolute permeability caused by the resulting salt precipitation. Capillary backflow effects, which can lead to severe salt precipitation in the vicinity of the well and full clogging of the reservoir, were found to be negligible at high flow rates comparable to rates of realistic field scale injection processes. Nevertheless, capillary backflow can potentially jeopardize a CO<sub>2</sub> injection process if the flow rate drops far below the critical flow rate and the salinity of brine is such that an exorbitant amount of salt precipitates in the vicinity of the well.

### **Near wellbore cooling management**

- Optimal injection conditions to mitigate potential hazardous conditions in the reservoir were found to be highly case specific. Nonetheless, cooling in the near wellbore region can be controlled by proper interplay between the operational injection parameters, i.e. injection rate and injection temperature, and the prevailing reservoir pressure. Hereby, the CO<sub>2</sub> phase condition is of vital importance because this correlates to the JT coefficient and corresponding JTC. As long as the reservoir pressure in the near wellbore region is below critical pressure of CO<sub>2</sub> and CO<sub>2</sub> is injected in gaseous phase at low temperatures, special care should be taken to constrain excessive cooling.

- Injection of less pure CO<sub>2</sub> streams can be beneficial in both economic as practical perspective in terms of the cooling effect. Impurities alter the thermophysical properties of the injection stream. The majority of the studied impurities, except SO<sub>2</sub> and H<sub>2</sub>, reduce the injection induced Joule-Thomson cooling in the near wellbore region compared to pure CO<sub>2</sub> injection. For the tested impurity concentrations the deviation in minimum temperature reached in the reservoir was in the range of 2°C. Moreover, the inaccuracy of modeling with a pure CO<sub>2</sub> injection stream with respect to a realistic CO<sub>2</sub> stream compositions was found to be negligible, i.e. less than 0.6°C over the entire injection phase.

#### **P18-4 test case**

- The well location relative to the boundaries and reservoir volume partly control the magnitude of the cooling in the well. In the P18-4 model, which has an elongated geometry, well location close to the boundaries of the reservoir and a relatively small volume, a different pressure behavior was observed compared to the radial model used in the sensitivity study. Due to the combination of smaller volume and well location close to the boundary in the P18-4 model, the time required to reach the critical pressure in the reservoir was limited. On the same hand, the configuration of a radial model is highly favorable for JTC because of the optimal location of the well with respect to the boundaries. Both the high rapidity of the pressure buildup and low gradient in the vicinity of the well in the P18-4 model are not in favor of the the JTC in the reservoir. Hence, the cooling effect in the P18-4 model was constrained to only 2°C, without accounting for salt precipitation, instead of the extensive cooling of more than 10°C in the radial model.
- Local heterogeneity of the formation highly impacts the distribution of the thermophysical effects occurring in the near wellbore region. Similar to the 2D results of the sensitivity study, it was found that the extent of the thermal front, location of the minimum temperature reached in the reservoir and dry-out zone which corresponds to the salt precipitation region, were distributed according to the local heterogeneity. In layers with a higher injectivity, the thermophysical effects are stretched out over a larger area. However, partly attributed to the mutual heat exchange, substantial differences in cooling over the injection height is not observed.

# 10

## Recommendations and future work

- Coupling of the non-isothermal reservoir simulator with a thermal wellbore model: during transport from surface to the reservoir through the wellbore, similar physical effects as observed during injection in depleted gas fields, will arise (e.g. phase changes and Joule-Thomson cooling). The temperature of the CO<sub>2</sub> arriving down hole consequently deviates from the injection temperature at the surface. As observed in the simulation results, the magnitude and appearance of the physical effects in the reservoir highly depend on the down hole injection temperature of the CO<sub>2</sub> into the reservoir. For accurate modeling and precise determination of the required CO<sub>2</sub> injection temperature at the surface to mitigate potential risky conditions in the reservoir and wellbore, a fully coupled non-isothermal compositional wellbore-reservoir simulator is required. However, these models are currently scarce or nonexistent [60].
- Modeling of geomechanical near wellbore effects: the strong cooling observed in the radial simulations presented, potentially induces large thermo-elastic stresses around the wellbore and increases the ease of fracture initiation in the reservoir. Consequences of the cooling on the thermal stresses and fracture initiation and propagation were not addressed in this thesis. However, fractures can enhance the injectivity of CO<sub>2</sub> but also pose a threat to the integrity of the sequestration processes in terms of cap rock or wellbore leakage. Hence, the integration of a geomechanics module in the numerical simulators, to determine the injectivity enhancement but also the integrity risks, would be valuable.
- Modeling of geochemical near wellbore effects: the geochemical effects treated in this research are restricted to salt precipitation and hydrate formation. Other geochemical effects as formation of carbonic acid and the related chemical reaction with rock minerals have not been modeled. In the Dutch North Sea gas fields, the vast majority of depleted reservoirs are composed of sandstones. Due to its composition, these formations are barely reactive with the weak carbonic acid that develops in the reservoir. Hence, modeling of the geochemical effects in this case was not relevant. For CO<sub>2</sub> storage in general however, modeling of the interaction between rock and carbonic acid in the near wellbore region can be relevant especially for reactive carbonate reservoirs. The resulting precipitation and dissolution reactions can lead to changes in injectivity and are therefore worthwhile to study.
- Validation of simulation results at high rates on field scale: occurrence of the near wellbore effects have been extensively demonstrated and tested in laboratory experiments. However, these effects are mostly studied isolated and the conditions and parameters as flow rates used in the majority of these experiments do not match with the values corresponding to a realistic injection scenario in depleted gas fields. Therefore, although field measurements of these effects are extremely challenging and potentially impossible with the state-of-the-art technology, it is essential that proper data is acquired in the ongoing and upcoming CO<sub>2</sub> storage pilot projects, to test the accuracy of the simulators at field scale.

# Bibliography

- [1] Chen, K., Winter, R. C., and Bergman, M. K. Carbon dioxide from fossil fuels. *Energy Policy*, 8(4):318–330, 1980.
- [2] Zhong, W. and Haigh, J. The greenhouse effect and carbon dioxide. *Weather*, 68(4), 2013.
- [3] Marchal, V., Dellink, R., Vuuren, D. V., Clapp, C., Château, J., Lanzi, E., Magné, B., and Vliet, J. V. Climate change. In *OECD environmental outlook to 2050*, pages 71–147. 2012.
- [4] Metz, B., Davidson, O., de Coninck, H., Loos, M., and Meyer, L. IPCC Special Report: Carbon Dioxide Capture and Storage. Technical report, Cambridge Univ Press, Cambridge, UK, 2005.
- [5] Bouzalakos, S. and Mercedes, M. Overview of carbon dioxide (CO<sub>2</sub>) capture and storage technology. *Developments and Innovation in Carbon Dioxide (CO<sub>2</sub>) Capture and Storage Technology*, 1:1–24, 2010.
- [6] Nordbotten, J. M. and Celia, M. A. *Geological Storage of CO<sub>2</sub>: Modeling Approaches for Large-Scale Simulation*. NJ: Wiley, Hoboken, 2012.
- [7] Global CCS Institute. Geological CO<sub>2</sub> storage. 2013.
- [8] Class, H., Ebigbo, A., Helmig, R., Dahle, H. K., Nordbotten, J. M., Celia, M. A., Audigane, P., Darcis, M., Ennis-King, J., Fan, Y. Q., Flemisch, B., Gasda, S. E., Jin, M., Krug, S., Labregere, D., Beni, A. N., Pawar, R. J., Sbai, A., Thomas, S. G., Trenty, L., and Wei, L. L. A benchmark study on problems related to CO<sub>2</sub> storage in geologic formations. *Computational Geosciences*, 13(4):409–434, 2009.
- [9] Hughes, D. S. Carbon storage in depleted gas fields: Key challenges. *Energy Procedia*, 1(1):3007–3014, 2009.
- [10] Hannis, S., Pearce, J., Chadwick, A., and Kirk, K. Case Studies of CO<sub>2</sub> Storage in Depleted Oil and Gas Fields. Technical report, IEAGHG, 2017.
- [11] Oldenburg, C. Joule-Thomson cooling due to CO<sub>2</sub> injection into natural gas reservoirs. *Energy Conversion and Management*, 48(6):1808–1815, 2007.
- [12] Orlic, B. Geomechanical effects of CO<sub>2</sub> storage in depleted gas reservoirs in the Netherlands: Inferences from feasibility studies and comparison with aquifer storage. *Journal of Rock Mechanics and Geotechnical Engineering*, 8(6):846–859, 2016.
- [13] EBN. CO<sub>2</sub> transport- and opslagstrategie. 2018.
- [14] Pruess, K. Formation dry-out from CO<sub>2</sub> injection into saline aquifers: 2. analytical model for salt precipitation. *Water Resources Research*, 45(3):1–6, 2009.
- [15] Pruess, K. and Müller, N. Formation dry-out from CO<sub>2</sub> injection into saline aquifers: 1. effects of solids precipitation and their mitigation. *Water Resources Research*, 45(3):1–11, 2009.
- [16] Muller, N., Qi, R., Mackie, E., Pruess, K., and Blunt, M. J. CO<sub>2</sub> injection impairment due to halite precipitation. *Energy Procedia*, 1(1):3507–3514, 2009.
- [17] Zatsepina, O. Y. and Pooladi-Darvish, M. Storage of CO<sub>2</sub> as hydrate in depleted gas reservoirs. *SPE Reservoir Evaluation & Engineering*, 15(1):98–108, 2012.
- [18] Maloney, D. R. and Briceno, M. Experimental Investigation of Cooling Effects Resulting from Injecting High Pressure Liquid or Supercritical CO<sub>2</sub> Into a Low Pressure Gas Reservoir. *Petrophysics*, 50(4):335–344, 2009.

- [19] Janicki, G., Schlüter, S., Hennig, T., Lyko, H., and Deerberg, G. Simulation of Methane Recovery from Gas Hydrates Combined with Storing Carbon Dioxide as Hydrates. *Journal of Geological Research*, 2011 (May):1–15, 2011.
- [20] Peters, E., Pizzocolo, F., Loeve, D., Fokker, P. A., Hofstee, C., Orlic, B., and Maas, J. G. Consequences of thermal fracture developments due to injection cold CO<sub>2</sub> into depleted gas fields. *Energy Procedia*, 2013.
- [21] Bao, J., Xu, Z., and Fang, Y. A coupled thermal-hydro-mechanical simulation for carbon dioxide sequestration. *Environmental Geotechnics*, 3(5):312–324, 2016.
- [22] Hou, Z., Gou, Y., Taron, J., Gorke, U. J., and Kolditz, O. Thermo-hydro-mechanical modeling of carbon dioxide injection for enhanced gas-recovery (CO<sub>2</sub>-EGR): A benchmarking study for code comparison. *Environmental Earth Sciences*, 67(2):549–561, 2012.
- [23] Han, W. S., Stillman, G. A., Lu, M., Lu, C., McPherson, B. J., and Park, E. Evaluation of potential non-isothermal processes and heat transport during CO<sub>2</sub> sequestration. *Journal of Geophysical Research*, 115, 2010.
- [24] Vilarrasa, V. and Rutqvist, J. Thermal effects on geologic carbon storage. *Earth-Science Reviews*, 165: 245–256, 2017.
- [25] ZiabakhshGanji, Z. *Physical and Geochemical Impacts of Impure CO<sub>2</sub> on Storage in Depleted Hydrocarbon Reservoirs and Saline Aquifers*. PhD thesis, VU University Amsterdam, 2015.
- [26] Singh, A. K., Goerke, U. J., and Kolditz, O. Numerical simulation of non-isothermal compositional gas flow: Application to carbon dioxide injection into gas reservoirs. *Energy*, 36(5):3446–3458, 2011.
- [27] CMG. CMG GEM User Guide - Version 2017, 2017.
- [28] Pruess, K. *ECO2M: A TOUGH2 Fluid Property Module for Mixtures of Water, NaCl, and CO<sub>2</sub>, Including Super- and Sub-Critical Conditions, and Phase Change Between Liquid and Gaseous CO<sub>2</sub>*. LBNL-4590E, Berkeley, California, Lawrence Berkely National Laboratory, 2011.
- [29] Battistelli, A. and Marcolini, M. TMGAS: A new TOUGH2 EOS module for the numerical simulation of gas mixtures injection in geological structures. *International Journal of Greenhouse Gas Control*, 3(4): 481–493, 2009.
- [30] Oldenburg, C., Moridis, G., Spycher, N., and Pruess, K. *EOS7C: TOUGH2 Module for Carbon Dioxide or Nitrogen in Natural Gas (Methane) Reservoirs*. LBNL-56589, Berkeley, California, Lawrence Berkeley National Laboratory, 2004.
- [31] Loeve, D., Hofstee, C., and Maas, J. G. Thermal effects in a depleted gas field by cold CO<sub>2</sub> injection in the presence of methane. *Energy Procedia*, 63:5378–5393, 2014.
- [32] Loeve, D., Maas, J., and Obdam, A. A new TOUGH2-Module: ECO2MG. *TOUGH Symposium 2015*, 2015.
- [33] Maloney, D. R. and Briceno, M. Experimental Investigation of Cooling Effects Resulting from Injecting High Pressure Liquid or Supercritical CO<sub>2</sub> Into a Low Pressure Gas Reservoir. *Petrophysics*, 50(4):335–344, 2009.
- [34] Mathias, S. A., Gluyas, J. G., Oldenburg, C. M., and Tsang, C. F. Analytical solution for Joule-Thomson cooling during CO<sub>2</sub> geo-sequestration in depleted oil and gas reservoirs. *International Journal of Greenhouse Gas Control*, 4(5):806–810, 2010.
- [35] Lemmon, E., McLinden, M., and Friend, D. Thermophysical Properties of Fluid Systems. In *NIST Chemistry WebBook, NIST Standard Reference Database Number 69*. 2017.
- [36] Batzle, M. and Wang, Z. Seismic properties of pore fluids. *Geophysics*, 57(11):1396–1408, 1992.
- [37] Michaelides, E. Thermodynamic Properties of Geothermal Fluids. *Geothermal Resources Council Transactions*, 5:361–364, 1981.

- [38] André, L., Peysson, Y., and Azaroual, M. Well injectivity during CO<sub>2</sub> storage operations in deep saline aquifers - Part 2: Numerical simulations of drying, salt deposit mechanisms and role of capillary forces. *International Journal of Greenhouse Gas Control*, 22:301–312, 2014.
- [39] Spycher, N. and Pruess, K. CO<sub>2</sub>-H<sub>2</sub>O Mixtures in the Geological Sequestration of CO<sub>2</sub>. II. Partitioning in Chloride Brines at 12-100 C and up to 600 bar. *Geochimica et Cosmochimica Acta*, 67(16):3015–3031, 2004.
- [40] Duan, Z. and Mao, S. A thermodynamic model for calculating methane solubility, density and gas phase composition of methane-bearing aqueous fluids from 273 to 523 K and from 1 to 2000 bar. *Geochimica et Cosmochimica Acta*, 70(13):3369–3386, 2006.
- [41] Qin, J., Rosenbauer, R., and Duan, Z. Experimental Measurements of Vapor–Liquid Equilibria of the H<sub>2</sub>O + CO<sub>2</sub> + CH<sub>4</sub> Ternary System. *Journal of Chemical Engineering Data*, 53:1246–1249, 2008.
- [42] Sinnott, R. and Towler, G. *Chemical Engineering Design*. Elsevier Ltd., 2nd edition, 2013.
- [43] Jambhekar, V. A., Mejri, E., Schroder, N., Helmig, R., and Shokri, N. Kinetic Approach to Model Reactive Transport and Mixed Salt Precipitation in a Coupled Free-Flow–Porous-Media System. *Transport in Porous Media*, 114(2):341–369, 2016.
- [44] Chen, Z., Huan, G., and Ma, Y. *Computational Methods for Multiphase Flows in Porous Media*. Philadelphia, 2006.
- [45] Tang, Y., Yang, R., and Kang, X. Modeling the effect of water vaporization and salt precipitation on reservoir properties due to carbon dioxide sequestration in a depleted gas reservoir. *Petroleum*, 2017.
- [46] Guyant, E., Han, W. S., Kim, K.-Y., Park, M.-H., and Kim, B.-Y. Salt precipitation and CO<sub>2</sub>/brine flow distribution under different injection well completions. *International Journal of Greenhouse Gas Control*, 37:299–310, 2015.
- [47] Suárez-arriaga, M. C. Local Thermal Non-Equilibrium Interfacial Interactions in Heterogeneous Reservoirs -Divergence of Numerical Methods to Simulate the Fluid and Heat flow. In *40th Workshop on Geothermal Reservoir Engineering*, pages 1–15, 2016.
- [48] Vinsome, P. and Westerveld, J. A Simple Method for Predicting Cap and Base Rock Heat Losses in Thermal Reservoir Simulators. *Journal of Canadian Petroleum Technology*, 19(3):87–90, 1980.
- [49] Qiao, C., Li, L., Johns, R. T., and Xu, J. Compositional Modeling of Dissolution-Induced Injectivity Alteration During CO<sub>2</sub> Flooding in Carbonate Reservoirs. *SPE Journal*, (June):809–826, 2016.
- [50] Wolfsteiner, C., Durlofsky, L. J., and Aziz, K. Calculation of well index for nonconventional wells on arbitrary grids. *Computational Geosciences*, 7(1):61–82, 2003.
- [51] Szymkiewicz. *Modelling Water Flow in Unsaturated Porous Media*. Springer-Verlag Berlin Heidelberg, 1st edition, 2013.
- [52] Hangx, S. *Geological storage of CO<sub>2</sub>: Mechanical and chemical effects on host and seal formations*. PhD thesis, Utrecht University, 2009.
- [53] Roels, S. *Formation dry-out and injectivity impairment during CO<sub>2</sub> storage in saline aquifers*. PhD thesis, Delft University of Technology, 2015.
- [54] Misyura, S. Y. The influence of porosity and structural parameters on different kinds of gas hydrate dissociation. *Scientific Reports*, 6(July):1–10, 2016.
- [55] Golfier, F., Bazin, B., Lenormand, R., and Quintard, M. Core-scale description of porous media dissolution during acid injection - Part I: theoretical development. *Computational & Applied Mathematics*, 23(2-3):173–194, 2004.
- [56] Taylor, J. and Bryant, S. Quantifying thermally driven fracture geometry during CO<sub>2</sub> storage. *Energy Procedia*, 63:3390–3404, 2014.

- [57] Tambach, T., Bergen, F. V., Hofstee, C., Obdam, A., and Maas, J. Physical chemistry of CO<sub>2</sub> sequestration on macroscale and nanoscale. *CATO-2*, 2008.
- [58] Luo, Z. and Bryant, S. Impacts of injection induced fractures propagation in CO<sub>2</sub> geological sequestration - is fracturing good or bad for CO<sub>2</sub> sequestration. *Energy Procedia*, 63:5394–5407, 2014.
- [59] Dortmund Data Bank. Joule-Thomson Coefficient of Carbon dioxide, 2018. URL [www.ddbst.com](http://www.ddbst.com).
- [60] Jamaloei, B. Y. and Asghari, K. The joule-thomson effect in petroleum fields: II. CO<sub>2</sub> Sequestration, wellbore temperature profiles, and thermal stresses and wellbore stability. *Energy Sources, Part A: Recovery, Utilization and Environmental Effects*, 37(3):236–244, 2015.
- [61] Uddin, M., Coombe, D., and Wright, F. Modeling of CO<sub>2</sub>-Hydrate Formation in Geological Reservoirs by Injection of CO<sub>2</sub> Gas. *Journal of Energy Resources Technology*, 130(3):032502, 2008.
- [62] Shell. Peterhead CCS Project - Storage Development Plan. Technical report, 2015.
- [63] Egermann, P., Bazin, B., and Vizika, O. An Experimental Investigation of Reaction-Transport Phenomena During CO<sub>2</sub> Injection. *SPE Middle East Oil and Gas Show and Conference*, March, 2005.
- [64] Vandeweyer, V., Groenenberg, R., Donselaar, R., Pluymaekers, M., Loeve, D., Hofstee, C., Nepveu, M., Orlic, B., Akemu, O., Miersemann, U., Benedictus, T., Arts, R., Neele, F., Meindersma, W., and Dillen, M. CATO-2 Feasibility study P18 (final report). Technical report, 2011.
- [65] Ott, H., Roels, S. M., and de Kloe, K. Salt precipitation due to supercritical gas injection: I. Capillary-driven flow in unimodal sandstone. *International Journal of Greenhouse Gas Control*, 43:247–255, 2015.
- [66] Ott, H., Kloe, K. D., Marcelis, F., and Makurat, A. Injection of Supercritical CO<sub>2</sub> in Brine Saturated Sandstone : Pattern Formation during Salt Precipitation. *Energy Procedia*, 4:4425–4432, 2011.
- [67] Shojai Kaveh, N., Rudolph, E., Rossen, W., Van Hemert, P., and Wolf, K. Interfacial tension and contact angle determination in water-sandstone systems with injection of flue gas and CO<sub>2</sub>. *Saint Petersburg Russia - From Fundamental Science to Deployment: 17th European Symposium on Improved Oil Recovery, IOR*, (April):16–18, 2013.
- [68] Giorgis, T., Carpita, M., and Battistelli, A. 2D modeling of salt precipitation during the injection of dry CO<sub>2</sub> in a depleted gas reservoir. *Energy Conversion and Management*, 48:1816–1826, 2007.
- [69] Orlic, B., Heege, J. T., and Wassing, B. Assessing the integrity of fault- and top seals at CO<sub>2</sub> storage sites. *Energy Procedia*, 4:4798–4805, 2011.
- [70] Luo, Z. and Bryant, S. L. Influence of thermo-elastic stress on CO<sub>2</sub> injection induced fractures during storage. *SPE International Conference on CO<sub>2</sub> Capture, Storage, and Utilization, 10-12 November, New Orleans, Louisiana, USA*, 2010.
- [71] Pruess, K., Oldenburg, C., and Moridis, G. *TOUGH2 User's Guide, Version 2*. LBNL-43134, Berkeley, California, Lawrence Berkely National Laboratory, 2012.
- [72] Khan, C., Amin, R., and Madden, G. Carbon dioxide injection for enhanced gas recovery and storage (reservoir simulation). *Egyptian Journal of Petroleum*, 22(2):225–240, 2013.
- [73] Bacci, G., Korre, A., and Durucan, S. Experimental investigation into salt precipitation during CO<sub>2</sub> injection in saline aquifers. *Energy Procedia*, 4:4450–4456, 2011.
- [74] Tambach, T. J., Loeve, D., Hofstee, C., Plug, W. J., and Maas, J. G. Effect of CO<sub>2</sub> Injection on Brine Flow and Salt Precipitation After Gas Field Production. *Transport in Porous Media*, 108(1):171–183, 2015.
- [75] Vilarrasa, V., Bolster, D., Dentz, M., Olivella, S., and Carrera, J. Effects of CO<sub>2</sub> Compressibility on CO<sub>2</sub> Storage in Deep Saline Aquifers. *Transport in Porous Media*, 85(2):619–639, 2010.
- [76] Veltin, J. and Belfroid, S. CATO-2 Flow assurance studies for CO<sub>2</sub> transport. Technical report, 2013.

- [77] Jamaloei, B. Y. and Asghari, K. The Joule-Thomson effect in petroleum fields: I. Well testing, multilateral/slanted wells, hydrate formation, and drilling/completion/production operations. *Energy Sources, Part A: Recovery, Utilization and Environmental Effects*, 37(2):217–224, 2015.
- [78] Adewumi, M. Phase Relations in Reservoir Engineering - The Hydrate Problem, 2017. URL [https://www.e-education.psu.edu/png520/m21{}\\_p3.html](https://www.e-education.psu.edu/png520/m21{}_p3.html).
- [79] Li, H., Jakobsen, J. P., Wilhelmsen, Ø., and Yan, J. PVTxy properties of CO<sub>2</sub> mixtures relevant for CO<sub>2</sub> capture, transport and storage: Review of available experimental data and theoretical models. *Applied Energy*, 88(11):3567–3579, 2011.
- [80] Li, H. and Yan, J. Evaluating cubic equations of state for calculation of vapor-liquid equilibrium of CO<sub>2</sub> and CO<sub>2</sub>-mixtures for CO<sub>2</sub> capture and storage processes. *Applied Energy*, 86(6):826–836, 2009.
- [81] Porter, R. T., Fairweather, M., Pourkashanian, M., and Woolley, R. M. The range and level of impurities in CO<sub>2</sub> streams from different carbon capture sources. *International Journal of Greenhouse Gas Control*, 36:161–174, 2015.

# Nomenclature

## General symbols

### Symbol Description

$\alpha_T$	Thermo-elastic coefficient
$\beta$	Non-aqueous phase total mole fraction
$\Gamma$	Fractional length of pore bodies
$\lambda$	Thermal conductivity
$\mu$	Viscosity
$\mu_{i,\alpha}$	Chemical potential of component $i$ in phase $\alpha$
$\mu_{jt}$	Joule-Thomson coefficient
$\omega$	Accentric factor
$\phi$	Porosity
$\phi_i$	Fugacity coefficient of component $i$
$\phi_r$	Critical porosity
$\psi$	Permeability reduction factor
$\rho$	Density
$\sigma_t$	Thermo-elastic stress
$C$	Volumetric heat capacity
$C_p$	Specific heat capacity
$D_f$	Degrees of freedom
$E$	Young's modulus
$f_{i,\alpha}$	Fugacity of component $i$ in phase $\alpha$
$g$	Gravitational acceleration
$H$	Specific enthalpy
$h$	Height
$II$	Injectivity index
$K$	Rock permeability
$K_i$	Equilibrium constant of component $i$
$k_{H,i}$	Henry coefficient of component $i$
$k_{i,j}$	Binary interaction coefficient between component $i$ and $j$
$k_r$	Relative permeability
$n$	Corey exponent
$N_c$	Number of components
$N_p$	Number of phases
$p$	Pressure
$p_b$	Critical pore fluid pressure for fracture initiation
$p_c$	Capillary pressure
$q$	Source term
$Q_{inj}$	Injection mass rate
$R$	Gas constant
$r$	Radius
$S$	Saturation
$s$	Skin factor
$S_{\alpha,r}$	Residual saturation of phase $\alpha$
$S_{H,max}$	Maximum horizontal stress
$S_{h,min}$	Minimum horizontal stress
$T$	Temperature
$t$	Time
$U$	Internal energy

$u$	Darcy velocity
$\nu$	Poisson's ratio
$V_i$	Partial molar volume of component $i$
$WI$	Well index
$x_{i,\alpha}$	Composition of component $i$ in phase $\alpha$
$Z$	Compressibility factor
$z_i$	Overall composition of component $i$

### Subscripts and superscripts

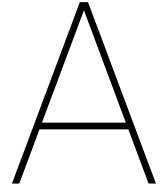
#### Symbol Description

0	Reference condition
$avg$	Average
$bhp$	Bottom hole pressure
$crit$	Critical
$eff$	Effective
$i$	Component $i$
$j$	Component $j$
$ini$	Initial
$max$	Maximum
$min$	Minimum
$r$	Rock
$res$	Reservoir
$sol$	Dissolution
$vap$	Vaporization
$w$	Well

### Phases and components

#### Symbol Description

$Aq$	Aqueous phase
$NA_L$	Non-aqueous liquid phase
$NA_V$	Non-aqueous vapor phase
$s$	Solid salt phase
$nw$	Non-wetting phase
$w$	Wetting phase
Ar	Argon
$CH_4$	Methane
$CO_2$	Carbon dioxide
$H_2$	Hydrogen
$H_2O$	Water
$H_2S$	Hydrogen sulfide
$N_2$	Nitrogen
$N_2$	Nitrogen
NaCl	Sodium chloride
$O_2$	Oxygen
$SO_2$	Sulfur dioxide



# Appendix

## A.1. Mutual solubility CO<sub>2</sub>-brine

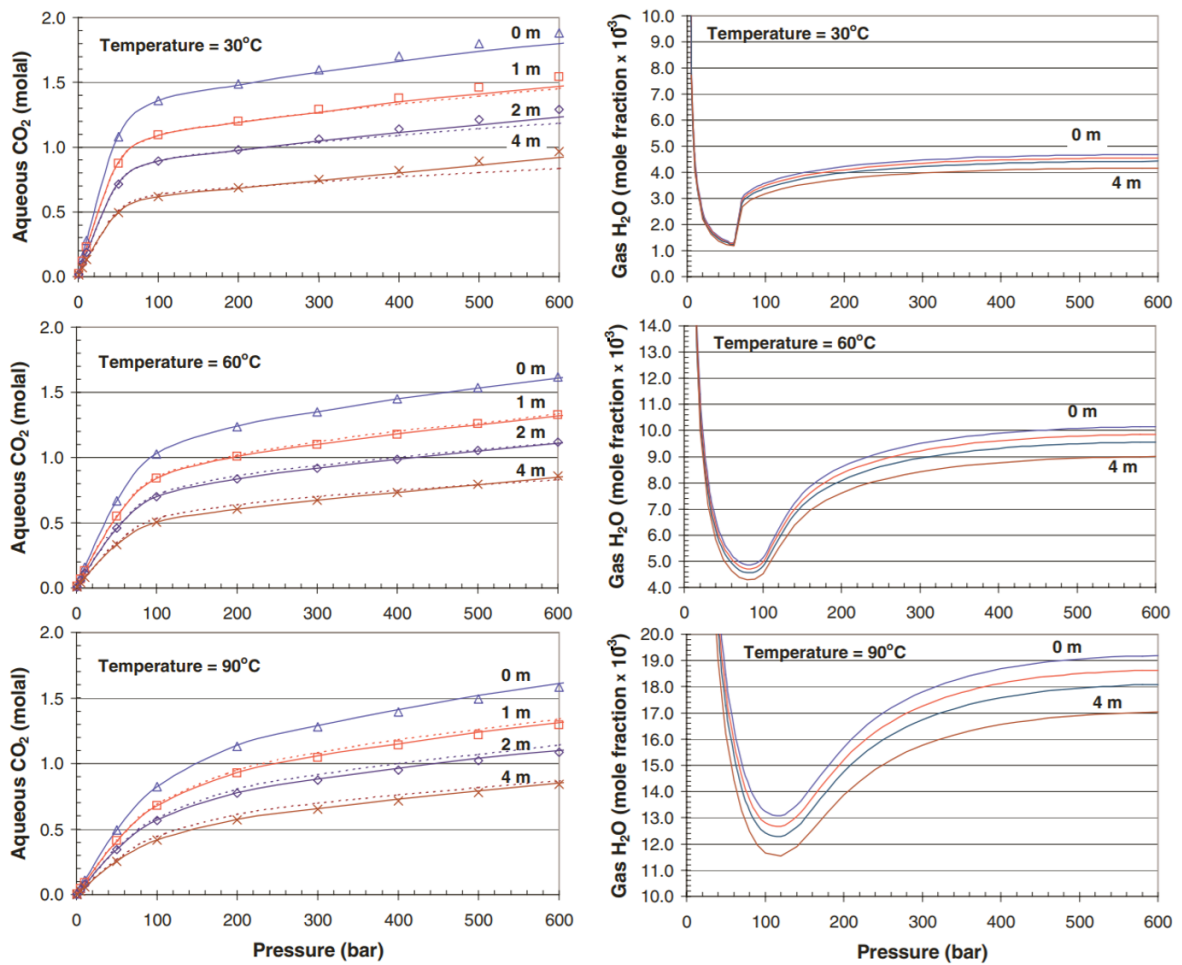


Figure A.1: Mutual solubility of CO<sub>2</sub> in the aqueous brine phase in molal (left) and H<sub>2</sub>O in the non-aqueous CO<sub>2</sub>-rich phase (right) for various pressures, temperatures and brine salinities, adopted from Spycher and Pruess [39].

## A.2. Mutual solubility CH<sub>4</sub>-brine

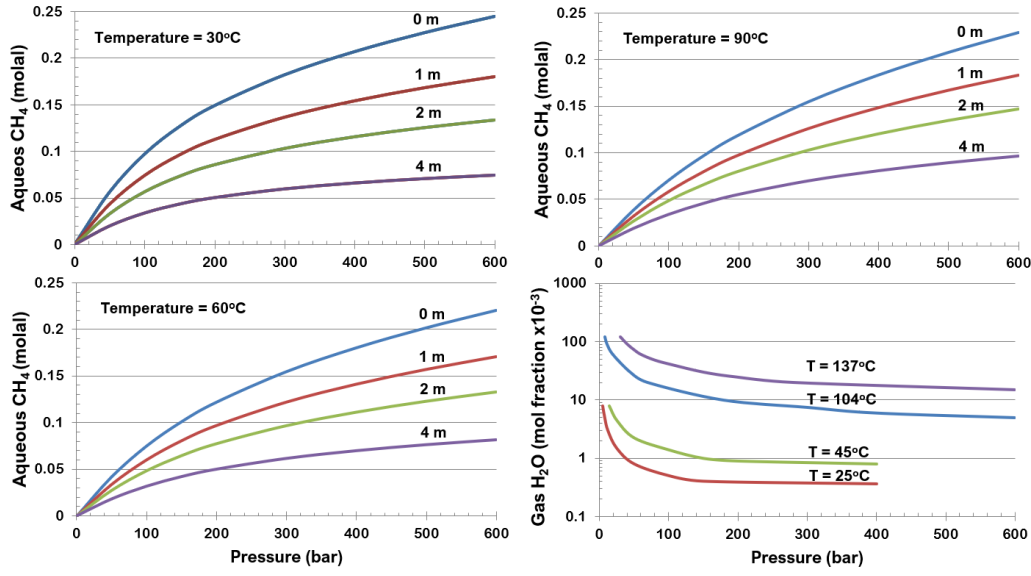


Figure A.2: Mutual solubility of CH<sub>4</sub> in the aqueous brine phase in molal and H<sub>2</sub>O in the CH<sub>4</sub>-rich phase (bottom-right) for various pressures, temperatures and brine salinities, adopted from Duan and Mao [40].

## A.3. Peng-Robinson EOS for non-aqueous phase fugacity coefficient determination

The PR EOS is applied to calculate the fugacity coefficient of the components in the non-aqueous phase. PR EOS in cubic polynomial form is defined as

$$Z^3 - (1 - B)Z^2 + (A - 2B - 3B^2)Z - (AB - B^2 - B^3) = 0. \quad (\text{A.1})$$

The parameters  $A$  and  $B$ , which are a function of temperature and pressure, are calculated by

$$A = \frac{\alpha(T)p}{(RT)^2}, \quad (\text{A.2})$$

and

$$B = \frac{bp}{RT}. \quad (\text{A.3})$$

The parameters  $a$  and  $b$  are given by

$$a(T) = 0.45724 \frac{R^2 T_{crit}^2}{p_{crit}} \alpha(T), \quad (\text{A.4})$$

and

$$b = 0.07780 \frac{RT_{crit}}{p_{crit}}, \quad (\text{A.5})$$

with

$$\alpha(T) = \left[ 1 + (0.37464 + 1.54226\omega - 0.26992\omega^2) \left( 1 - \sqrt{\frac{T}{T_{crit}}} \right) \right]^2. \quad (\text{A.6})$$

Here, the  $T_{crit}$  and  $p_{crit}$  indicate the critical temperature and pressure respectively and  $\omega$  represent the acentric factor. For mixture systems, mixing rules are adopted to obtain the values for the  $a$  and  $b$  parameters. Following the simple mixing rule, these values can be obtained from

$$a = \sum_i \sum_j x_{i,NA} x_{j,NA} a_{ij}, \quad a_{ij} = \sqrt{a_i a_j} (1 - k_{ij}), \quad b = \sum_i b_i x_{i,NA}, \quad (\text{A.7})$$

where  $k_{ij}$  denotes the binary interaction coefficients between the component  $i$  and  $j$  in the non-aqueous phase.

Before the fugacity can be derived, the compressibility factor in equation A.1 must be determined. Solving equation A.1 can provide three roots of which the root providing the lowest Gibbs free energy should be chosen, according to Battistelli and Marcolini [29]. Hereby, the intermediate root is neglected and two real values for the compressibility  $Z_a$  and  $Z_b$  remain. The final value for the compressibility factor is selected based on the outcome of the following equation, i.e.,

$$\frac{G_a}{RT} - \frac{G_b}{RT} = (Z_a - Z_b) + \ln \left( \frac{Z_b - B}{Z_a - B} \right) + \frac{1}{\delta_2 - \delta_1} \times \frac{A}{B} \ln \left[ \left( \frac{Z_b + \delta_2 B}{Z_a + \delta_2 B} \right) \left( \frac{Z_a + \delta_1 B}{Z_b + \delta_1 B} \right) \right], \quad (\text{A.8})$$

with  $\delta_1 = 1 + \sqrt{2}$  and  $\delta_2 = 1 - \sqrt{2}$ . If the term in the left hand side of A.8 is larger than zero, the final value for the compressibility is given by  $Z_b$  or else by  $Z_a$ .

After obtaining the compressibility factor, the fugacity coefficient can be determined using equation 2.35.

# B

## Appendix

### B.1. Derivation of analytical solution for Joule-Thomson cooling

The analytical solution of JTC for CO<sub>2</sub> in depleted gas reservoirs, developed and derived by Mathias et al. [34], is based on a simplified heat transport equation, i.e.,

$$\left[ \phi(1 - S_{H_2O,r})\rho_{CO_2}C_{p,CO_2} + \phi S_{H_2O,r}\rho_{H_2O}C_{p,H_2O} + (1 - \phi)\rho_r C_{p,r} \right] \frac{\partial T}{\partial t} = -q\rho_{CO_2}C_{p,CO_2} \left[ \frac{\partial T}{\partial r} - \mu_{jt} \frac{\partial p}{\partial r} \right]. \quad (B.1)$$

Including the following boundary conditions:

$$\begin{aligned} T &= T_0, & r &\geq r_w, & t &= 0 \\ T &= T_w, & r &= r_w, & t &> 0 \end{aligned}$$

Here, the CO<sub>2</sub> source term is written as

$$q = \frac{Q_{inj}}{2\pi r h \rho_{CO_2}}. \quad (B.2)$$

In equation B.1, Darcy's law for incompressible single phase flow is implemented to define the pressure gradient, given by

$$\frac{\partial p}{\partial r} = \frac{Q_{inj}\mu_{CO_2}}{2\pi h \rho_{CO_2} k_{r,CO_2} K}. \quad (B.3)$$

The radial distance of the prolonged CO<sub>2</sub> front into the reservoir can be calculated using

$$r_F = \left[ \frac{Q_{inj} t}{\pi h \phi(1 - S_{H_2O,r})\rho_{CO_2}} \right]^{1/2}. \quad (B.4)$$

In order to define an equation for the temperature profile along the reservoir, the transient heat equation (equation B.1) is coupled with the steady state flow equation from Darcy's law (equation B.3). In non dimensionless form this equation reads as

$$\frac{\partial T_D}{\partial t_D} = -\frac{1}{r_D} \left[ \frac{\partial T_D}{\partial r_D} + \frac{1}{r_D} \right]. \quad (B.5)$$

Including the boundary conditions

$$\begin{aligned} T_D &= 0, & r_D &\geq 1, & t_D &= 0 \\ T_D &= T_{wD}, & r_D &= 1, & t_D &> 0 \end{aligned}$$

The dimensionless variables are defined as

$$r_D = \frac{r}{r_w}, \quad (B.6)$$

$$t_D = \left[ \frac{C_{p,CO_2}}{\phi(1 - S_{H_2O,r})\rho_{CO_2}C_{p,CO_2} + \phi S_{H_2O,r}\rho_{H_2O}C_{p,H_2O} + (1 - \phi)\rho_r C_{p,r}} \right] \frac{Q_{inj} t}{2\pi h r_w^2}, \quad (B.7)$$

$$T_D = \frac{2\pi h k_{r,CO_2} K (T - T_0) \rho_{CO_2}}{\mu_{jt} Q_{inj} \mu_{CO_2}}, \quad (B.8)$$

$$T_{wD} = \frac{2\pi h k_{r,CO_2} K (T_w - T_0) \rho_{CO_2}}{\mu_{jt} Q_{inj} \mu_{CO_2}}. \quad (B.9)$$

Applying Laplace transformations and further reduction of equation B.5 eventually leads to

$$T_D(r_D, t_D) = \begin{cases} \frac{1}{2} \ln(1 - \frac{2t_D}{r_D^2}), & t_D < \frac{r_D^2 - 1}{2} \\ \frac{1}{2} \ln(\frac{1}{r_D^2} + T_{wD}), & t_D \geq \frac{r_D^2 - 1}{2} \end{cases}, \quad (B.10)$$

Rewriting equation B.10, conversion into general dimensions and implementing  $t_D = (r_D^2 - 1)/2$  provides an explicit expression for the minimum temperature reached in the reservoir, which is located at the discontinuity and given by

$$T_{min} = \frac{\mu_{jt} Q_{inj} \mu_{CO_2}}{4\pi h k_{r,CO_2} K \rho_{CO_2}} \times \ln \left\{ \left[ \frac{C_{p,CO_2}}{\phi(1 - S_{H_2O,r}) \rho_{CO_2} C_{p,CO_2} + \phi S_{H_2O,r} \rho_{H_2O} C_{p,H_2O} + (1 - \phi) \rho_r C_{p,r}} \right] \frac{Q_{inj} t}{\pi h r_w^2} + 1 \right\} \\ + \begin{cases} T_0, & T_0 \leq T_w \\ T_w, & T_0 > T_w \end{cases}. \quad (B.11)$$

# C

## Appendix

### C.1. Modified phase envelopes in ECO2MG

The phase envelopes in ECO2MG, modified to ensure monotonically increasing dew point lines, are depicted below.

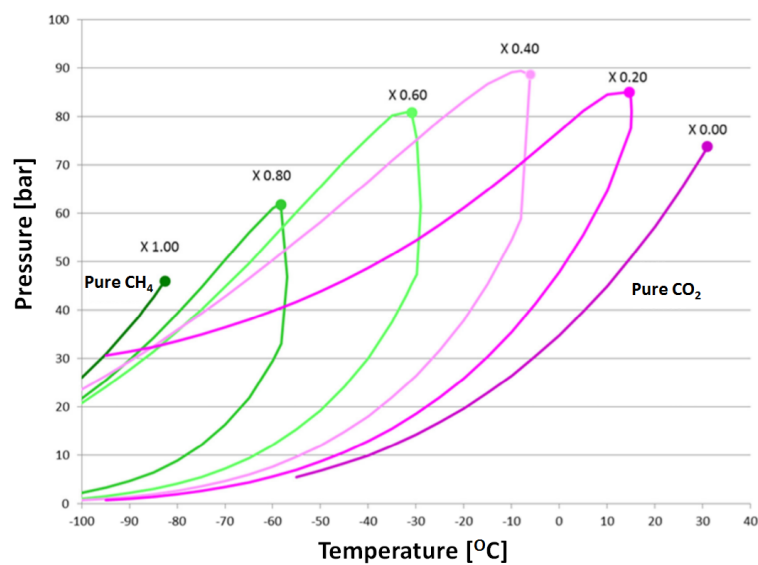


Figure C.1: Modified CO<sub>2</sub>-CH<sub>4</sub> phase envelopes in ECO2MG [32].

# D

## Appendix

### D.1. Comparison between CO<sub>2</sub>-brine and CO<sub>2</sub>-CH<sub>4</sub>-brine systems

Modeling of an additional CH<sub>4</sub> component in a CO<sub>2</sub>-brine system requires a more complex phase partitioning model. To examine the modeling accuracy of only a CO<sub>2</sub>-brine system with respect to a CO<sub>2</sub>-CH<sub>4</sub>-brine system, two simulations have been conducted with different initial reservoir pressures, i.e. 40 and 100 bar. In the simulation where only CO<sub>2</sub>-brine was considered, the initially present CH<sub>4</sub> was substituted for CO<sub>2</sub>. At an injection temperature of 45°C and 40 bar, the CO<sub>2</sub> is in gaseous condition while at 100 bar the CO<sub>2</sub> is supercritical condition.

Important flow properties as viscosity and compressibility of CH<sub>4</sub> differ from CO<sub>2</sub>. Hence, substitution of CH<sub>4</sub> by CO<sub>2</sub> would affect the behavior of the system, due to differences in flow properties, altering the pressure gradient in the near wellbore region and the JTC. The obtained temperature and pressure profiles are shown in figure D.1.

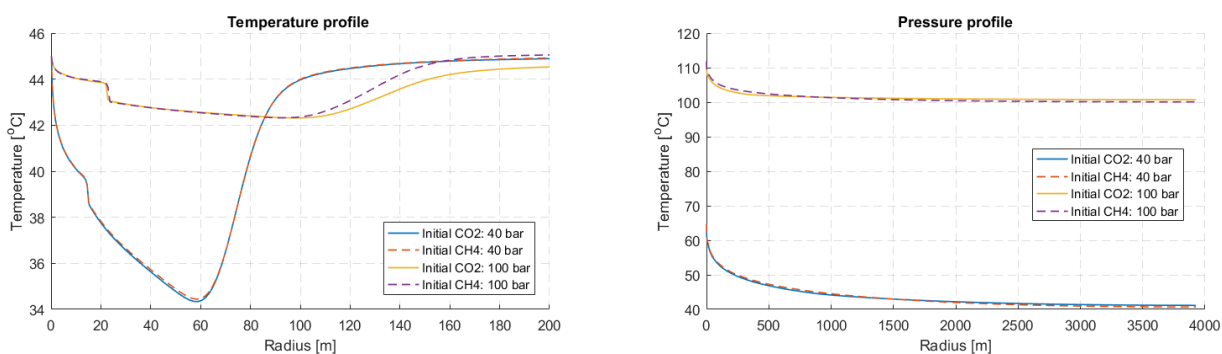


Figure D.1: Temperature and pressure profiles for a CO<sub>2</sub>-brine system (dashed lines) and original CO<sub>2</sub>-CH<sub>4</sub>-brine (solid lines) for an initial pressure of 40 bar (i.e. subcritical conditions) and 100 bar (i.e. supercritical conditions).

The simulation results indicate that, in particular at subcritical conditions of CO<sub>2</sub>, the magnitudes of the thermal effects and extent of the dry-out are highly similar. The pressure gradient in the simulation with initial CO<sub>2</sub> is higher over the near wellbore region compared to initial CH<sub>4</sub>, causing slightly more cooling. However, a reasonable estimation can be made of the thermal near wellbore effects in a depleted gas system with initial methane by modeling a more simplistic CO<sub>2</sub>-brine system, where the reservoir is initially filled with CO<sub>2</sub> instead of CH<sub>4</sub>. In addition, for a realistic reservoir temperature of 90°C instead of 45°C, the differences between temperature profiles of a CO<sub>2</sub>-brine and a CO<sub>2</sub>-CH<sub>4</sub>-brine system were found to be even smaller.



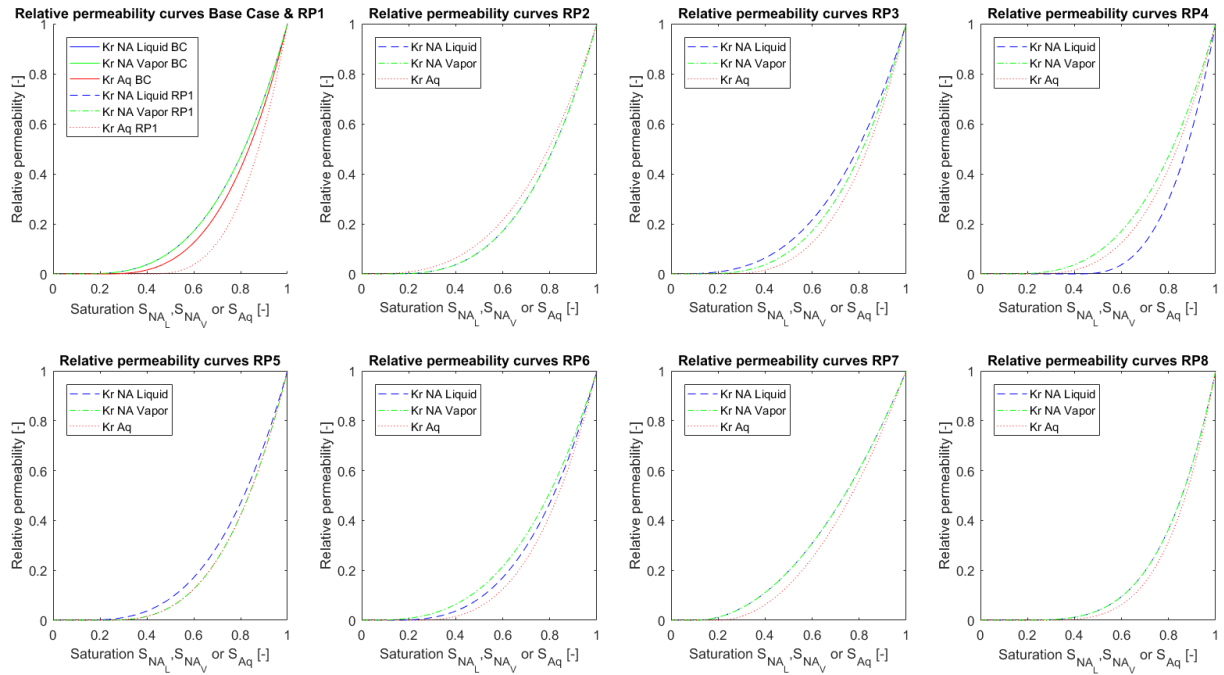


Figure D.3: Relative permeability curves based on the values given in table D.1, utilized to study the sensitivity with respect to the relative permeability

The results of the simulation conducted with the various permeability curves are shown in figure D.4. Capillary pressure are neglected in the simulations.

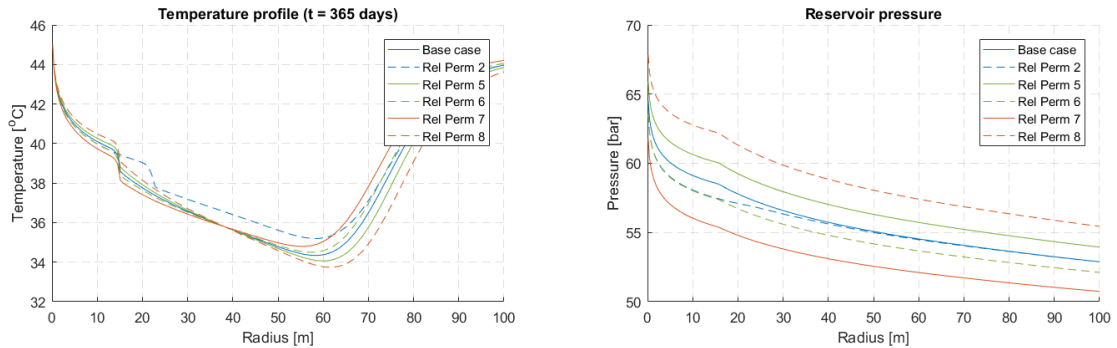


Figure D.4: (Case 13) Temperature and pressure profile for different relative permeability curves.

The temperature profiles for the cases with relative permeability curves RP3 and RP4 exactly overlap the base case scenario, since  $\text{CO}_2$  in liquid phase is not encountered. Likewise, the change in aqueous phase relative permeability in RP1 does not affect the system since aqueous phase is already immobile in the base case.

### D.4. Rock thermal parameters and temperature profiles

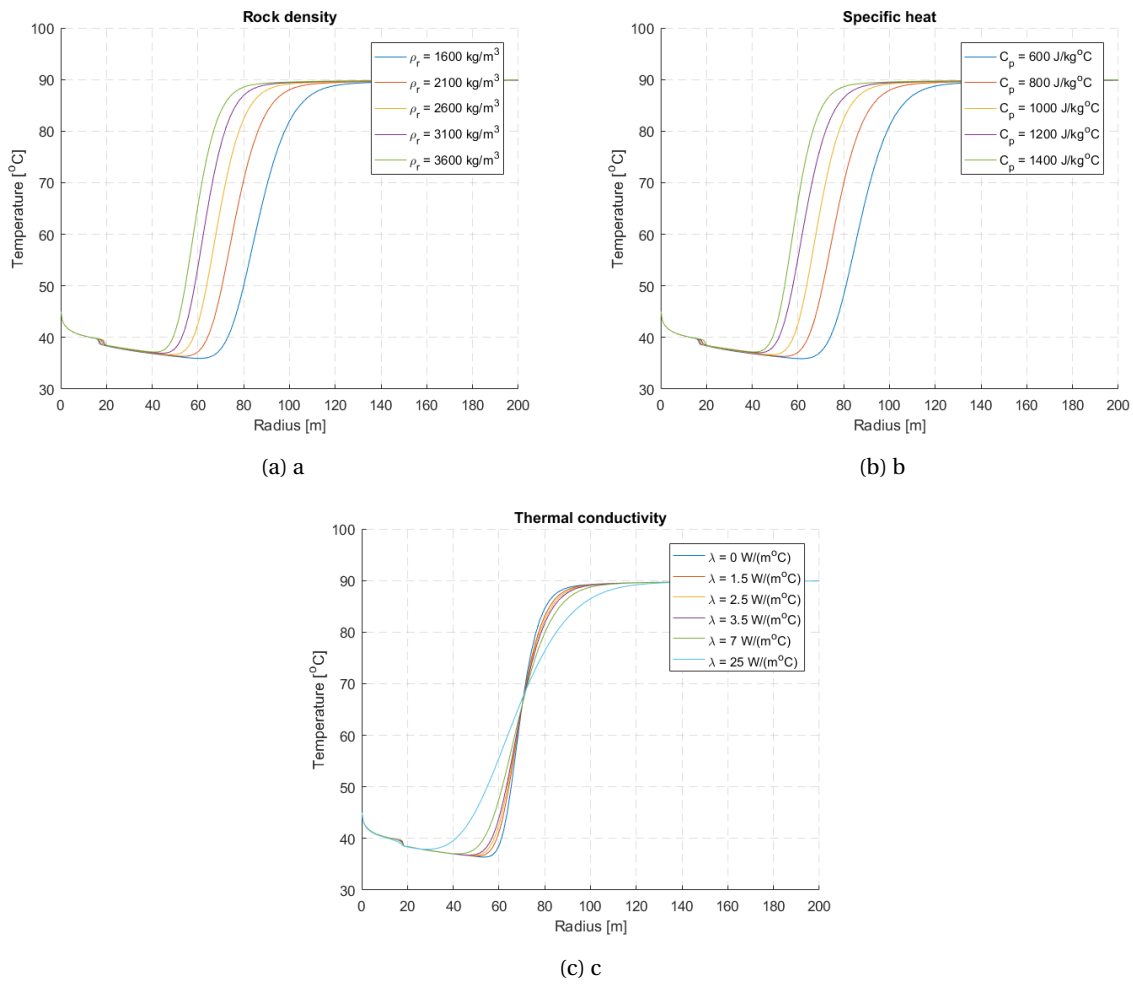


Figure D.5: (Case 14) Temperature profiles for (a) different densities, (b) specific heat capacities and (c) thermal conductivities of the formation after 1 year of injection.

# E

## Appendix

### E.1. Realistic CO<sub>2</sub> bottom hole injection temperature

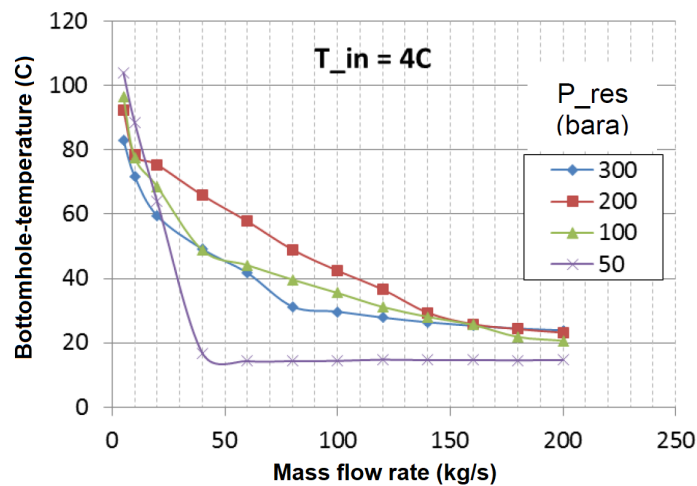


Figure E.1: Bottom hole temperature for a CO<sub>2</sub> injection well of approximately 3200 m depth versus flow rate at different initial reservoir temperatures with an initial surface CO<sub>2</sub> injection temperature of 4°C [76].

### E.2. Impure CO<sub>2</sub> injection temperature profiles

#### E.2.1. 90 mole% CO<sub>2</sub> and 10 mole% impurity at 35 kg/s

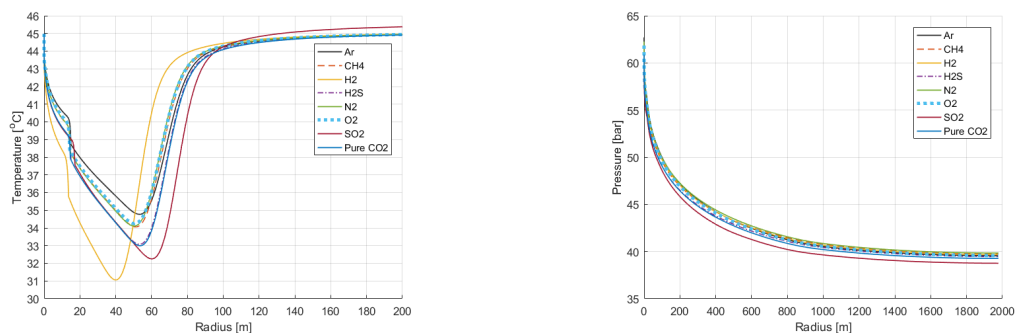
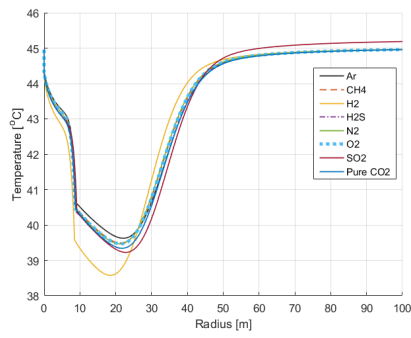
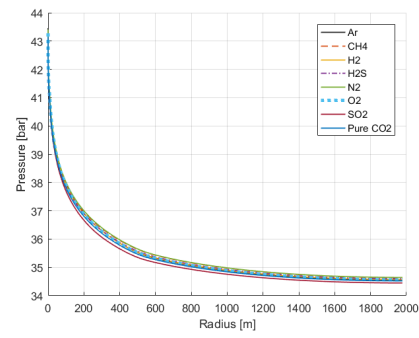


Figure E.2: Temperature and pressure profile for an injected CO<sub>2</sub> stream with a composition of 90 mole% CO<sub>2</sub> and 10 mole% impurity after 1 year of injection at 35 kg/s.

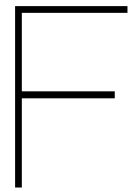
**E.2.2. 95 mole% CO<sub>2</sub> and 5 mole% impurity at 10 kg/s**

(a) Density



(b) Viscosity

Figure E.3: Temperature and pressure profile for an injected CO<sub>2</sub> stream with a composition of 95 mole% CO<sub>2</sub> and 5 mole% impurity after 1 year of injection at 10 kg/s.



# Appendix

## F.1. Effect of grid refinement

Grid resolution in the vicinity of the well impacts the near wellbore pressure and temperature distribution. To illustrate the importance of grid refinement, several simulations are performed on an identical Cartesian coarse grid but with different grid resolutions of the cell perforated by well. The original cells size of the model generated for this refinement study is approximately 50 m and thus equivalent to the P18-4 model. In figure F.1, the effect of grid refinement in the near wellbore region is shown.

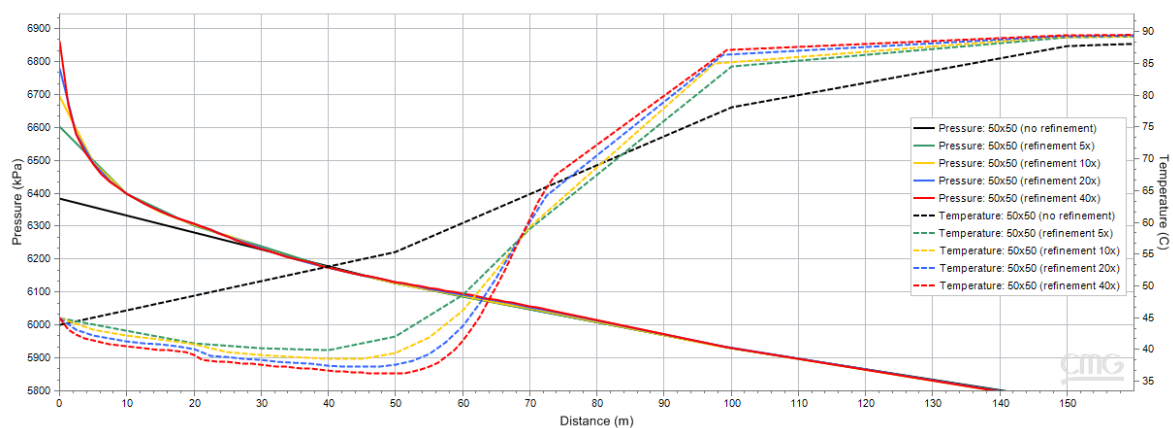


Figure F.1: Pressure and temperature profiles for a grid with different refinement levels of the cell perforated by the well.

It is clearly obvious that grid refinement is necessary on large coarse grids to accurately capture the near wellbore physical effects. The highest refinement provides the most accurate result. However, it should be taken into account that grid refinement negatively affects simulation time, especially for high refinement ratios.

## F.2. Effect of well location and reservoir geometry

The well location with respect to the no-flow boundaries of the grid and grid geometry play an important role in the pressure distribution around the well. As extensively discussed previously, two characteristic features strongly influence the JTC, i.e. the gradient of the pressure curve and the absolute pressure value. The influence of the geometry on the pressure behavior of the reservoir is tested for reservoir with different length to width ratios, but with approximately equivalent volumes (see figure F.2).

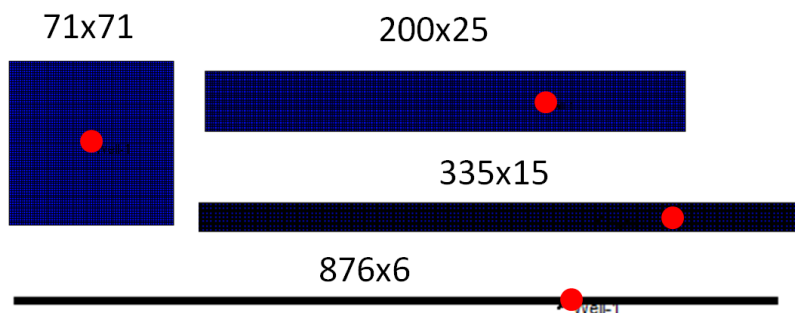


Figure F2: Geometries of the different reservoirs tested ranging from a symmetric to an highly elongated reservoir with approximately the same volumes.

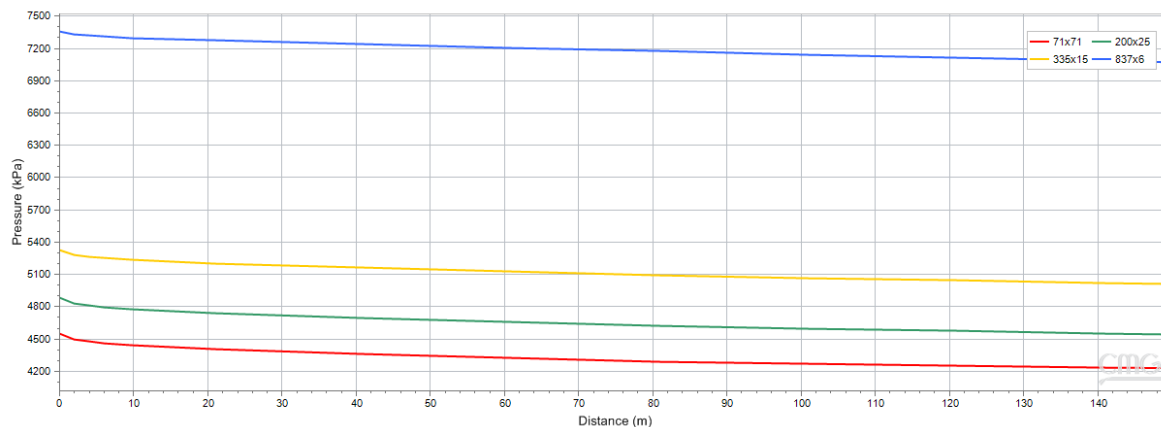


Figure F3: Pressure profiles for the various reservoir geometries illustrated in figure F2 after 1 year of injection.

Figure F3 indicates that the pressure response is highly sensitive to the reservoir geometry and well location. Absolute pressure increases and pressure gradient close to the well decreases, as the length to width ratio becomes larger. The boundary effects become more significant for smaller distances between the boundaries of the reservoir domain and the well. These boundary affects are clearly visible in the absolute value of the pressure. Most favorable for the Joule-Thomson cooling effect is the symmetric geometry (i.e. 71x71). In this case the effect of the boundary is small and the buildup in pressure is slow. Hence, an abundant amount of CO<sub>2</sub> is injected in gaseous phase with a high JT coefficient. The JTC cooling will therefore be significant. This in contrast to the highly elongated reservoir (e.g. 876x6), where the boundary effect causes the pressure to rise rapidly and the JTC is only minor.